SPATIALLY-DENSE, MULTI-SPECTRAL, FREQUENCY-DOMAIN DIFFUSE OPTICAL TOMOGRAPHY OF BREAST CANCER

Han Yong Ban

A DISSERTATION

in

Physics and Astronomy

Presented to the Faculties of the University of Pennsylvania in Partial

Fulfillment of the Requirements for the Degree of Doctor of Philosophy

2015

____

Arjun G. Yodh, Professor of Physics and Astronomy

Supervisor of Dissertation

____

Marija Drndic, Professor of Physics and Astronomy

Graduate Group Chairperson

Dissertation Committee

Masao Sato, Professor of Physics and Astronomy

Timothy Zhu, Professor of Radiation Oncology

Ravinder Reddy, Professor of Radiology

Frank Moscatelli, Professor of Physics and Astronomy

Dedication

I dedicate this work to:

the cancer patients who volunteered for our research,

friends who supported me through my failures and celebrated my successes,

mom and dad, who love me unconditionally, and my brother whom I love,

and God, without whom I would be nothing.

Acknowledgements

My graduate work would not have been possible without the help and support of many people. First and foremost I want to acknowledge my advisor, Arjun Yodh. I have learned a lot from Arjun over the years and I still strive to emulate his ability to think outside the box when problem solving. His deep knowledge of not just the biomedical optics field but nonlinear optics and soft condense matter physics is very apparent when discussing how to approach various problems. Arjun has always been generous with his time and advice and I will always be thankful for that.

I want to thank my collaborators as well. I've had the honor of being able to work with world class researchers like John Schotland, Manabu Machida, and Vadim Markel. Vadim was always patient in teach me about image reconstructions and it has been a pleasure to work closely with him. I also want to thank Simon Arridge and Martin Schweiger for their work on the Gen3 imager project. I am especially thankful to Martin for enduring hot summers in Philadelphia to work to produce our images and for spending time teaching me about nonlinear reconstruction methods. I also want to thank Mitchell Schnall, Brian Czerniecki, and Emily Conant without whom our clinical work would not be possible.

When I first joined Arjun's lab I worked with Kijoon Lee. Kijoon got me started at the lab and really went out of his way to help me learn about diffuse optics and instrumentation. I could tell that he really loved to teach. Kijoon soon left for Singapore and I was certainly poorer for not being able to learn more from him before he left. It was only a few months but I also got to meet with Alper Corlu, Chao Zhou, Jonathan Fisher, and Guoqiang Yu all who warmly welcomed me into the lab.

In my earlier years Dr. Regine Choe and Turgut Durduran were truly Arjun's lieutenants and advised all of the graduate students. They really shaped my early graduate experience and I learned a great deal from them. In particular Regine got me started in learning about breast imaging.

There were many people who worked with me on breast imaging over the years and helped me get over a lot of hurdles. I want to thank the numerous clinical coordinators like Maddie Winters, Sarah Grundy, and Alex Vandergrift who recruited patients and made sure they were comfortable. I want to thank Darren for his enthusiasm, relentless energy, and drive without which I could not have finished the Gen3 project. I also remember interesting nights at Perelman with Bryan Chong and sharing stories in the dark while taking data. Jeff is also one of my peers who I've felt a kinship in instrumentation work. My only regret is that I did not work with him more over the years. Frank Moscatelli was one of the few people who called things as it is and I have him to thank for teaching me people skills. I cannot forget Jaka Katrasnik who was here for a short time but became one of my closest friends. I also want to thank Sophie Chung, Sarauv Pathak and Soren Konecky as well.

Then there are those who I consider good friends who made coming into the lab a lot of fun. Meeri Kim is (probably) up there in best friends of all time. Erin Buckley and I (along with Meeri) have shared a few pet rodents together and that is a strong bond that cannot be broken (R.I.P. hamster JD). Wes Baker has always been a good friend who always made me laugh every time he joked around and who always made it more fun to hang out if he was around. Jennifer Lynch was always a comrade in arms and the best fashion advisor and life cheerleader anyone could ask for. Steve (or Sam) Schenkel for the workout sessions and just being a great guy to hang out with. Tiffany Ko for living life in a way that I envied and being a generous friend. I want to thank Ken Abrahmson as well for great conversations and being our lab's Q.

I want to acknowledge David Busch who gave countless advice that was incredibly helpful academically and personally. I owe him more than I can repay and I really cherish his friendship. Ashwin Parthasarathy has been a friend from day one. I have him to thank for many great conversations, ideas, and really fun moments in the office. He talked me through some hard times and I really appreciated that. I want to also thank Venki Kauri because he saved my life. I've known him less than a year but Venki really brought a great surge of curiosity and love of diffuse optics that one can only describe as contagious. I want to thank other people who have really shaped my time here in the lab like Rickson Mesquita, ShihYu Tzeng, Zhe Li, Detian Wang, Alex Zhang, Julien Menko, Leonid Zubkov, and Michelle Wong.

Finally I want to thank my family for their support throughout these years. They've always encouraged me from when I tried to be a cellist to when I decided to become a physicist. Thank you mom and dad for your constant love and encouragement. Thank you all for making this work possible.

ABSTRACT

SPATIALLY-DENSE, MULTI-SPECTRAL, FREQUENCY-DOMAIN DIFFUSE OPTICAL TOMOGRAPHY OF BREAST CANCER

Han Y. Ban

Arjun G. Yodh

Diffuse optical tomography (DOT) employs near-infrared light to image the concentration of chromophores and cell organelles in tissue and thereby providing access to functional parameters that can differentiate cancerous from normal tissues. This thesis describes research at the bench and in the clinic that explores and identifies the potential of DOT breast cancer imaging. The bench and clinic instrumentation differ but share important features: they utilize a very large, spatially dense, set of source-detector pairs (10^7) for imaging in the parallel-plate geometry.

The bench experiments explored three-dimensional (3D) image resolution and fidelity as a function of numerous parameters and also ascertained the effects of a chest wall phantom. The chest wall is always present but is typically ignored in breast DOT. My experiments clarified chest wall influences and developed schemes to mitigate these effects. Mostly, these schemes involved selective data exclusion, but their efficacy also depended on reconstruction approach. Reconstruction algorithms based on analytic (fast) Fourier inversion and linear algebraic techniques were explored.

The clinical experiments centered around a DOT instrument that I designed, constructed, and have begun to test (in-vitro and in-vivo). This instrumentation offers many features new to the field. Specifically, the imager employs spatially-dense, multi-spectral, frequency-domain data; it possesses the world's largest optical source-detector density yet reported, facilitated by highly-parallel CCD-based frequency-domain imaging based on gain-modulation heterodyne detection. The instrument thus measures both phase and amplitude of the diffusive light waves. Other features include both frontal and sagittal breast imaging capabilities, ancillary cameras for measurement of breast boundary profiles, real-time data normalization, and mechanical improvements for patient comfort. The instrument design and construction is my most significant contribution, but first imaging experiments with tissue phantoms and of cancer bearing breasts were also carried out. A parallel effort with simulated data has yielded important information about new reconstruction regularization issues that arise when phase and amplitude are measured. With these gains in device implementation and DOT reconstruction, my research takes valuable steps towards bringing this novel imaging technique closer to clinical utilization.

Contents

List of Tables

List of Figures

Chapter 1

Introduction

1.1 Diffuse Optics

The desire to use light to characterize human tissues and carry out tissue biopsy is pervasive in science-fiction has begun to penetrate the more traditional scientific and medical communities. Early attempts to use light for tissue imaging, for example, date back to the 1930's when transillumination images of breast were used to detect the "shadows" of tumors [1]. Unfortunately, because tissue is both highly absorbing and highly scattering, such crude light projections were found to be too unreliable for medical use, especially when compared to standard techniques in the clinic such as x-ray imaging.

The potential for clinical imaging with light was revisited in the 1970's and 80's with the rediscovery of the so-called spectral "window" in tissue [2–4]. Indeed, light in the near-infrared (NIR) part of the spectrum ($600 - 1000$ nm) is minimally absorbed by tissue hemoglobin and water (Figure 1.1), though it is substantially scattered by tissue organelles. This realization eventually gave birth to the field of NIR spectroscopy. Minimal absorption in this spectral "window"

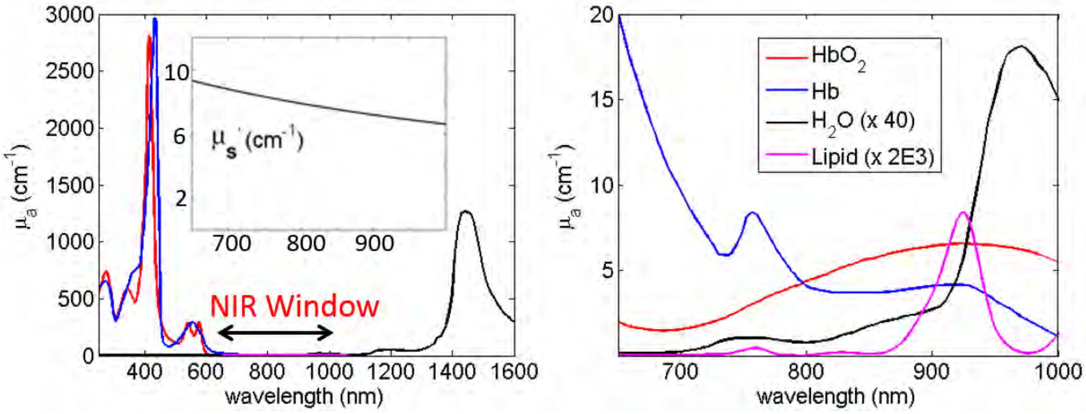

Figure 1.1: Spectra of the major chromophores in tissue showing the "Near-infrared window". H_2O ($\times 40$) and lipid ($\times 2000$) has been scaled up to be visible on the plots. Hemoglobin concentrations for 150g Hb/L (whole blood). a) Low absorption region that defines the NIR window; Inset: Estimated μ_s' for breast tissues from Mie scattering theory in the NIR window. b) Tissue absorption coefficients in the NIR window for common chromophores. *Spectral data compiled at http://omlc.org/spectra/index.html*

permitted light to penetrate deeply into tissue and thereby provided optical access to information about tissue chromophores such as oxy-hemoglobin (HbO_2), deoxy-hemoglobin (Hb), lipid, and water (H_2O). However, at the time, these methods were better characterized as qualitative rather than quantitative.

The situation changed in the late 1980's and early 1990's when the community recognized that near-infrared (NIR) light diffuses in tissues [5–7]. In the diffusion model, photons travel along random walk trajectories through tissue. These light trajectories are characterized by a wavelength-dependent reduced scattering coefficient ($\mu_s'(\lambda)$) (see Figure 1.1 and Figure 1.2), which is the reciprocal of the random walk step length, and a wavelength-dependent absorption coefficient ($\mu_a(\lambda)$), which depends on the concentrations of tissue chromophores such as oxy-hemoglobin (HbO_2), deoxy-hemoglobin (Hb), lipid, and water (H_2O). Adoption of the diffusion

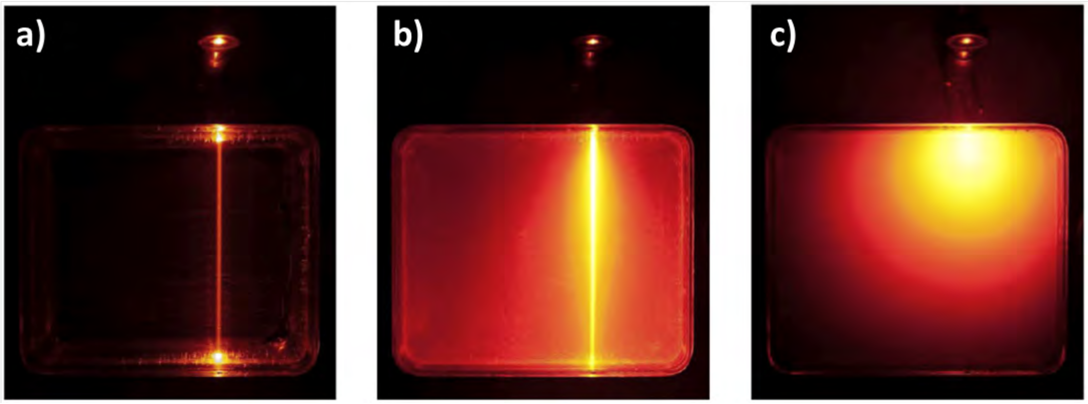

Figure 1.2: Photograph showing a top-view image of a collimated NIR light beam as it passes through solutions with variable scattering coefficient (μ_s'). a) Small scattering coefficient. b) Medium scattering coefficient. c) Large scattering coefficient.

model for light transport, in turn, opened up the possibility for quantitative diffuse optical spectroscopy (DOS) or near-infrared spectroscopy (NIRS). [8–32] and diffuse optical tomography (DOT) [12, 33–55].

Of course, the key attraction of diffuse optical techniques is that they are sensitive to functional information about tissue hemodynamics and oxygen metabolism, e.g., as reflected in the variation of total hemoglobin concentration (THC), blood oxygen saturation (StO_2), tissue scattering (μ_s'), and even tissue blood flow [15, 20, 46, 56–70]. Indeed, all of these physiological parameters are pathologically relevant biomarkers of cancer, stroke, and other tissue disease/injury. Further, the diffuse optical methods have other attractive features. They are generally non-invasive, use non-ionizing radiation, are relatively rapid and portable, and they offer high-throughput (e.g., repeated or continuous measurements at the bedside). Finally, optical methods hold potential for use in multi-modal settings with other medical diagnostics such as ultrasound, MRI, X-ray, and PET.

In this thesis, I employ diffuse optics for imaging oxy- and deoxy-hemoglobin and tissue scattering in the human breast. My long-range goal is to use the contrast offered by these physiological parameters to identify and characterize breast lesions and to monitor breast tumor progression. This work builds on previous research in diffuse optical tomography, but it pushes the current limits of breast DOT both instrumentally and algorithmically. It is my hope that this research takes useful steps for clinical translation of quantitative DOT for breast cancer imaging.

1.2 Spectroscopic monitoring and imaging of breast cancer

For women in the U.S., breast cancer is the second most commonly diagnosed cancer (after skin cancer) and the second leading cause of cancer death (after lung cancer) [71]. While the mortality rate of breast cancer has decreased significantly in recent years, the overall number of women affected remains large. In 2012, the American Cancer society estimated that $39,510$ of the $226,870$ new cases of breast cancer would lead to death in the U.S. [72]. In addition, the National Cancer Institute estimated the cost of breast cancer to the U.S. economy as greater than $\$8$ billion (2007) [73].

Currently, many imaging modalities are in use for the detection, diagnosis and management of breast cancer. X-ray mammography is the most prevalent and widely adopted breast cancer screening tool; it employs ionizing photons to create high resolution projection images (~ 0.1 mm/pixel). Ultrasound imaging is another useful method that probes the acoustic/mechanical properties of tissue with high-frequency sound waves; e.g., it uses acoustic wave reflection to locate a suspicious mass. Single Photon Emission Computed Tomography (SPECT) and Positron Emission Tomography (PET) represent still other useful imaging modalities based on the detection of gamma rays emitted from radioactive tagged proteins or sugars that are injected (or inhaled); tracking these macromolecules permits exploration of tissue metabolic pathways which can be different in tumors compared to normal tissues. Finally, Magnetic Resonance Imaging (MRI) employs radio waves and strong magnetic fields to probe tissue structure and function; these techniques rely on measurement of spin relaxation times to gain sensitivity to tissue micro-environment and to diagnose disease.

All of these techniques have advantages (e.g., x-ray: high resolution, ultrasound: low cost, PET: metabolism detection, MRI: function and structure) and disadvantages (e.g., x-ray: ionizing radiation, ultrasound: contrast and penetration, PET: ionizing radiation, MRI: throughput and cost) that lead to arguments about which modality should be standard in breast cancer screening and diagnosis. In reality, no technology is perfect for all scenarios, and most modern approaches to breast cancer treatment utilize a combination of imaging technologies in synchrony with an array of treatments tailored to the patient (e.g., neoadjuvant chemotherapy, lumpectomy, mastectomy). In this environment, there is a need for additional modalities to detect cancers earlier, to detect cancers in populations with low specificity (e.g., women with dense breasts), and to track functional information during treatment (such as neoadjuvant chemotherapy).

By comparison to the medical diagnostics described above, diffuse optics is new. It also has different contrast mechanisms and complementary strengths. For example, DOT's ability to measure endogenous tissue chromophores (Hb, HbO) and exogenous optical contrast agents (ICG) provides access to functional processes and to parameters which are useful for detection and characterization of breast tumors with high sensitivity and specificity [53, 74]. Cancer cells are accompanied by various growth factors that spur angiogenesis and can result in higher blood

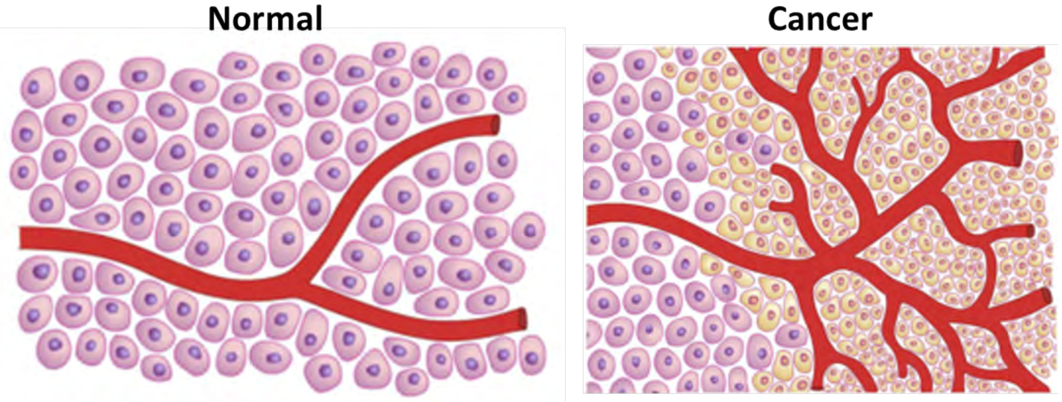

Figure 1.3: Illustration of normal and cancer tissue. Cancer tissue regions have greater blood vessel and cell/cell-organelle densities due to angiogenesis and cell growth which can be differentiated optically compared to surrounding health tissue region. *Figure courtesy of R. Choe.* [80]

concentration in the tumor region [75–77]; this variation in hemoglobin content can be detected as an absorption contrast optically. Further, cellular and extracelluar components, such as nuclei, mitochondia, and other organelles, are known to scatter light due to their refractive index differences and size, and their scattering can be modeled with Mie scattering theory [78, 79]. In tumors, these regions of enhanced cell growth and mitochondrial density can produce greater scattering compared to healthy tissue, and these scattering changes can be detected optically (see Figure 1.3).

Further, as noted above, DOT is non-invasive, uses non-ionizing radiation, and is relatively low in cost compared to most diagnostic modalities, though it suffers from issues of low spatial resolution. Despite this apparent disadvantage, several groups (including ours) have shown that changes in optics-based physiological contrast can be utilized to distinguish between healthy and diseased tissue; this general approach has by now found use in investigations of muscle [14, 59, 62, 81], brain [13, 15, 19, 20, 28, 56, 61, 65, 80, 82–89] and breast cancer. DOT, with its access to functional information, low cost, high throughput (of patients), and potentially high specificity and sensitivity is an attractive modality for development in the current roster of imaging technologies used in breast cancer diagnosis and treatment.

In the context of breast imaging, DOT utilizes light sources on the surface of tissues to illuminate the breast and employs detectors to access light that has been transmitted and scattered in tissue. With literally many thousands of source-detector pairs on the tissue boundaries, DOT readily employs these measured light fluence rate signals in order to computationally reconstruct the 3D distribution of μ_a and μ_s' within the sampled tissue. While large DOT datasets have been prohibitively data intensive in the past, decreasing computational costs and increasing computational processing power make DOT a more attractive modality for clinical development. To date, DOT has successfully imaged tumors in the breast in a variety of clinical situations. For example it has been shown that DOT can differentiate of malignant and benign tumors [10,12,41,53,90–92]. DOT and DOS have also been shown to have potential for statistical separation of responders from partial responders to inform chemotherapy treatments [32,93–98]. These studies point to DOT as a strong candidate for diagnosis and monitoring in modern breast cancer treatments and regiments that are targeted and unique to patients.

1.3 Diffuse Optical Tomography instrumentation

Presently, a few groups are exploring DOT, and as of yet no consensus of its best implementation has come about. Part of the problem is that DOT is quite flexible in its possible configurations, and each configuration has its own set of advantages and disadvantages. Typically, DOT systems vary in number of wavelengths used, number and arrangement of source-detector pairs, detection techniques, and, of course, algorithmic approaches.

Multi-spectral systems permit robust imaging of multiple chromophores, in part because *a priori* spectral information about each chromophore exists and can be utilized. Many DOS and DOT systems will employ at least two wavelengths, but the best systems employ more wavelength which generally permit the quantification of more chromophores. Source-detector arrangements vary too. Most employ either the remission or transmission geometry. In the remission geometry, the source and detector are on the same side of the tissue surface; this configuration offers a great deal of flexibility and ease of measurement. Many remission systems, in fact, are handheld, and the optical properties of tissue located just below the probe are mapped out as the device is placed at several locations on the breast surface. One disadvantage of this geometry, however, is that the sensitivity function is depth-dependent, and the data are distorted to varying degrees with depth. Also, it is hard to penetrate too deeply in this geometry (e.g., the typical penetration is approximately one-half of the source-detector separation on the surface). In the transmission geometry, typical DOT source-detector arrangements include the ring [99–102] and the slab [53, 103, 104]. In general, transmission measurements provide much better sensitivity for deep tissues, since the detected light in this geometry is more likely to travel through all areas of interest.

These systems can be further divided by data-type, a property which also defines the experimental detection system and the nature of the experimental light sources. These data-types generally fall into three categories: continuous-wave (CW), frequency-domain (FD), and time domain (TD) (Figure 1.4). CW systems are the most simple; in this case the variation in light amplitude (fluence-rate amplitude) is measured. However, in these systems, the cross-talk between absorption and scattering is often severe; the cross-talk can be ameliorated via multi-spectral

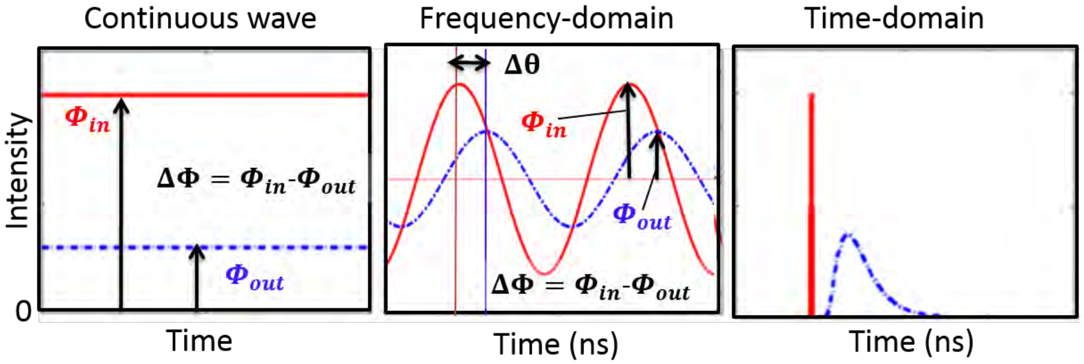

Figure 1.4: Schematic illustration of the three optical data types used in diffuse optical experiments. The input signal is colored red and the output (detected) signal is colored blue. Continuous wave (CW) techniques measure the change in fluence rate amplitude $\Delta\Phi$. The frequency-domain (FD) methods amplitude modulate the light sources and measure both $\Delta\Phi$ and the phase shift, $\Delta\theta$, between the input and output waveforms. The time-domain (TD) technique measures to amplitude and broadening of a very short incident pulse as it travels through the medium; TD methods can be thought of as a superposition of FD measurements with many modulation frequencies.

techniques [45, 105], but the situation is definitely not perfect! Frequency-domain systems employ laser light sources that are intensity modulated (typically in the 50 MHz to GHz range); in this scenario, a diffusive wave is injected into the tissue with amplitude and phase that evolve as the light travels through the turbid medium. By measuring the amplitude and phase of the output signal (e.g., as a function of position, modulation frequency, etc.), one can rigorously separate absorption *from* scattering contrasts. The FD detection scheme can be either homodyne or heterodyne. The data-types used in this thesis are either CW or FD. Time-domain (TD) systems use pulsed laser sources that inject short light pulses ($\leq$ps) into the turbid medium; these pulses broaden as they travel through the medium due to the different photon trajectories, and their broadening is measured by sophisticated time-correlated photon counting detection systems. Like FD systems, the TD methods also permit separation of scattering from absorption. The TD and FD experiments are essentially Fourier analogs. Numerous arguments have arisen in the community about whether TD is superior to FD or vice versa; these questions are still not resolved. Many factors come into play in analyzing these questions, ranging from duty cycle for best signal-to-noise, to detection systematic errors, to cost.

1.4 Diffuse Optical Tomography of Breast Cancer at Penn

DOT and, more generally, diffuse optics has had a long history at Penn. For example, the first experimental tomographic reconstructions of absorption and scattering heterogeneities were demonstrated at Penn [33]; similarly the first fluorescent lifetime tomography with diffuse optics was carried out here [9], as was the first fluorescence breast cancer imaging in humans [49]. In a different vein, numerous comparison and validation studies of DOT and other imaging modalities were performed here, including with PET [106] and MRI [47]. Further, instruments have been developed that combine DOT with other modalities such as ultrasound [107, 108] and MRI [12, 38, 109, 110]; this approach enhances the ability of optics to extract functional information about tissues by using structural information provided by other techniques to constrain the inverse problem.

Parallel to this experimental work, our group has developed theoretical approaches for DOT, including important research that shed light on the use and value of multiple optical wavelengths (and the optimization of the wavelength choice) for clinical DOT and DOS devices [45, 105]. Experiments characterizing (and pushing) the resolution of stand-alone DOT imaging were carried out [52], and a clinical DOT breast imaging device (Gen2) was built and used in a 47 patient study; the latter study demonstrated statistically significant differences in DOT contrast between malignant and benign lesions [53]. From this research, we have learned that it is possible to use optical imaging as a clinical and a research tool to advance our understanding of breast cancer physiology and treatment.

In my thesis I present my work to build on this previous success at Penn, i.e., my work pushes the frontier further in order to translate DOT into the clinical setting. Specifically, I explored and addressed clinically relevant issues for DOT imaging such as the effect of the chest wall, and I designed and built the next generation DOT breast imaging device. This new instrument will advance the clinical application of DOT in terms of resolution and image fidelity (i.e., due substantially to the enormous amount of data obtainable from the new instrumentation and signal normalization/calibration in-situ), information content (i.e., due to separation of absorption and scattering contrast with frequency-domain detection), and overall image quality (i.e., due to improved patient interfaces, etc.). Finally, I have begun to reconstruct images using the instrument in tissue phantoms and in the clinic.

1.5 Thesis Organization

The remainder of this thesis is organized as follows. In Chapter 2, I review the underlying theory of diffuse light propagation in tissue, as well as selected image reconstruction techniques (especially ones that I employ for my experiments). Specifically, I derive analytical solutions in frequency domain for the geometries and boundary conditions commonly used in diffuse optical tomography. I also describe the linear and nonlinear methods used to solve the forward and inverse problems that are utilized in my experimental image reconstructions.

Chapter 3 describes a (published) benchtop experiment wherein I systematically explore diffuse optical tomography in the clinically relevant slab geometry in the presence of the chest wall. The effect that the chest wall has on DOT reconstructions is not understood. The chest is highly absorptive tissue that breaks the symmetry of the inverse problem, among other things. DOT reconstruction methods have not been systematically studied in this important regime. The use of a high spatial-density of source-detector pairs helps us to characterize the resulting systematics and also enables us to explore various schemes to mitigate these chest wall effects.

Chapter 4 introduces, explains, and characterizes the new Gen3 breast imaging instrument; then I describe first imaging tests with the instrument. These first experiments are deployed in the lab (with tissue phantoms) and then in the clinic. Details of the optics, electronics, detection are provided in Section 4.3. Details of the data processing and signal correction/normalization are discussed in Section 4.4. The design, construction, and testing of this instrument is the most important research in this thesis. The image reconstruction research takes the first of many steps towards clinical DOT investigations, and teaches us about important issues in image regularization with DOT. Data and image reconstructions from simulation and tissue phantom experiments highlight the multi-spectral and frequency-domain capabilities of the device. Finally, the first clinical image reconstructions from cancer patients are shown; with these first images, I establish that more work is needed to find the best algorithms for the apparatus, but the work helps to define these new directions for research. Chapter 5 summarizes my work and offers suggestions for further development of the research.

Chapter 2

Theory

2.1 Modelling of light propagation in tissue

Photon migration through turbid media such as human tissue is usually well described by the radiative transport equation [5, 54]. The radiative transport equation, in turn, is well approximated by the diffusion equation for the photon fluence rate when the medium has low absorption but substantial scattering [5, 6]. The derivation of the photon diffusion equation from the transport equation can be traced back to nuclear transport theory [7], and the reader who is interested in the passage from the transport to diffusion equation should consult several useful review articles [54, 111, 112]. Herein, we will assume the diffusion approximation is valid for the media we investigate, i.e., human tissues. Thus, for the purposes of this thesis, in a media with low absorption and high scattering, we will assume that the photon fluence rate $\Phi(\mathbf{r}, t)$ (W/cm^2) obeys the diffusion equation:

$$\nabla \cdot (D(\mathbf{r})\nabla\Phi(\mathbf{r}, t)) - v\mu_a(\mathbf{r})\Phi(\mathbf{r}, t) + S(\mathbf{r}, t) = \frac{\partial\Phi(\mathbf{r}, t)}{\partial t}. \tag{2.1}$$

Here $\mathbf{r}$ represents position in the sample, t is time, v is the speed of light in the medium (i.e., c/n where c is the speed of light in vacuum and n is the index of refraction of the medium), $\mu_a(\mathbf{r})$ (cm^{-1}) is the tissue absorption coefficient, $D(\mathbf{r}) = \frac{v}{3(\mu_a(\mathbf{r})+\mu_{\mathbf{s}}'(\mathbf{r}))}$ is the tissue diffusion coefficient wherein $\mu_s'(\mathbf{r})$ (cm^{-1}) is the tissue reduced scattering coefficient, and $S(\mathbf{r},t)$ $(\mathrm{W/cm}^3)$ is the light source term. In the near-infrared (NIR) wavelength range, typical optical properties of the human breast are $\mu_a \sim 0.05\,\mathrm{cm}^{-1}$ and $\mu_s' \sim 8\,\mathrm{cm}^{-1}$.

The experiments in this thesis employ frequency-domain (FD) techniques. In the frequency-domain, the light source is typically point-like in space (which we often model with a delta function) and is modulated sinusoidally at an angular frequency ω. In this case, the source and resulting photon fluence rate have DC and AC components.

$$\begin{aligned} S(\mathbf{r},t) &= [S_{dc} + S_{ac}e^{-i\omega t}]\delta(\mathbf{r}-\mathbf{r}_s)\ ; && (2.2) \\ \Phi(\mathbf{r},t) &= \Phi(\mathbf{r})_{dc} + \Phi(\mathbf{r})_{ac}e^{-i\omega t}\ . && (2.3) \end{aligned}$$

Here S_{dc} is the DC light source power density (with units (W/cm^3)), S_{ac} is the AC light source power density, and $\mathbf{r}_s$ is the source location. Equation (2.2) shows that the photon fluence rate also has corresponding AC and DC components. Note, here the equations are expressed using complex notation; in this case, we expect that the AC components for both the source and the fluence rate to be complex. In later chapters, we are mainly concerned with the phase and the amplitude of the AC component of the fluence rate. Substituting for the light source and fluence rate from the two equations above into the diffusion equation, one readily derives the following frequency-domain diffusion equation i.e., equation for the AC component of the fluence rate:

$$[-\nabla \cdot D(\mathbf{r})\nabla + v\mu_a(\mathbf{r}) - i\omega]\Phi(\mathbf{r},\omega) = S\delta(\mathbf{r}-\mathbf{r}_s)\ . \tag{2.4}$$

For clarity, I have suppressed the AC subscript, and explicitly written the frequency dependence, ω, into the argument of the fluence rate in order to remind the reader of its importance. Equation (2.4) is the starting point for most of the analyses in this thesis, including the tomographic image reconstruction algorithms. However, before we delve into the tomographic reconstruction, we will solve this equation analytically for some common and simple geometries: homogeneous infinite media, semi-infinite media and slab media.

2.1.1 Boundary Conditions

To find a complete solution to any differential equation, one needs boundary conditions. For infinite medium, the primary requirement is for the photon fluence rate to reduce to zero at infinity. However, in practice, most important situations involve interfaces between diffuse and non-diffuse media, e.g., the air-tissue interface. The boundary condition problem has been discussed in books and review papers [54, 113–116]. Here I provide a review of the key results without detailed derivations.

To accomplish this task, we must return to the transport equation and its key functional quantities. Consider a small volume element centered on the point at $\mathbf{r}$. The radiance L ($\mathrm{W/m^2sr^1}$), is a measure of the light energy per unit area per unit solid angle at $\mathbf{r}$ and traveling in the direction $\mathbf{s}$. Thus, the isotropic fluence rate, $\Phi(\mathbf{r},t)$ in the diffusion equation above is obtained by integrating the radiance over all possible angles/directions; the associated photon flux, $\mathbf{j}(\mathbf{r})$, is the vector sum of the radiance emerging from the volume element:

$$\Phi(\mathbf{r}) = \iint_{4\pi} d\Omega\, L(\mathbf{r},\mathbf{s}) \; ; \tag{2.5}$$

$$\mathbf{j}(\mathbf{r}) = \iint_{4\pi} d\Omega\, L(\mathbf{r},\mathbf{s})\, \hat{\mathbf{s}} \; . \tag{2.6}$$

In the diffusion approximation, which is also called the P_1 approximation because it only retains spherical harmonics of order zero and one from the transport equation, the radiance only depends on the fluence rate and photon flux. Specifically, at any point, $\mathbf{r}$, the radiance is simply the sum of the isotropic fluence rate at $\mathbf{r}$ plus an additional term involving the dot product of the photon flux at $\mathbf{r}$ and the unit vector along $\mathbf{s}$, i.e.,

$$L(\mathbf{r},\mathbf{s}) = \frac{1}{4\pi}[\Phi(\mathbf{r}) + 3\mathbf{j}(\mathbf{r}) \cdot \hat{\mathbf{s}}] \; . \tag{2.7}$$

Typically, we study diffuse media (like tissue) that are bounded by non-diffuse media (like air). Therefore, we must carefully consider what happens to the radiance at the air-tissue boundary (see Fig. 2.1.1). Let $\hat{\mathbf{n}}$ be the outward unit normal on the tissue surface, and let $\hat{\mathbf{s}}$ define a direction of the light radiance propagation. In this case, the radiance exiting and entering the tissue at the boundary is determined, respectively, by integrating the radiance over all outward directions ($L(\mathbf{s})(\hat{\mathbf{s}} \cdot \hat{\mathbf{n}})$) and integrating the radiance over all inward directions ($L(\mathbf{s})(\hat{\mathbf{s}} \cdot -\hat{\mathbf{n}})$). Since air is non-scattering medium, the only light radiance that can enter the tissue from the boundary is due to Fresnel (specular) reflections of outgoing light radiance at the boundary. Let $R(\mathbf{s})$ be the Fresnel reflection coefficient for unpolarized light at the angle θ (where $\hat{\mathbf{s}} \cdot \hat{\mathbf{n}} = \cos\theta$

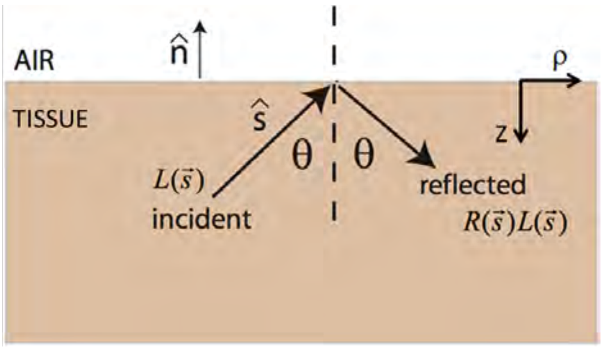

Figure 2.1: At the air-tissue boundary, a fraction of the incident radiance $L(\hat{s})$ is Fresnel reflected ($R(\hat{s})$) back into the turbid medium due to index mismatch. This reflected light $R(\hat{s})L(\hat{s})$ accounts for all light diffusing inwards into the medium at the boundary. The boundary condition is derived using this observation. $\hat{n}$ is the unit vector normal to the air-tissue boundary. z increases downward into the tissue and ρ is parallel with the boundary.

and $\hat{\mathbf{j}} \cdot \hat{\mathbf{n}} = j_z \cos\theta$), then

$$\int\!\!\iint_{\hat{\mathbf{s}}\cdot\hat{\mathbf{n}}>0} R(\mathbf{s})L(\mathbf{s})(\hat{\mathbf{s}}\cdot\hat{\mathbf{n}})d\Omega = \int\!\!\iint_{\hat{\mathbf{s}}\cdot\hat{\mathbf{n}}<0} L(\mathbf{s})(\hat{\mathbf{s}}\cdot -\hat{\mathbf{n}})d\Omega \; . \tag{2.8}$$

The solution of this equation leads us to the well-known partial-flux boundary condition [113, 115], i.e.,

$$\Phi + \ell\nabla\Phi\cdot\hat{\mathbf{n}} = 0 \; ; \tag{2.9}$$

$$\ell = 2D\frac{1+R_{eff}}{1-R_{eff}} \; . \tag{2.10}$$

Here R_{eff} is the effective reflection coefficient due to the index of refraction differences at the interface [117, 118]. The positive parameter, ℓ (Equation 2.10), is called the extrapolated boundary length; it corresponds to the distance (along the direction normal to the interface) for which the solution to Equation 2.9 is zero. (Note, this result is obtained with the Taylor expandsion of the fluence rate around its value at the interface, while keeping only the terms up to first order). Again, the details of this approach have been worked out in [54, 113–115], and I will not carry out the derivation here. The resulting so-called extrapolated boundary condition is:

$$\Phi(z = -\ell) = 0 \; . \tag{2.11}$$

We will use this extrapolated boundary condition to construct the Green's functions for semi-infinite and slab media. These Green's functions (or some equivalent form), in turn, facilitate solution of the problem when the turbid medium is heterogeneous. Of course, this latter situation is important for imaging inside a breast with cancerous lesions.

2.1.2 Analytical Solutions

This section covers three analytical solutions to the photon diffusion equation. We will solve for the fluence rate, Φ, in homogenous turbid media in the infinite, the semi-infinite, and the slab geometries. For the infinite medium, we will derive the Green's function. For the semi-infinite and slab problems we will use the method of images and the extrapolated boundary condition to derive new Green's functions.

2.1.2.1 Infinite Geometry

The simplest case we consider is the infinite geometry. Starting with the diffusion equation in the frequency domain (Equation 2.4), we assume that both the diffusion coefficient and the absorption coefficient of the medium are constant (i.e., the medium is homogeneous). Further, we assume that the point light source sits at the origin of the coordinate system. After dividing both sides by D, and defining the constant $k_0^2 = \frac{-v\mu_a^0 + i\omega}{D}$, (Equation 2.4) can be written in the following Helmholtz-like form:

$$(\nabla^2 + k_0^2)\Phi(\mathbf{r}, \mathbf{r}_s) = -\frac{S}{D}\delta(\mathbf{r} - \mathbf{r}_s)\ . \tag{2.12}$$

Note, in this form, the photon fluence rate, Φ, due to a point source is proportional to the Green's function solution (in this case the proportionality constant is S/D) for the Helmholtz equation (i.e., for the Helmholtz-like equation above with the unusual wave-vector). This equation for the Green's function with point source at $\mathbf{r_s}$ is:

$$(\nabla^2 + k_0^2)G(\mathbf{r}, \mathbf{r}_s) = -\delta(\mathbf{r} - \mathbf{r}_s)\ . \tag{2.13}$$

With the boundary condition that the fluence rate goes to zero at infinity we obtain the well-known result:

$$G(\mathbf{r}, \mathbf{r}_s) = \frac{1}{4\pi}\frac{e^{ik_o|\mathbf{r}-\mathbf{r}_s|}}{|\mathbf{r} - \mathbf{r}_s|}\ . \tag{2.14}$$

This Green's function solution is an overdamped spherical wave that vanishes at infinity. The wave-vector has real and imaginary parts that depend on the absorption coefficient, the reduced scattering coefficient, and the modulation frequency. The photon fluence rate solution is computed by spatial convolution of the Green's function and source distribution (which can originate at only a single point, but need not).

2.1.2.2 Semi-infinite Geometry

Now that we have the Green's function solution for infinite media, it is straight-forward to derive related solutions in the semi-infinite geometry. A key assumption from the partial-flux boundary condition facilitates the solution: the fluence rate is zero at the so-called extrapolated boundary (which is typically close to the real air-tissue boundary) [113–115]. Thus, if we know the source position, then we can use the method of images to construct our Green's function such that it vanishes at the extrapolated boundary. Recall that the extrapolated zero boundary is located a distance ℓ from the air-diffusive media interface ($z = 0$) as shown in figure 2.2.

The solution for the semi-infinite geometry can be readily determined using the well-known method of images. If a source exits some distance $\ell + z_s$ away from the extrapolated boundary (i.e., in the turbid medium), then we must place a sink the same distance on the opposite side of the boundary to insure that the net fluence rate at the extrapolated boundary position (i.e., between the real and image sources) is zero (see figure 2.2). This method-of-images approach yields the Green's function for the semi-infinite medium. The Green's function with the source and image source is

$$G(\rho_s, z_s; \rho, z) = \frac{1}{4\pi}\left(\frac{exp[ikr_+]}{r_+} - \frac{exp[ikr_-]}{r_-}\right); \tag{2.15}$$

$$\begin{aligned} r_+ &= \sqrt{(\rho - \rho_s)^2 + (z - z_+)^2}\ ; \\ r_- &= \sqrt{(\rho - \rho_s)^2 + (z - z_-)^2}\ . \end{aligned} \tag{2.16}$$

Here $z_+ = z_s$ is the position of the source and $z_- = -2\ell - z_s$ is the position of our image source. Note, typically the source position due to a light fiber located at the air-tissue interface is set to be at a distance (into the diffuse medium) equal to the reciprocal of the reduced scattering coefficient and measured from the air-tissue interface at $z = 0$. Finally, as was the case for

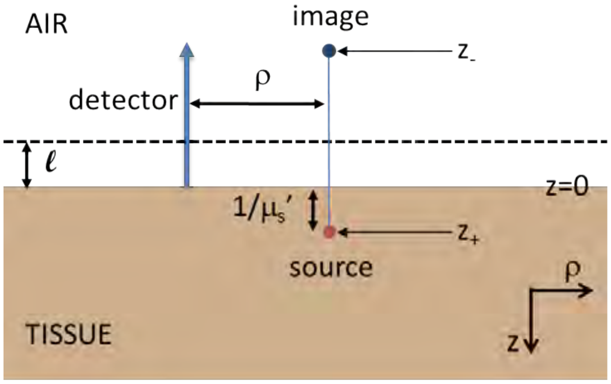

Figure 2.2: The semi-infinite case where the method of images is used to find the solution of the Green's function. The z direction increases downwards into the medium. z_+ is the location of the source, z_- is the location of the image sink, and $z = 0$ is the boundary between the tissue and air. The dotted line is where the extrapolated boundary is located a distance ℓ away from the boundary. ρ is the distance between the source and detector fibers.

the infinite medium, the photon fluence rate solution is computed by spatial convolution of the Green's function and source distribution (which can originate at a only one point, but need not).

2.1.2.3 Slab Geometry

The solution for the slab geometry is just a more complicated variant of the solution for the semi-infinite case. We use the method of images again. This time, however, there is a second boundary, and we again make the assumption that $\Phi = 0$ some distance ℓ away from the air/diffuse-media boundary for the second interface at $z = L$. As in the semi-infinite case, we add an image sink above the top ($z = 0$) boundary, but now we also need to add another image sink below the bottom ($z = L$) boundary to the source.

Notably, every additional sink that is added would need its own image source, leading to a recursive procedure of adding sources and sinks. Therefore a pattern in the position of these sources and sinks emerge, and the Green's function for the original source and all the images

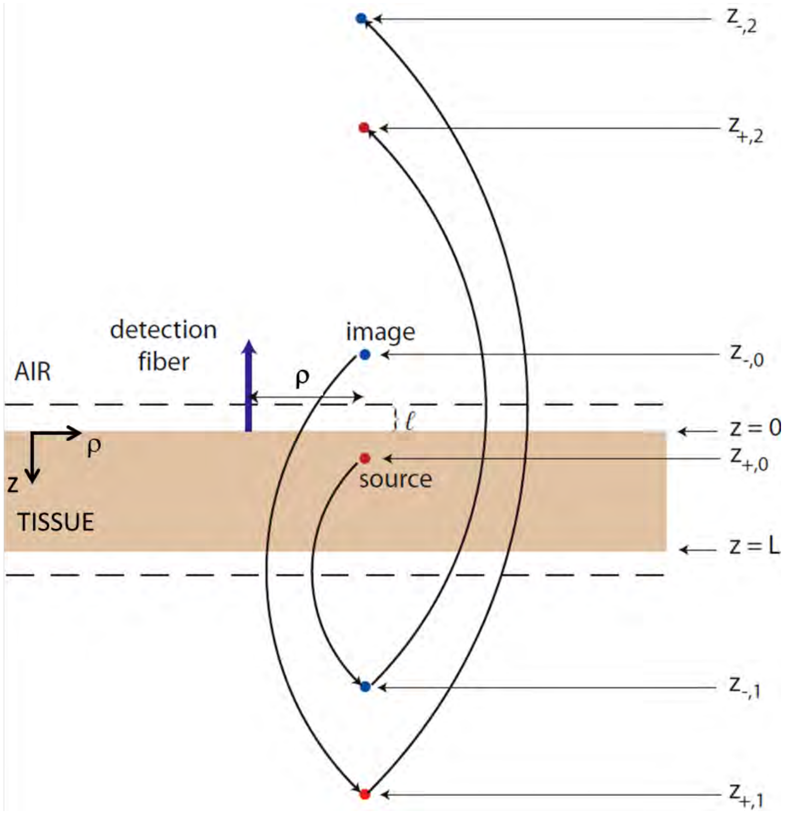

Figure 2.3: The slab case where the method of images is used to find the solution of the Green's function. $z_+, 0$ is the location of the source, $z_-, 0$ is the location of the image sink, $z_+, 1$ is the first source image, $z_-, 1$ is the 2nd sink image and so on. $z = 0, L$ is location of the boundaries between the tissue and air. The dotted line is where the extrapolated boundaries are located a distance ℓ away from the tissue/air boundaries. ρ is the distance between the source and detector fibers. z increases downwards into the slab.

can be written as an infinite sum:

$$G(\rho_s, z_s; \rho, z) = \frac{1}{4\pi} \sum_{m=-\infty}^{m=\infty} \left\{ \frac{exp[ikr_{+,m}]}{r_{+,m}} - \frac{exp[ikr_{-,m}]}{r_{-,m}} \right\} ; \tag{2.17}$$

$$\begin{aligned} r_{+,m} &= \sqrt{(\rho - \rho_s)^2 + (z - z_{+,m})^2} \; ; \\ r_{-,m} &= \sqrt{(\rho - \rho_s)^2 + (z - z_{-,m})^2} \; . \end{aligned} \tag{2.18}$$

Here $z_{+,m} = 2m(L + 2\ell) + z_s$, $z_{-,m} = 2m(L + 2\ell) - 2\ell - z_s$, $m = 0, \pm 1, \pm 2, \ldots$, and L is the thickness of the slab. For the semi-infinite geometry, only the $m = 0$ term is used.

Again, typically the source position due to a light fiber located at the air-tissue interface is set to be at a distance (into the diffuse medium) equal to the reciprocal of the reduced scattering coefficient; $z_{+,m}$ is positive as measured from air-tissue interface at $z = 0$. Also, the terms in the sum are decreasing in size with distance of the image sources from the primary interface, so one typically does not have to keep too many terms to obtain good agreement between theory and experiment. Finally, as was the case for the infinite medium, the photon fluence rate solution is computed by spatial convolution of the Green's function and source distribution (which can originate at only one point, but need not).

2.1.3 Multi-spectral Methods

2.1.3.1 Chromophore Absorption

In tissues and other turbid media, the total absorption, μ_a, is dependent on the relative concentrations of chromophores within the medium. If the number of chromophores is N, and they have spatial concentration distributions $c_i(\mathbf{r})$,($i = 1..N$), then

$$\mu_a(\lambda, \mathbf{r}) = \sum_{i=1}^{N} \Bigg(c_i(\mathbf{r}) \varepsilon_i(\lambda) \, . \tag{2.19}$$

Here λ is the wavelength of the probing light, and ε_i is the wavelength-dependent extinction coefficient of chromophore i. The ε_i are typically known from independent spectral measurements. Notice, it is possible to determine the chromophore concentrations, c_i, using this linear relationship. That is, the chromophore concentrations can be reconstructed directly from measurements of the absorption coefficient (μ_a) at multiple wavelengths λ_j ($j = 1..M$), provided the number of independent equations (M) is equal to or greater than the number of unknowns (N).

In breast tissue, the major chromophores are deoxy- (Hb), oxy-hemogloblin ($\mathrm{HbO_2}$), lipid, and water (H_2O) in the near-infrared (NIR) wavelength range. The extinction coefficients for these chromophores are known [119–122]. Furthermore, typical concentration values are known for breast, and this knowledge often helps to provide bounds/constraints on the allowed absorption in tomographic reconstructions. In our reconstructions in Chapter 4 the volume concentrations of water and lipid in the breast is assumed based on values from the literature [123–125].

Various analysis schemes are employed to extract physiological concentration information from the wavelength-dependent data. The traditional method determines an absorption coefficient at each wavelength, and then employs the equation above to extract chromophore concentrations. However, it is also possible to use all data at all wavelengths simultaneously to reconstruct chromophore concentrations. This latter, so-called multi-spectral approach has been shown to stabilize the reconstructions and to improve concentration fidelity [45, 126, 127], provided that enough wavelengths are utilized.

2.1.3.2 Scattering: Spectral Signatures from Mie Theory

In tissue, the scattering properties are due to a number of factors, especially organelles (e.g., mitochondria, nuclei, cells, cell/tissue interfaces) and their concentration. In practice, the scattering coefficient, μ_s', has been found to exhibit a power law variation as a function of wavelength in the NIR. Interestingly, this power law follows from a Mie scattering analysis too; the simplest Mie analysis assumes that all of the scattering is due to spherical particles of fixed size, but more complex analyses can add in particle size polydispersity, etc.

Mie scattering is a theory for light scattering from spherical particles based on Maxwell's equations. It is quite general, and it becomes especially important to use when the wavelength of the incident light becomes comparable to the particle size.

Although Mie theory is old, its application to scattering in tissues in this context is relatively recent [119, 122, 128]. If we assume a Mie scattering model as described above, then the wavelength dependence of the scattering coefficient, μ_s', has a power-law form:

$$\mu_s'(\lambda, \mathbf{r}) = a(2\pi\varrho n_m)^b \lambda^{-b}. \tag{2.20}$$

Here a is a constant that is proportional to the scatterer density, ϱ is the radius of the spheres, n_m is the index of refraction of the medium, and b is the scattering power. In biomedical optics, this equation is often further simplified to

$$\mu_s'(\lambda, \mathbf{r}) = A(\mathbf{r})\lambda^{-b} . \tag{2.21}$$

Here A is called the scattering prefactor. A few papers have been published that fit scattering spectra from tissues, and, generally, b is found to vary between 0.5 and 3 [122, 128]. Notice, the spatial distribution of scattering model parameters, A and b, can in principle be independently reconstructed from multi-spectral data [105]. However, it is quite common for experimenters to assume a fixed value for b and then reconstruct A and hence determine μ_s'. Since the NIR spectral range is not too broad, the scattering wavelength dependence is useful to employ in the reconstructions, which are often not very sensitive to the exact values of A and b in lieu of μ_s'.

2.2 Reconstruction Methods

The main rationale for using Diffuse Optical Tomography (DOT) in breast cancer imaging is that tumors have different physiological properties, such as vasculature, metabolic activity, organelle concenrations, and more, compared to surrounding healthy tissue. Furthermore, these differences in physiological properties are reflected as differences in optical properties, such as absorption and scattering coefficients.

Typical DOT instruments send photons into tissue at known points on the tissue surface (sources); output light that has traveled through the breast is then detected at known locations on the breast tissue surface (detectors). Importantly, this work is carried out in geometries that can be modeled reasonably with Green's function-based inverse problem approaches. Within these schemes, we utilize the measured data to solve for unknown μ_a and μ_s' values in each volume element of the 3-dimensional image-space for the medium. Common reconstruction methods require two basic steps: 1) solving the forward problem and 2) solving the inverse problem (see Fig. 2.4).

The forward problem, in essence, involves solving the diffusion equation for the fluence rate at known locations (e.g., within the medium or at the detector positions). The forward solution is readily determined, provided we are given specific values of μ_a and μ_s' in each volume element within the sample, as well as information about input source locations and the tissue boundaries.

Solving the inverse problem is conceptually and technically more difficult than the forward problem. It involves determining new values of μ_a and μ_s' from a comparison of the fluence rate at the boundary to the forward problem solution. Generally, as experimenters, we have knowledge about the diffuse light that we send into the medium and about the light that we

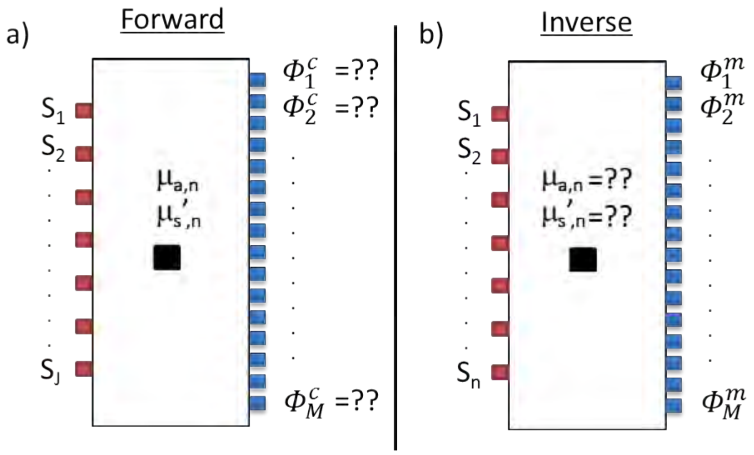

Figure 2.4: a) Forward problem diagram (model) for slab geometry. The forward problem calculates the fluence Φ_{model} at detector locations, given values for the source (S) locations as well as μ_a and μ_s' at N voxel locations inside the turbid medium. b) Inverse problem diagram (experimental). From the measured value for the fluence at the boundaries Φ_{data}, and the calculated fluence rate from the forward problem, the values for μ_a, μ_s' are updated/calculated.

measure after its emergence from the medium. The task of the inverse problem is to find unique solutions for the optical properties inside the medium, given this information.

For the forward problem, general theoretical approaches can be divided into three groups: Analytical methods, Numerical methods, and Monte-Carlo (MC) methods. These schemes range, respectively, from least to most computationally demanding. The analytical method is the fastest and easiest scheme (if we can figure out the analytic solution); given the source distribution, sample geometry, and optical properties, all that is required is a Green's function to generate the fluence rate within the medium (and on its boundaries). In principle, these analytical or semi-analytical approaches are well suited to use with very large data sets. However, the analytical approaches have limitations. These limitations come, in part, from true experimental geometries that differ from ideal cases and other experimental limitations such as small heterogeneities in the medium. Numerical methods, though more computationally intensive, are a bit more versatile. For example, by using numerical schemes, the number of assumptions about geometry are reduced, and it is possible to utilize well-worn techniques such as the Finite Element Method (FEM) and Finite Difference Method (FDM). The Monte-Carlo approach is a stochastic method which employs random step or Markov-chain models to account for transport of photons through the tissue; each of these photon trajectories is traced through the medium, with probability of absorption and scattering events included, until the photon exits or is absorbed. Though probably the most accurate method, this procedure employs a large number of photons ($> 10^8$) and thus very computationally and time intensive. Of the methods described above, we will primarily investigate the first two groups.

The inverse problem is inherently more difficult than the forward problem; it involves the inversion of matrices (or similar/related mathematical operations). Such inversions are necessary to solve/update μ_a and μ_s' from the measured and calculated fluence rates. Standard inversions of the resulting sets of linear equations are non-trivial. For example, they can involve generating a pseudoinverse matrix (e.g., using singular value decomposition (SVD)). These operations are fast but are susceptible to large deviations due to the ill-conditioned matrices and noise, among other factors. A different approach to derive a solution is iterative and nonlinear (to varying degrees). In the nonlinear case, an iterative approach is utilized wherein the measured fluence is compared to the forward model (e.g., FEM model) solution of the diffusion equation using a cost function $\boldsymbol{\Psi}$ (see Section 2.2.2.2). The key iteration step chooses a direction in the solution-space and calculates (e.g., using either the Conjugate-Gradient (CG) method or the Gauss-Newton (GN) method) new optical property parameters; then the forward problem is solved again (with the new optical properties) and the iteration steps are repeated until a pre-set convergence criteria is reached. The nonlinear methods, while more accurate and flexible, are computationally very expensive and time consuming, especially when the data sets and the number of volume elements are large.

In the following sections we describe two inverse problem approaches using analytic (Section 2.2.1.2) and algebraic (Section 2.2.1.4) linear schemes. Further, these reconstructions are used to analyze the experimental data described in Chapter 3. We will also discuss a nonlinear reconstruction method which is used for the experimental data in Chapter 4.

2.2.1 Linear Reconstruction Methods

2.2.1.1 Linearized Integral Equations

Here we derive linear solutions to the diffusion equation (2.4) in turbid media with heterogeneities. To simplify our problem, we divide the absorption and scattering (i.e., light diffusion coefficient) parameter into two parts: homogeneous background components and spatially heterogeneous (i.e., perturbative) components:

$$\mu_a(\mathbf{r}) = \mu_a^0 + \delta\mu_a(\mathbf{r}) \; ; \tag{2.22}$$

$$D(\mathbf{r}) = D^0 + \delta D(\mathbf{r}) \; . \tag{2.23}$$

We use/substitute this perturbation expansion of the optical properties into the diffusion equation (Equation 2.4) in the presence of a single **point source** at $\mathbf{r}_s$ (and we replace the fluence rate, Φ, with the corresponding Green's function, G). Note, again, formally the fluence rate in this situation, $\Phi(\mathbf{r}_s, \mathbf{r})$, is proportional to the Green's function, $G(\mathbf{r}_s, \mathbf{r})$. Rearranging this resulting equation as described, we obtain:

$$\left[-D^0\nabla^2 + v\mu_a^0 - i\omega\right] G(\mathbf{r}_s,\mathbf{r}) = \delta(\mathbf{r}-\mathbf{r}_s) - \Big[v\delta\mu_a(\mathbf{r}) - \nabla\cdot\delta D(\mathbf{r})\nabla\Big] G(\mathbf{r}_s,\mathbf{r}) \, . \qquad (2.24)$$

The LHS of this equation is essentially the homogeneous diffusion equation with average/background values of absorption and diffusion. The spatially heterogeneous perturbations introduce important additional terms on the RHS of the equation. These terms account for how the fluence rate propagation is modified by the heterogeneous perturbations. We can manipulate this equation to derive an expression for the Green's function, $G(\mathbf{r}_s,\mathbf{r}_d)$, for a particular source-detector pair where $\mathbf{r}_d$ is the detector position. The Green's function satisifes the Dyson equation:

$$G(\mathbf{r}_s,\mathbf{r}_d) = G_0(\mathbf{r}_s,\mathbf{r}_d) - \iiint_V G_0(\mathbf{r},\mathbf{r}_d)[\delta\mu_a(\mathbf{r}) - \nabla\cdot\delta D(\mathbf{r})\nabla]G(\mathbf{r}_s,\mathbf{r}) \; d^3r \, . \qquad (2.25)$$

Here the integral is taken over V, the full volume of our medium (i.e., the slab), and $G_0(\mathbf{r}_s,\mathbf{r}_d)$ is the analytic Green's function solution for the homogenous medium, i.e., homogenous slab, in this case.

This equation is intrinsically nonlinear, since $G(\mathbf{r}_s,\mathbf{r})$ depends on the optical properties too. Linearization involves the recursive substitution of the Green's function $G(\mathbf{r}_s,\mathbf{r})$ in the integrand, with Equation 2.25. The higher order terms are then neglected, leading to a linearized equation, where we have now excluded $G(\mathbf{r}_s,\mathbf{r})$ from the RHS. In addition, to simplify the notation, we let $\alpha(\mathbf{r}) = [v\delta\mu_a(\mathbf{r}) - \nabla\cdot\delta D(\mathbf{r})\nabla]$. The lowest order linear solution, as might be expected from any Born expansion, is:

$$G(\mathbf{r}_d, \mathbf{r}_s) = G_0(\mathbf{r}_d, \mathbf{r}_s) - \iiint_V G_0(\mathbf{r}_d, \mathbf{r})\alpha(\mathbf{r})\, G_0(\mathbf{r}_d, \mathbf{r}_s)\, d^3r\ . \tag{2.26}$$

If, instead of the Born approximation the first Rytov approximation [129] is adopted, Equation (2.26) yields:

$$G(\mathbf{r}_\mathrm{d}, \mathbf{r}_\mathrm{s}) = G_0(\mathbf{r}_\mathrm{d}, \mathbf{r}_\mathrm{s}) \exp\left[- \iiint_V \frac{G_0(\mathbf{r}_\mathrm{d}, \mathbf{r})\alpha(\mathbf{r})G_0(\mathbf{r}, \mathbf{r}_\mathrm{s})\, d^3r}{G_0(\mathbf{r}_\mathrm{d}, \mathbf{r}_\mathrm{s})}\right] . \tag{2.27}$$

Now let us connect this result to the data we might measure in an experiment. In practice, two independent measurements of the transmitted intensity are made. (Note, this intensity is derived from and is proportional to the diffuse light fluence rate at the output plane.) One measurement is made on a homogeneous (reference) media, and the another measurement is made on the medium with heterogeneities (i.e., the medium we want to understand). We denote these measurements by $I_0(\mathbf{r}_\mathrm{d}, \mathbf{r}_\mathrm{s})$ and $I(\mathbf{r}_\mathrm{d}, \mathbf{r}_\mathrm{s})$, respectively, where $\mathbf{r}_\mathrm{d}$ and $\mathbf{r}_\mathrm{s}$ are vectors specifying the positions of the detector and the source. Note, in my experimental work in Chapters 3 and 4, these quantities, I_0 and I, are ultimately derived from measured CCD counts in particular CCD pixels with specific integration times; the number of CCD counts in each pixel is linearly proportional to the corresponding photon fluence rate from the detected region. These measurements are readily connected to Green's function (which is also proportional to the fluence rate) and thus related to the optical properties of the sample medium through the relations:

$$I(\mathbf{r}_d, \mathbf{r}_s) = C_d(\mathbf{r}_d) C_s(\mathbf{r}_s) G(\mathbf{r}_d, \mathbf{r}_s)\ ; \tag{2.28}$$

$$I_0(\mathbf{r}_d, \mathbf{r}_s) = C_d(\mathbf{r}_d) C_s(\mathbf{r}_s) G_0(\mathbf{r}_d, \mathbf{r}_s)\ . \tag{2.29}$$

As noted above, $G(\mathbf{r}_d, \mathbf{r}_s)$ is the Green's function solution that is proportional to the fluence rate we should measure with our CCD. The quantities $C_d(\mathbf{r}_d)$ and $C_s(\mathbf{r}_s)$ are unknown coupling coefficients on the detectors and sources respectively. The coupling coefficients are cancelled out (in principle) when we normalize the true sample data by the reference measurement for the reconstructions (i.e., when we compute I/I_0).

We divide both sides of Equation 2.27 by G_0, and take the natural log of both sides of the resulting equation. Finally we multiply both sides by $-G_0$ and obtain:

$$-G_0(\mathbf{r}_\mathrm{d}, \mathbf{r}_\mathrm{s}) \ln \left[\frac{G(\mathbf{r}_\mathrm{d}, \mathbf{r}_\mathrm{s})}{G_0(\mathbf{r}_\mathrm{d}, \mathbf{r}_\mathrm{s})} \right] = \iint_V G_0(\mathbf{r}_\mathrm{d}, \mathbf{r}) \alpha(\mathbf{r}) G_0(\mathbf{r}, \mathbf{r}_\mathrm{s})\, d^3 r\ ; \tag{2.30}$$

$$\phi(\mathbf{r}_d, \mathbf{r}_s) = \iint_V G_0(\mathbf{r}_\mathrm{d}, \mathbf{r}) \alpha(\mathbf{r}) G_0(\mathbf{r}, \mathbf{r}_\mathrm{s})\, d^3 r\ . \tag{2.31}$$

Here we define the so-called Rytov data function, $\phi(\mathbf{r}_d, \mathbf{r}_s)$ as

$$\phi(\mathbf{r}_d, \mathbf{r}_s) = -G_0(\mathbf{r}_\mathrm{d}, \mathbf{r}_\mathrm{s}) \ln \left[\frac{I(\mathbf{r}_\mathrm{d}, \mathbf{r}_\mathrm{s})}{I_0(\mathbf{r}_\mathrm{d}, \mathbf{r}_\mathrm{s})} \right] . \tag{2.32}$$

Note, that the data function $\phi(\mathbf{r}_d, \mathbf{r}_s)$ is proportional to the measured fluence rate $\Phi(\mathbf{r}_d, \mathbf{r}_s)$. The right-hand side of the equation above contains the measured data function, and the left-hand side is an integral transform of the contrast within the sample. This formulation of the linearized

DOT inverse problem is standard [129].

2.2.1.2 Analytical Inverse Reconstruction

The analytical inverse reconstruction method that describe here and use in Chapter 3 was pioneered by my collaborators [52,130–135]. Its application in the slab geometry has been reported in Refs. [52, 136, 137]. In this method, the inverse problem is simplified by taking advantage of symmetries which reduce the complexity of the Green's function while also enabling simplified data inversions through the use of the Fourier transform. To achieve this goal, one first decomposes the Green's function into plane waves so that it has the following form:

$$G(\mathbf{r},\mathbf{r}') = \frac{1}{(2\pi)^3} \iiint d^3k \; g(k) \; e^{i\mathbf{k}\cdot(\mathbf{r}-\mathbf{r}')} \; . \tag{2.33}$$

Here $g(k)$ gives the amplitude and phase for each plane wave. For complex boundaries, it is impossible to solve for $g(k)$. However, for some simple symmetric geometries (i.e., semi-infinite, slab, cylindrical, spherical), formulas for the Fourier components can be derived [132].

Our experiments in Chapters 3 and 4 are carried out in the slab geometry. Therefore, we will study the specifics of the slab geometry. In the slab, we define $\mathbf{r} = (\rho, z)$ where z is depth in the medium and ρ is parallel to the surfaces (see Fig. 2.2.1.2). In the Fourier space, $\mathbf{k} = (\mathbf{q}, k_z)$. The form of the Helmholtz equation is thus modified:

$$(\nabla_\rho^2 + \frac{\partial^2}{\partial z^2} + k_0^2)G(\mathbf{r},\mathbf{r}') = \frac{-1}{D_0}\delta(\mathbf{r}-\mathbf{r}') \; . \tag{2.34}$$

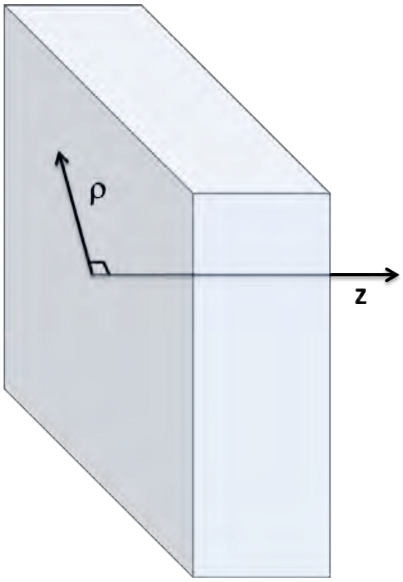

Figure 2.5: Coordinates in the slab geometry. The positive z direction points into the slab while ρ is parallel to the surface.

Since no translational symmetry exists in the z direction, we expand the Greens function in plane waves along ρ. Then

$$G(\mathbf{r},\mathbf{r}') = \frac{1}{(2\pi)^2}\iint d^2q\; g(q,z,z')e^{i\mathbf{q}\cdot(\rho-\rho')}\ . \tag{2.35}$$

Substitution of Equation 2.35 into Equation 2.34 gives a one-dimensional differential equation for each value of $\mathbf{q}$.

$$\left(\frac{\partial^2}{\partial z^2} - (q^2 - k_0^2)\right) g(q,z,z') = \frac{-1}{D}\delta(z-z')\ . \tag{2.36}$$

Although I will not write out the derivation here (see reference [52, 138]), please note that g(q,z,z') can be solved for in the slab geometry and has the form:

$$g(q; z, z') = \frac{\ell}{D} \frac{\sinh[Q(L - |z - z'|)] + Q\ell\cosh[Q(L - |z - z'|)]}{\sinh(QL) + 2Q\ell\cosh(QL) + (Q\ell)^2\sinh(QL)} \tag{2.37}$$

where $Q = q^2 - k_0^2$, L is the slab thickness, and ℓ is the extrapolated boundary distance.

2.2.1.3 Fourier Inversion Equations

We next derive the inversion equations. We begin by substituting the plane wave Green's function (Equation 2.35) into the linearized forward equation we must solve (i.e., Equation 2.31). This substitution yields the following equation for the data function:

$$\begin{aligned} \phi(\mathbf{r}_s, \mathbf{r}_d) = \;& \tfrac{1}{(2\pi)^4} \int d^2q_s \int d^2q_d \int d^3r \; g(q_d, z, z_d)\exp[i\mathbf{q}_d \cdot (\rho - \rho_d)] \; ; \\ & \times\alpha(\mathbf{r}) \; g(q_s, z_s, z)\exp[i\mathbf{q}_s \cdot (\rho_s - \rho)] \; . \end{aligned} \tag{2.38}$$

For discrete source-detector pairs, the Fourier transform and the substitution of $\mathbf{q} = \mathbf{q}_s + \mathbf{q}_d$, and $\mathbf{p} = -\mathbf{q}_s$, gives us a set of separate integral equations for each value of q:

$$\tilde{\phi}(\mathbf{q}_s, \mathbf{q}_d) = \int_{z_s}^{z_d} \left[\kappa_A(\mathbf{q}_s, \mathbf{q}_d; z) \; c \; \delta\tilde{\mu}_a(\mathbf{q}_s + \mathbf{q}_d) + \kappa_D(\mathbf{q}_s, \mathbf{q}_d; z) \; \delta\tilde{D}(\mathbf{q}_s + \mathbf{q}_d)\right] dz \tag{2.39}$$

where

$$\kappa_A(\mathbf{q},\mathbf{p};z) = g(-\mathbf{p};z_s,z)g(\mathbf{q}+\mathbf{p};z,z_d)\ ; \tag{2.40}$$

$$\kappa_D(\mathbf{q},\mathbf{p};z) = \frac{\partial g(-\mathbf{p};z_s,z)}{\partial z}\frac{\partial g(\mathbf{q}+\mathbf{p};z,z_d)}{\partial z} + \mathbf{p}\cdot(\mathbf{q}+\mathbf{p})\ g(-\mathbf{p};z_s,z)g(\mathbf{q}+\mathbf{p};z,z_d)\ . \tag{2.41}$$

Each integral in Equation (2.39) can be inverted independently, thereby reducing computation time. From these results, we obtain inverse equations for μ_a and D (and thus μ_s').

Specifically: 1) we compute the Fourier transform of Equation (2.38) to obtain Equation (2.39); 2) then we solve for $\delta\mu_a(\mathbf{q},z)$ and $\delta D(\mathbf{q},z)$ using singular value decomposition; 3) finally, the inverse Fourier transform for a given value of z is computed with the equations below.

$$\delta\mu_a(\mathbf{r}) = \frac{1}{(2\pi)^2}\iint\Bigg(d^2q\exp(-i\mathbf{q}\cdot\rho)\sum_{\mathbf{r},\mathbf{p}}\Bigg(\kappa_A^*(\mathbf{q},\mathbf{r};z)\ [\kappa\kappa^*]^{-1}(\mathbf{q},\mathbf{r},\mathbf{p})\tilde{\phi}(\mathbf{q},\mathbf{p})\ . \tag{2.42}$$

$$\delta D(\mathbf{r}) = \frac{1}{(2\pi)^2}\iint\Bigg(d^2q\exp(-i\mathbf{q}\cdot\rho)\sum_{\mathbf{r},\mathbf{p}}\Bigg(\kappa_D^*(\mathbf{q},\mathbf{r};z)\ [\kappa\kappa^*]^{-1}(\mathbf{q},\mathbf{r},\mathbf{p})\tilde{\phi}(\mathbf{q},\mathbf{p})\ . \tag{2.43}$$

Here $\kappa_A^*[\kappa\kappa^*]^{-1}$ is the SVD pseudoinverse.

As an aside, note that the computational complexity of the analytical reconstruction is $O(N_q N_p^3)$, where N_q is the number of discrete values of the vector $\mathbf{q}$, and N_p is the number of discrete values of $\mathbf{p}$ in Equation 2.39. In the numerical implementation of the analytical method in Chapter 3, we have closely followed reference [52] and used a total of $49\times3249 \simeq 1.6\times10^5$ independent Fourier-space data points. Using these parameters, the necessary computations require 7×10^9 floating point operations. On a single-core Intel Core 2 Duo processor with a peak performance of 19 GFlops, this calculation translates to 7 minutes of computation time.

2.2.1.4 Algebraic Method

In general, variants of the algebraic image reconstruction are among the most popular methods per linear inversion techniques that have been applied to DOT [33, 38, 139, 140]. These reconstructions are obtained by discretization of the volume integral in Equation (2.31) and subsequent computation of the pseudo-inverse of the obtained system of linearized equations [141]. This method does not require large windows (i.e., it does not need the large field-of-views which are required by symmetry in the analytic inversions), and it can be used with any type of data restriction. For the case of the analytical reconstruction method, on the other hand, for data restriction, it must be assumed that the data function $\phi = 0$ (see Equation (2.31) at these data points (i.e., $\Phi/\Phi_0 = 1$ at these restricted data points). On the other hand, the algebraic method requires explicit volume discretization in terms of voxels, while the analytical method allows one to reconstruct the target z plane without much additional effort and is not dependent on volume discretization.

For the purpose of obtaining algebraic reconstructions we divide the slab into cubic voxels. In the discretization we approximate the integral in Equation (2.31) with a Riemann sum, resulting in a system of algebraic equations $Ax = \phi$ where A_{mn} is the $M \times N$ weight matrix, where M is the number of distinct source-detector pairs, N is the number of voxels, $x_n = \delta\alpha(\mathbf{r}_n)/\alpha_0$ is the vector of dimensionless contrast $(n = 1, \ldots, N)$, and ϕ_m is the m-th data point $(m = 1, \ldots, M)$. The equations are cast in dimensionless form by defining a dimensionless Green's functions according to $\tilde{G}_0(\mathbf{r}, \mathbf{r}') = D_0 h G_0(\mathbf{r}, \mathbf{r}')$, where D_0 is the diffusion coefficient in the background solution. Then we have:

$$A_{mn} = (k_{\rm d} h)^2 \tilde{G}_0(\mathbf{r}_{{\rm d}m}, \mathbf{r}_n) \tilde{G}_0(\mathbf{r}_n, \mathbf{r}_{{\rm s}m}) \; ; \tag{2.44}$$

$$\phi_m = -\tilde{G}_0(\mathbf{r}_{{\rm d}m}, \mathbf{r}_{{\rm s}m}) \ln \left[\frac{I(\mathbf{r}_{{\rm d}m}, \mathbf{r}_{{\rm s}m})}{I_0(\mathbf{r}_{{\rm d}m}, \mathbf{r}_{{\rm s}m})} \right] \tag{2.45}$$

Here $k_d = \sqrt{\alpha_0 / D_0}$, $\mathbf{r}_n$ is the position of the center of the n-th voxel, and $\mathbf{r}_{{\rm d}m}$, $\mathbf{r}_{{\rm s}m}$ are the detector and source positions of the m-th data point used in the reconstruction.

The pseudoinverse solution to the above system of equations is defined as the unique solution to the system $(A^* A + \lambda^2 I)x = A^* \phi$, where λ is the regularization parameter and I is the identity matrix. In the experiments in Chapter 3, the number of measurements M is much larger than the number of voxels N (e.g., $M \sim 10^7$ and $N \sim 10^4$). Correspondingly, the most time consuming part of finding the pseudoinverse (at least, with the numerical approach we used) is the computation of the matrix product $A^* A$. In the most challenging case considered, we have used $M = 2 \times 10^7$ and $N = 2 \times 10^4$, which requires 8×10^{15} floating point operations.

On an 8-core Xeon workstation with the peak performance of 56 GFlops, this calculation translates into 40 hours of computation time. However, this time-consuming procedure need only be repeated once for a given source-detector arrangement and given optical properties of the background medium; this situation is the case for my experiment in Chapter 3. Importantly, the resultant matrix, $A^* A$, once computed, can be stored on a hard drive and re-used for image reconstruction with each new data set obtained, e.g., for various positions of the chest wall phantom. Furthermore, computation of the projection, that is, of the N-component vector $A^* \phi$, involves only one matrix-vector multiplication, and its computational cost is insignificant. In our case, the matrix $A^* A$ is small enough to be diagonalized; its eigenvectors and eigenvalues can be also stored on a hard drive for future use. In the reconstructions of Chapter 3, however, we solved the equation $(A^*A + \lambda^2 I)x = A^*\phi$ directly by the conjugate-gradient descent method [142].

2.2.2 Nonlinear Reconstruction Methods

For the approaches described thus far, the tomography problem was linearized. Ultimately, however, it is desirable to employ nonlinear methods to find the solution, because in general the relationship between the measurements made and the unknown optical parameters is nonlinear. Among the advantages of the nonlinear reconstruction methods is that one typically has no restrictions on the experimental geometry; further, no linear assumptions are made to solve the diffusion equation, i.e., as we did in Section 2.2.1.1. While these conditions usually result in the problem being computationally intensive and time consuming, this drawback is typically compensated with parallelization of the problem. The nonlinear method we employ in this thesis is a model-based reconstruction technique. A forward model of light propagation generates an expected fluence rate, and then we seek to iteratively minimize the differences between our measurement and our model (forward) data by updating the parameters in the forward model. The forward model (diffusion equation) is solved using the finite element method (FEM).

2.2.2.1 Finite Element Method

The FEM programs I employ are already standardized functions in most inversion software. Nevertheless, here I will quickly describe the basic premise of FEM for DOT, and I refer the interested reader to the literature for a more complete treatment [143, 144]. To solve the forward problem with FEM, we first define a diffusion equation operator $\mathcal{L} = -\nabla \cdot D(\lambda)\nabla + \mu_a(\lambda) + i\omega/v$

such that:

$$\mathcal{L}\Phi(\mathbf{r}) = q_0(\mathbf{r}) \; . \tag{2.46}$$

Here $q_0(\mathbf{r})$ is a our source term (note, it doesn't have to be a point source). The boundary condition used here is the Robin-type (partial flux) boundary condition:

$$\Phi(r_b) + \frac{D(z_b)}{\alpha}\hat{\mathbf{n}} \cdot \nabla\Phi(r_b) = 0 \; . \tag{2.47}$$

Here r_b is a point on the measurement boundary and α is a refractive index mismatch term [145]. Assuming that our detected signal is the normal component of the photon flux $\phi_m = \hat{\mathbf{n}} \cdot [-D(r_b)\nabla\Phi(r_b)]$, the equation in the case of the Robin boundary condition simplifies to

$$\phi_m(r_b) = \alpha\Phi(r_b) \; . \tag{2.48}$$

The volume Ω we are interested in imaging (in our case the slab) is discretized into V vertex nodes. If $u_i(\mathbf{r})$ is a basis function from a V-dimensional subspace, then the approximate piecewise continuous polynomial FEM solution to $\Phi(\mathbf{r})$ is

$$\Phi^h(\mathbf{r}) = \sum_i^V \Phi_i u_i(\mathbf{r}) \; . \tag{2.49}$$

The linear or higher order basis functions are defined over triangle (2D), tetrahedral (3D), or square grid elements (3D, used in TOAST++ [146]).

To find the appropriate basis vectors $u_i(\mathbf{r})$, we minimize the residual defined as:

$$\mathcal{L}\Phi(\mathbf{r}) - q_0(\mathbf{r}) = R, \tag{2.50}$$

$$= \sum_{i}^{V} R_i u_i(\mathbf{r}) \,, \tag{2.51}$$

by requiring that R be orthogonal to u_i (for $i = 1...V$) which in Equation 2.50 gives

$$(\mathbf{K}(D) + \mathbf{C}(\mu_a) + i\omega\mathbf{B} + \alpha\mathbf{A})\mathbf{\Phi} = \mathbf{Q} \,; \tag{2.52}$$

$$K_{ij} = \iint_{\omega} D(r)\nabla u_i(\mathbf{r}) \cdot \nabla u_j(\mathbf{r}) d\Omega \,; \tag{2.53}$$

$$C_{ij} = \iint_{\omega} \mu_a(r) u_i(\mathbf{r}) u_j(\mathbf{r}) d\Omega \,; \tag{2.54}$$

$$B_{ij} = \frac{1}{v} \iint_{\omega} u_i(\mathbf{r}) u_j(\mathbf{r}) d\Omega \,; \tag{2.55}$$

$$A_{ij} = \iint_{\omega} u_i(\mathbf{r}) u_j(\mathbf{r}) d(\Omega) \,; \tag{2.56}$$

$$q_{0,i} = \iint_{\omega} \mu_a(r) u_i(\mathbf{r}) q_0(\mathbf{r}) d\Omega \,. \tag{2.57}$$

Here $\mathbf{\Phi}$ is the FEM basis expansion coefficient vectors for $\Phi(\mathbf{r})$. These equations are the FEM discretization of the diffusion equation. Note that $\mathbf{K}, \mathbf{C}, \mathbf{B}$, and $\mathbf{A}$ are matrices of size $V \times V$. Equation (2.52) can can be inverted to give us our forward solver using Cholesky factorization (CW only), LU Decomposition, or iterative solvers like the Conjugate-Gradient method and GMRES.

2.2.2.2 The Inverse Problem

The central problem to image reconstruction lies in finding a solution vector $\hat{\mathbf{x}}$ that best fits the measurement data where

$$\mathbf{x} = [\mu_{a,1}, \cdots, \mu_{,V}, \mu'_{s,1}, \cdots, \mu'_{s,V}]^T \ . \tag{2.58}$$

The elements of $\mathbf{x}$ are μ_a and μ'_s (at a single wavelength) for every vertex of the volume that we want to reconstruct. A straightforward way to utilize multi-spectral data is to reconstruct $\mathbf{x}$ for each wavelength, and then convert μ_a and μ'_s to C_i (where i indexes the chromophore) and A using the relationship given by Equation (2.19) and (2.21). (Note, the exponent b can also be a free parameter if desired but is often fixed). It has been learned that multi-spectral methods stabilize various inverse problems [45, 105], so the preferred method (when the data quality is good for many wavelengths) is to reconstruct for C_i and A utilizing all the data simultaneously in the inversion. Then $\mathbf{x}$ is instead

$$\mathbf{x} = [C_{1,1}, \cdots, C_{1,V}, \cdots, C_{K,1}, \cdots, C_{K,V}, A_1, \cdots, A_V]^T \tag{2.59}$$

where the number of elements in $\mathbf{x}$ is $N = [(K+1) \times V]$.

Finding the solution vector $\hat{\mathbf{x}}$ can be approached as an optimization problem [147, 148] wherein the solution $\hat{\mathbf{x}}$ is found by minimizing an objective function

$$\hat{\mathbf{x}} = \arg\min_{\mathbf{x}} \Psi(\mathbf{x}) \ , \tag{2.60}$$

where above we search for some parameter x that returns the minimum of $\Psi(x)$. Here Ψ is defined

$$\Psi = \frac{1}{2}\sum_{l=1}^{L}\sum_{s=1}^{S}\sum_{d=1}^{D_s}\left[\Phi^c(\mathbf{x}) - \Phi^m\right]^2 . \tag{2.61}$$

The summations are over all source-detector pairs and wavelengths in the data sets, where L is the number of wavelengths, S is the number of source positions, and D_s is the number of detector positions for a given source. The total number of measurements is $M = L \times (\sum_{s=1}^{S} D_s)$. $\Phi^c(\mathbf{x})$ is the fluence rate calculated by our forward FEM (Section 2.2.2.1) and Φ is our measured fluence rate for a given source-detector pair, and thus the term to minimize is $[\Phi^c(\mathbf{x}) - \Phi]^2$. Fig. 2.6 is the flowchart for the image reconstruction algorithms. We start with an initial guess $\mathbf{x_0}$ for the

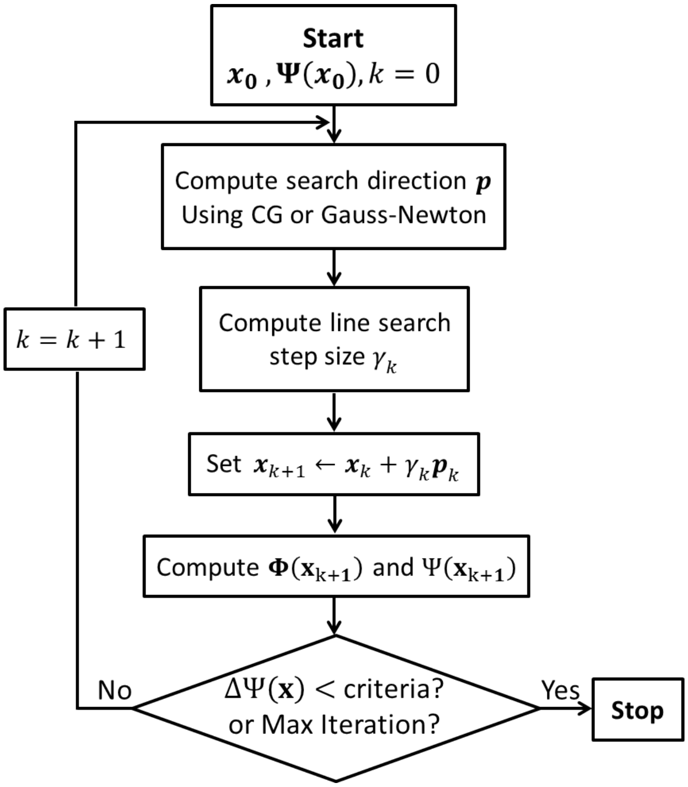

Figure 2.6: Reconstruction flowchart.

parameters, and then calculate the Ψ function by solving the forward problem for $\mathbf{\Phi^c}(\mathbf{x})$ and using the measured data $\mathbf{\Phi^m}$. The parameter vector $\mathbf{x_0}$ is updated by adding a scaled vector $\Delta\mathbf{x} = \gamma_k\mathbf{p_k}$. Then Ψ is recalculated with the updated parameter vector and checked again to determine if the stopping criteria, which is set by the user to test how close the model fluence rate is to the data, is satisfied. If the criteria, or some maximum iteration number, is not met, then x is updated again, and the loop is continued.

$\Delta\mathbf{x}$ depends on the step size γ and the step direction $\mathbf{p}$. γ is determined by a line search along $\mathbf{p_k}$ that sufficiently minimizes Ψ:

$$\min_{\gamma} \mathbf{\Psi}(\mathbf{x}_k + \gamma\mathbf{p_k}). \tag{2.62}$$

The Taylor's expansion of our updated objective function $\mathbf{\Psi}(\mathbf{x}_k + \gamma\mathbf{p}_k)$ is:

$$\mathbf{\Psi}(\mathbf{x}_k + \gamma\mathbf{p}_k) = \mathbf{\Psi}(\mathbf{x})_k + \gamma\mathbf{p}_k^T\nabla\mathbf{\Psi}(\mathbf{x}_k) + \frac{1}{2}\gamma^2\mathbf{p}_k^T\nabla^2\mathbf{\Psi}(\mathbf{x})_k\mathbf{p}_k + \cdots \tag{2.63}$$

The search direction $\mathbf{p}_k$ can be derived using either the first order derivative (Conjugate Gradient) or the second order derivative (Gauss-Newton). We will briefly discuss these methods in the following sections.

2.2.2.3 Conjugate Gradient Method

The Conjugate-Gradient technique is a commonly implemented method in DOT reconstruction algorithms. For a detailed derivation of the Conjugate Gradient (CG) method, I refer the reader to [147, 149]. Very briefly, to use the CG method, $\nabla\mathbf{\Psi}$ from the 2nd term of Equation (2.63) is needed. It is

$$\nabla \boldsymbol{\Psi}(\mathbf{x}) = \mathbf{J}(\mathbf{x})^{\mathbf{T}}\mathbf{F}(\mathbf{x}) \ ; \tag{2.64}$$

$$f_i(\mathbf{x}) = \Phi_i^c(\mathbf{x}) - \Phi_i^m \ ; \tag{2.65}$$

$$\mathbf{F}(\mathbf{x}) = \Big[f_1(\mathbf{x}), f_2(\mathbf{x}), \cdots, f_M(\mathbf{x})\Big]^T \ . \tag{2.66}$$

where the Jacobian is

$$J = \begin{bmatrix} \frac{\partial f_1(\mathbf{x})}{\partial x_1} & \frac{\partial f_1(\mathbf{x})}{\partial x_2} & \cdots & \frac{\partial f_1(\mathbf{x})}{\partial x_N} \\ \frac{\partial f_2(\mathbf{x})}{\partial x_1} & \frac{\partial f_2(\mathbf{x})}{\partial x_2} & \cdots & \frac{\partial f_2(\mathbf{x})}{\partial x_N} \\ \vdots & \vdots & \ddots & \vdots \\ \frac{\partial f_M(\mathbf{x})}{\partial x_1} & \frac{\partial f_M(\mathbf{x})}{\partial x_2} & \cdots & \frac{\partial f_M(\mathbf{x})}{\partial x_N} \end{bmatrix} . \tag{2.67}$$

For real experimental data in Chapter 4, the Jacobians are arranged as shown in Fig. 2.2.2.3. The Jacobian is typically calculated for known μ_a and μ_s'. The image reconstruction software that we use (Toast++) readily provides the gradients for the standard DOT optical coefficients, i.e.,

$$f'^{(\mu_a)} = \frac{\partial \Phi}{\partial \mu_a}, \quad f'^{(\mu_s)} = \frac{\partial \Phi}{\partial \mu_s} \ . \tag{2.68}$$

For multi-spectral data, we want the Jacobian to be written in terms of the chromophore concentration and the scattering factor and power A, b. The required gradients with respect to these parameters can be obtained by applying the chain rule:

$$f'^{(c_i)} = \sum_{j=1}^{L} f'^{(\mu_a)}(\lambda_j)\frac{\partial \mu_a(\lambda_j)}{\partial c_i} = \sum_{j=1}^{L} f'^{(\mu_a)}(\lambda_j)\varepsilon_i(\lambda_j)\ ; \tag{2.69}$$

$$f'^{(A)} = \sum_{j=1}^{L} f'^{(\mu_s)}(\lambda_j)\frac{\partial \mu_s(\lambda_j)}{\partial A} = \sum_{j=1}^{L} f'^{(\mu_s)}(\lambda_j)\lambda_j^{-b}\ ; \tag{2.70}$$

$$f'^{(b)} = \sum_{j=1}^{L} f'^{(\mu_s)}(\lambda_j)\frac{\partial \mu_s(\lambda_j)}{\partial b} = \sum_{j=1}^{L} f'^{(\mu_s)}(\lambda_j)A\lambda_j^{-b}\ln\lambda_j\ . \tag{2.71}$$

Now we are able to use the Conjugate Gradient algorithm:

1. Initialize: $k = 0$

$$\mathbf{r}_0 = -\nabla\mathbf{\Psi}(\mathbf{x}_0)\ ; \tag{2.72}$$

$$\mathbf{p}_0 = \mathbf{r}_0\ . \tag{2.73}$$

2. Find step size (find γ):

$$\min_{\gamma}\mathbf{\Psi}(\mathbf{x}_k + \gamma_k\mathbf{p_k})\ . \tag{2.74}$$

3. Update parameters:

$$\mathbf{x}_{k+1} = \mathbf{x}_k + \gamma_k\mathbf{p}_k\ . \tag{2.75}$$

4. Check $\Big[\mathbf{\Psi}(\mathbf{x}_{k+1}) <$ criteria?$\Big]$: $\Big($ **Yes:** Stop **No:** Continue

5. Update direction vector:

$$\mathbf{r}_{k+1} = -\nabla\mathbf{\Psi}(\mathbf{r}_{k+1})\ ; \tag{2.76}$$

$$\beta_{k+1} = \frac{\mathbf{r}_{k+1}^T(\mathbf{r}_{k+1} - \mathbf{r}_k)}{\mathbf{r}_k^T\mathbf{r}_k}\ ; \tag{2.77}$$

$$\mathbf{p}_{k+1} = \mathbf{r}_{k+1} + \beta_{k+1}\mathbf{p}_k. \tag{2.78}$$

6. $k = k + 1$. Move to Step 2.

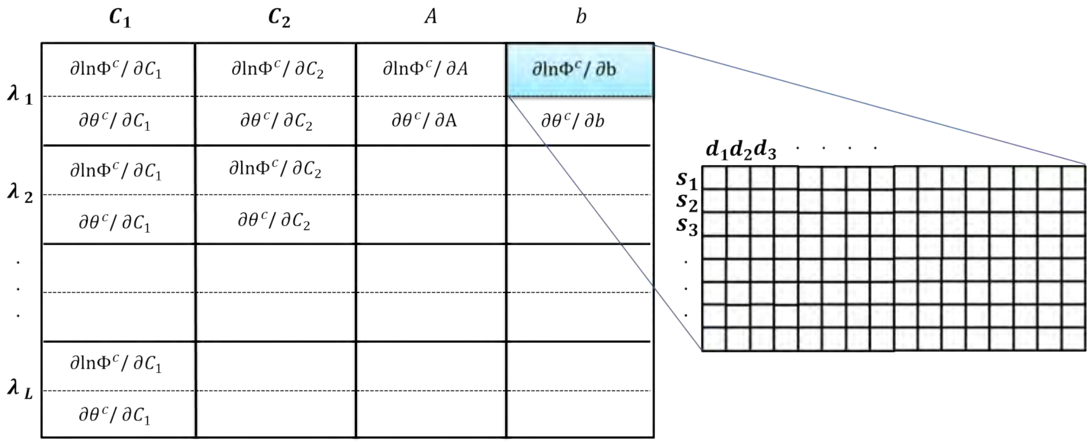

Figure 2.7: Illustration of the Jacobian matrix for datasets collected in Chapter 4. Row blocks are organized by wavelengths; they are further divided into amplitude and phase. Column blocks are organized by the chromophores (C), and A,b. The amplitude and phase data blocks (light blue) consist of data for every source-detector pair: the rows indexes the sources s and the columns indexes the detectors d for each source.

2.2.2.4 Gauss-Newton Method

The Gauss-Newton method is an iterative method that uses an approximation of second order derivatives in the cost function. Consider Equation (2.63) with $\gamma = 1$. Let us assume that $\mathbf{\Psi}(\mathbf{x}_k + \gamma \mathbf{p}_k)$ is twice differentiable. Beginning with Equation (2.63) and differentiating both sides with respect to $\mathbf{p}_k$ we have:

$$\nabla \mathbf{\Psi}(\mathbf{x}_k + \gamma \mathbf{p}_k) = \nabla \mathbf{\Psi}(\mathbf{x}_k) + \nabla^2 \mathbf{\Psi}(\mathbf{x})_k \mathbf{p}_k \; . \tag{2.79}$$

$\mathbf{\Psi}(\mathbf{x}_k + \gamma \mathbf{p}_k)$ is minimized when $\nabla \mathbf{\Psi}(\mathbf{x}_k + \gamma \mathbf{p}_k) = 0$. The above equation then becomes:

$$\nabla^2 \mathbf{\Psi}(\mathbf{x})_k \mathbf{p}_k^{GN} = -\nabla \mathbf{\Psi}(\mathbf{x}_k) \; , \tag{2.80}$$

where $\mathbf{p}_k^{GN}$ is a vector that points in the Newton direction. We know $\left[\nabla\mathbf{\Psi}(\mathbf{x}_k) = \mathbf{2J}(\mathbf{x}_k)^T\mathbf{F}(\mathbf{x}_k)\right]$ from Equation (2.64). $\nabla^2\mathbf{\Psi}(\mathbf{x})$ is

$$\nabla^2\mathbf{\Psi}(\mathbf{x}_k) = \sum_{m=1}^{M}\nabla^2(\mathbf{\Psi}(\mathbf{x}_k)^2) = \sum_{m=1}^{M}\mathbf{H}^{\mathbf{m}}(\mathbf{x}_k)\ , \tag{2.81}$$

where $\mathbf{H}^m(\mathbf{x}_k)$ is the Hessian. Written out explicitly:

$$\nabla^2\mathbf{\Psi}(\mathbf{x}_k) = 2\mathbf{J}(\mathbf{x}_k)^T\mathbf{J}(\mathbf{x}_k) + \sum_{m=1}^{M}\sum_{i=1}^{N}\sum_{j=1}^{N} f_i(\mathbf{x})\frac{\partial f_m(\mathbf{x})}{\partial x_i \partial x_j}\ . \tag{2.82}$$

The second term is much smaller than the first term, and in the Gauss-Newton method an approximation is made wherein the second term is ignored such that:

$$\nabla^2\mathbf{\Psi}(\mathbf{x}_k) = 2\mathbf{J}(\mathbf{x}_k)^T\mathbf{J}(\mathbf{x}_k)\ . \tag{2.83}$$

Thus the main equation in the Gauss-Newton method is:

$$2\mathbf{J}(\mathbf{x}_k)^T\mathbf{J}(\mathbf{x})_k\mathbf{p}_k^N = -\mathbf{2J}(\mathbf{x}_k)^T\mathbf{F}(\mathbf{x}_k)\ . \tag{2.84}$$

With this method to ascertain the Gauss-Newton direction $\mathbf{p}_k^N$, this relation can be used repeatedly in an iterative manner. A line search method can also be added into the algorithm where the minimum is searched for along $\mathbf{p}_k^N$. The Gauss-Newton algorithm is as follows:

1. Initialize: k = 0
2. Evaluate:
$$\nabla \boldsymbol{\Psi}(\mathbf{x}_k) = \mathbf{2J}(\mathbf{x}_k)^T \mathbf{F}(\mathbf{x}_k) \; ; \tag{2.85}$$
$$\nabla^2 \boldsymbol{\Psi}(\mathbf{x}_k) = 2\mathbf{J}(\mathbf{x}_k)^T \mathbf{J}(\mathbf{x})_k \; . \tag{2.86}$$
3. Solve for $\mathbf{p}_k^N$ in
$$2\mathbf{J}(\mathbf{x}_k)^T \mathbf{J}(\mathbf{x})_k \mathbf{p}_k^N = -\mathbf{2J}(\mathbf{x}_k)^T \mathbf{F}(\mathbf{x}_k) \tag{2.87}$$
$$\text{(using GMRES, CG, etc.)} \; .$$
4. Compute γ_k (line search) .
5. Update parameter:
$$\mathbf{x}_{k+1} = \mathbf{x}_k + \gamma_i \mathbf{p}_k \; . \tag{2.88}$$
6. Check $\Big[\boldsymbol{\Psi}(\mathbf{x}_k) < \text{criteria?}\Big]:\Bigg($ **Yes:** Stop **No:** Continue
7. Update $k = k + 1$, go to Step 2.

2.2.2.5 Levenberg-Marquardt Method

The Levenberg-Marquardt Method is another technique commonly used in DOT reconstruction packages (e.g., TOAST++, NIRFAST) that I will very briefly summarize. The Levenberg-Marquardt Method is a variation on the Gauss-Newton method wherein a term is added to the Hessian in Equation 2.84

$$2[\mathbf{J}(\mathbf{x}_k)^T \mathbf{J}(\mathbf{x})_k + \lambda I]\mathbf{p}_k = -\mathbf{2J}(\mathbf{x}_k)^T \mathbf{F}(\mathbf{x}_k) \; ; \tag{2.89}$$

$$\mathbf{p}_k = -2[\mathbf{J}(\mathbf{x}_k)^T \mathbf{J}(\mathbf{x})_k]^{-1} \mathbf{2J}(\mathbf{x}_k)^T \mathbf{F}(\mathbf{x}_k) \; . \tag{2.90}$$

λ is called the damping parameter. This additional term has two main effects. The first effect is to increase the the number on the diagonals and therefore suppress the 2nd derivatives. A large λ will result in the left hand side of the equation being more like the identity matrix, resulting in the steps becoming more like the steepest descent method. One common technique is to start with a large λ and then decrease its value at each iteration (i.e., by half every iteration); this procedure causes a gradual switch from the gradient descent method to Gauss-Newton over each step of the reconstruction. The second effect that this additional term introduces is to limit the step size. Since they are inversely related with the search direction vector $\mathbf{p}_k$ (Equation 2.90), higher damping terms have the effect of decreasing the step size. This decrease in step size prevents large changes in the iteration at early steps which is useful when there could be instabilities due to errors in the initial guess. Overall these two functions have an effect of stabilizing the reconstruction in the early iterations.

2.2.2.6 Regularization

The image reconstruction problems we discussed above are generally ill-posed and often underdetermined (i.e., the number of independent measurements are less than the number of unknowns). Among the characteristics of ill-posed problems is that small changes in detected signals can induce large changes in the reconstructed optical properties This situation implies that the reconstructions have non-uniqueness problems and will require additional constraints to help achieve convergence. In practice the solution space is constrained or *regularized* to utilize *apriori* information. Generally, any scientist working on ill-posed image reconstruction (or ill-posed inverse problems) will utilize some type of regularization technique to optimize their images. In the medical imaging field, regularization is common.

For our nonlinear methods, regularization is typically introduced as a term in the objective function as shown below:

$$\Psi = \frac{1}{2} \sum_{l=1}^{L} \sum_{s=1}^{S} \sum_{d=1}^{D_s} \Bigg(\left[\Phi^c(\mathbf{x}) - \Phi \right]^2 + \Lambda R(\mathbf{x}) \; . \tag{2.91}$$

Here Λ is the scaling factor, and $R(\mathbf{x})$ is called the regularization functional. As in Equation 2.61, L is the total number of wavelengths, S is the total number of sources, and D_s is the number of detectors for a particular source s. The additional term can be thought of as a penalty on the cost function based on the regularization functional. A few examples are: $R = ||\mathbf{x} - \mathbf{x_0}||_2^2$, $R = ||\nabla \mathbf{x}||_1$, and $R = -\nabla \cdot (\nabla \mathbf{x} / |\nabla \mathbf{x}|)$; in these cases, the reconstruction is effectively penalized for large optical property excursions within the image based on, respectively, its difference, its gradient, or a function of its change in gradient. The relative importance of these penalties is adjusted through the scaling factor Λ, which can be modified with each iteration as well. These kinds of regularization terms are useful when spatial information about the optical properties of the medium are known, or when some information about the optical property variations are expected. The more information one has in advance, the more that can be included in the cost function.

Throughout this thesis, I have explored the utility of various regularization schemes, and I have tried to identify the best ones for our problem. These tasks are non-trivial and have only just begun. In our reconstructions in Chapter 4, we found that the Total Variation (TV) method, which is an edge-preserving regularization, can work well. TV was applied to preserve contrast and to preserve transverse size of targets in our DOT reconstructions, but it also had the cost of increasing certain classes of artifacts. The particular form we used is $\Lambda\sqrt{|\nabla \mathbf{x}|^2 + \beta^2}$, which is actually an approximation of the TV method. Here $\beta > 0$ is a small parameter added to deal with the non-differentiability of the absolute value $|\nabla \mathbf{x}|$ when $\nabla \mathbf{x} = 0$. It is worth noting that it is also possible to employ different regularization multiplicative scaling terms for different optical parameters. For example, in our reconstructions in Chapter 4, we found that using a separate regularization factor for absorption and for scattering improved the spatial fidelity of the target reconstructions (see Section 4.8.1 in Chapter 4).

Chapter 3

Imaging Breast Cancer: Chest Wall Effects

3.1 Introduction

Although various forms of diffuse optical tomography (DOT) have been employed to derive spatial maps of physiological features in the human breast with some success, the fidelity of these images is compromised by boundary effects such as those that arise from data obtained near the subject's chest wall.

The breast is sometimes approximated as a slab, which allows the formulation of imaging problem with analytical Green's functions. The chest wall falls within the vicinity of the breast through which light can travel. Furthermore, from a general diffuse optics viewpoint, the very existence of the chest wall breaks the natural symmetry of the slab geometry, a symmetry which is often utilized when formulating Green's functions for the imaging problem. The chest wall introduces perturbations into the inverse problem that become more important as the source and detector locations move away from the nipple region and closer to the chest.

The DOT community has not dealt systematically with the influence of the chest wall. Dealing with these chest wall issues is the primary purpose of the research described in this Chapter, which is based on and expands upon my publication in the Journal of Biomedical Optics [137]. The remainder of this sub-section provides a brief perspective about the whole of my work on this problem. Following the present section, it is organized as follows: in Section 3.2 the experimental set-up is described in detail; Section 3.3 explains our approaches to data restriction; Section 3.4 presents the results, and Section 3.5 contains a brief discussion about the findings and implications of the work.

Specifically, as part of our effort to translate DOT into the clinic, I set about to explore the effect of the chest wall in a systematic study at the optical bench. I assessed image quality of two types of DOT reconstructions: fast data-intensive analytic inversions and algebraic linear DOT. The investigation employed tissue phantoms with sub-centimeter targets in the presence of large absorbing regions that mimic the chest wall. My experiments show that this chest wall phantom can introduce image artifacts, and that these artifacts are especially severe for features near the boundary region. The responses are fully characterized, and I show how these artifacts can be mitigated by exclusion of data near the chest wall. As part of this effort, in addition to exploring the utility of well-understood analytic inversions, I introduce and demonstrate a linear algebraic reconstruction method that is well suited for very large data sets (i.e., large data sets characteristic of CCD-based imagers); I study the performance of this algorithm for the first time as a function of distance from the phantom chest wall.

Here we employ linear image reconstruction methods and take measurements using continuous-wave (CW) illumination. In principle, one could also resort to time- [150–155] or frequency-domain [82, 156–158] measurements and nonlinear reconstruction methods [35, 134] to obtain a reconstruction of the target and the chest wall phantom simultaneously; however, these approaches require more expensive and complex instrumentation, as well as more time-consuming computational schemes.

The algorithms and experimental apparatus employed for these studies were carefully chosen to provide best case scenarios for breast imaging. It has been demonstrated that image quality in DOT [52, 136, 159], and in other imaging modalities such as inverse diffraction [160], can be significantly improved by utilization of large data sets for the reconstruction. Furthermore, it has been shown that the plane-parallel transmission geometry is particularly well suited for utilization of larger data sets. The plane-parallel transmission geometry benefits from the possibility of non-contact source scanning [136, 161–164] and detection where a collimated laser beam can be scanned on one side of the sample for illumination, and is paired with a CCD camera for parallel detection.

A characteristic feature of such non-contact scanning approaches is the availability of very large data sets with up to $\sim 10^9$ independent measurements, e.g., with $\sim 10^3$ source positions and $\sim 10^6$ CCD pixels per source. Unfortunately, utilization of data sets consisting of more than $\sim 10^5$ independent measurements presents a serious computational challenge for traditional inversion methods, primarily due to data storage requirements. For this reason, theorists in the DOT community are motivated to develop new (and fast) algorithms capable of reconstructing very large data sets, albeit in simple imaging geometries (including the slab geometry) [130, 131, 133–135]. Numerical simulations [131] have explored some aspects of these methodologies, and they also indicate that large image windows (i.e., wide-field illumination and detection) are required to achieve optimal resolution. For example, the simulations suggest that the dimensions on both sides of the slab, wherein sources are scanned and CCD-detectors collect data, ideally, should be larger by a factor of approximately 3 in both transverse directions compared to the slab thickness. In practice, experimental studies have shown that a somewhat smaller ratio can be used and the ultimate limits will be due to the presence of noise and other imperfections of the imaging system [52, 136]. My experiments employ this type of ideal experimental geometry and data generation/collection scheme with the additional complication of the chest-wall phantom. Thus my research helps to set best-case bounds for DOT breast imaging.

The tissue phantoms used for the experiment are similar to many that have been utilized with success in the DOT community for preclinical, *in vitro* investigations that ascertain the strengths and limitations of various image reconstruction schemes [44, 165, 166]. One advantage of the present tissue phantom experiment is that it is possible to compare reconstructions obtained under similar conditions but with different imaging windows and spatial sampling, some of which would be difficult to realize *in vivo*. Thus, based on this single set of experimental results, I am able to discuss and compare two (or more) approaches for image reconstruction of large data sets under conditions of large/small imaging windows. In this way, one can more fully explore methods to ameliorate chest wall effects.

3.2 Experiment and Setup

In this sub-section, I will describe details of the experimental set-up including illumination, detection, and mechanical features of the tissue phantom. The experimental apparatus is shown in Fig. 3.1.

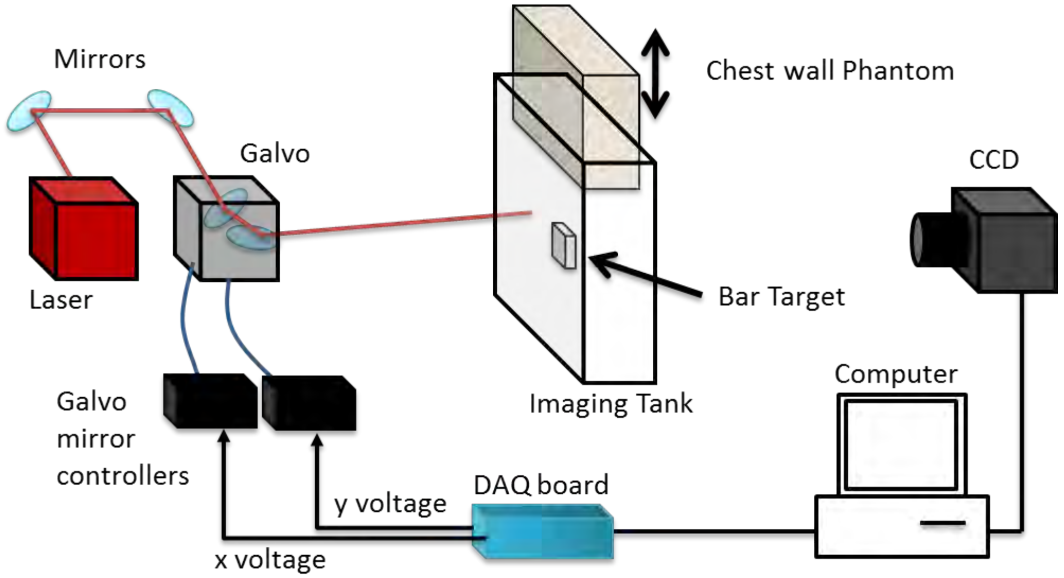

Figure 3.1: Schematic of the experimental setup at the optical bench. A CW $785\,\mathrm{nm}$ laser source is raster scanned on one side of the imaging tank. The transmitted light on the detection plane is collected in parallel by a CCD and then binned (flexibly) for each source position.

3.2.1 Light source

Source illumination light is derived from a collimated 785nm 90mW diode laser (Thorlabs, L785P090). The laser is coupled to a 2D galvonometer scanner (Thorlabs, GV012). The diode laser output is temperature sensitive, and therefore it is temperature controlled using a diode laser mount (Thorlabs, TCLDM9) and a temperature controller (ILX lightwave, LDT-5525) with custom cable for different pin configurations (required when using different brands for the mount and controller). The laser is current driven at $160\,\mathrm{mA}$ using the diode laser controller (Thorlabs, LDC500). The wavelength of the laser is $785\,\mathrm{nm}$. The output of the beam is collimated (Thorlabs, C140TMD-B) on the laser mount and is then focused, over a $2\,\mathrm{m}$ length, to a $0.5\,\mathrm{mm}$ spot size onto the source plane of the imaging tank.

The beam is raster scanned across this source plane of the imaging tank. Specifically, the collimated laser light is aligned with a pair of mirrors into the galvo scanner which raster scans a 35×35 square grid with a $4\,\mathrm{mm}$ spacing covering an area of $13.6 \times 13.6\,\mathrm{cm}^2$ on the inner side of the source window of the imaging tank. The galvo is controlled with a pair of drivers (one for each mirror). Voltages can be applied to the driver card to change the angle of the mirrors. Each mirror has a maximum angular displacement of $\pm 20^o$, and $1\mathrm{V}$ moves the mirror 1^o. Resistor pots on the driver were utilized to scale the voltage down (to $0.5\mathrm{V}/1^{\mathrm{o}}$) and to add an offset (as needed). A DAQ board (National Instruments, USB-6251) was used to output two distinct voltages (through its analog output channels a0 and a1) to the galvo scanner in series for each source position.

3.2.2 Imaging Tank

The imaging tank shown in Fig. 3.3 is designed specifically for the chest wall experiment. The tank is composed of aluminum walls on three surfaces (i.e., the bottom plate and two side plates) with acrylic windows in the input and output planes, and an opening at the top. The latter opening permits loading of Intralipid, targets and the chest wall phantom. In addition, a spigot is built into the side for easy draining and cleaning of the tank. The inner dimensions of the tank are $44 \times 44 \times 6\,\mathrm{cm}^3$. The $6\,\mathrm{cm}$ thickness of the tank was chosen to be close to the average compression used in our DOT clinical studies [44, 53]. The unit has a removable black Delrin

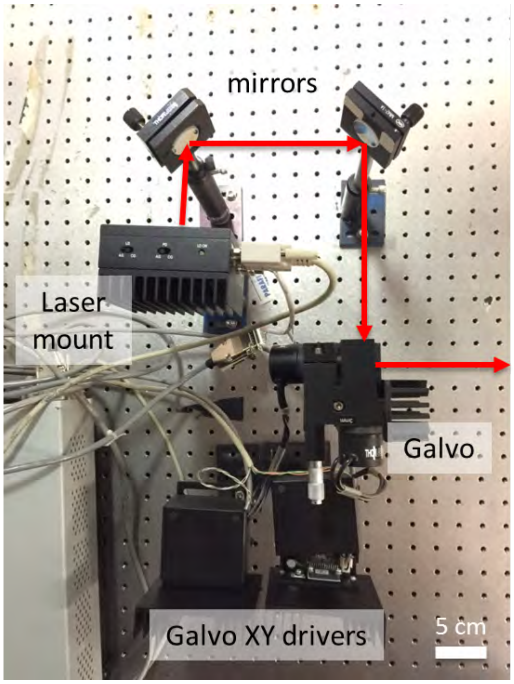

Figure 3.2: Photograph of the laser and source position control setup. The diode laser is mounted on a TEC cooled mount with collimating lens that outputs the beam to a pair of mirrors which redirects the beam onto the galvo mirrors for scanning.

target holder which lines the walls of the tank, and it has evenly spaced holes that can be threaded with filamentous fishing lines to suspend various phantoms within the tank. These fishing lines hold bar targets (described in Section 3.2.4). The windows are designed to be swappable and are lined with o-rings for water tight sealing. In this experiment a pair of $1/2 - \mathrm{inch}$ acrylic windows were used. The top of the tank has optical posts that hold an aluminum plate which, in turn, holds a pair of threaded rods from which the chest wall phantom is suspended downwards.

3.2.3 CCD Detection

For each illuminated source position, transmission data is collected on the opposite side of the tank over a $21.2 \times 21.2\,\mathrm{cm}^2$ field-of-view (FOV) area. These data are collected with a CCD

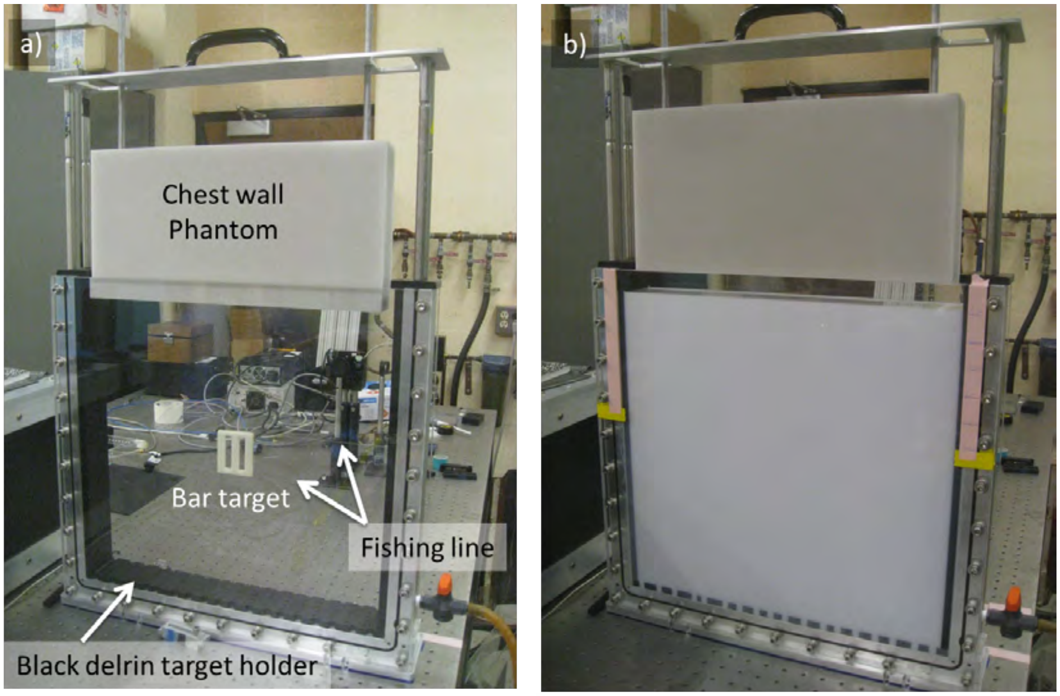

Figure 3.3: Photograph of the imaging tank. a) The bar target is suspended below the chest wall phantom with fishing lines. b) The tank filled with Intralipid solution.

camera (Andor, DV887ECS-UV, lens $25\,\mathrm{mm}$ $\mathrm{F}/0.95$). The FOV is effectively mapped to a grid of 512×512 CCD pixels. This mapping yields a corresponding detected rectangular grid on the output surface of the tank with spacing $p = 0.416\,\mathrm{mm}$. The CCD typically employed an exposure time of $500\,\mathrm{ms}$ at 16-bits (for a total of $2^{16} \sim 64\mathrm{K}$ counts) with 1×1 binning. The total measurement time per scan was $\sim 11\,\mathrm{min}$.

3.2.4 Phantoms: Bar Target and Chest Wall

The bar target is made of silicon rubber (RTV-12, General Electric), titanium oxide (T-8141, Sigma-Aldrich) and carbon black (Raven 5000 Ultra Powder II). It has absorption coefficient $\mu_\mathrm{a} = 0.2\,\mathrm{cm}^{-1}$ and reduced scattering coefficient $\mu_\mathrm{s}' = 7.5\,\mathrm{cm}^{-1}$. The tank is filled with an indian ink and intralipid solution ($\mu_\mathrm{a} = 0.05\,\mathrm{cm}^{-1}$ and $\mu_\mathrm{s}' = 7.5\,\mathrm{cm}^{-1}$); these background

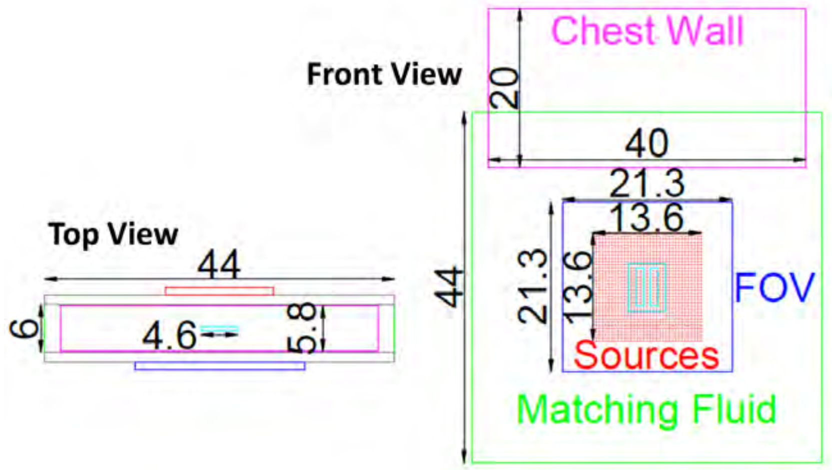

Figure 3.4: Schematic of the imaging tank with dimensions given in units of cm. The red sources make up a $13.6 \times 13.6\,\mathrm{cm}$ grid within the blue $21.3 \times 21.3\,\mathrm{cm}$ field of view of the CCD. The green dimensions are the tank size and the purple dimensions are those of the chest wall phantom.

optical properties are similar to those used in previous *in vitro* and clinical research. The contrast between the target and the surrounding fluid is purely absorptive with ratio of about 4. The bar target is suspended in the mid-plane of the tank ($3\,\mathrm{cm}$ from either surface) using the fishing line.

A chest wall phantom (Biomimic, INO) with $\mu_\mathrm{a} = 0.1\,\mathrm{cm}^{-1}$ and $\mu_\mathrm{s}' = 5.0\,\mathrm{cm}^{-1}$ and dimensions $40 \times 20 \times 5.8\,\mathrm{cm}^3$) is suspended at various distances, d, from the top edge of the bar target ($d = 2,\ 5,\ 8,\ 11,\ 14,\ 17\,\mathrm{cm}$) as shown in Fig. 3.6 (a). The optical properties of the chest wall phantom were chosen to mimic muscle tissue [167–169]. Thus both absorptive and scattering contrast exist between the chest wall phantom and the background fluid. The bar target and the chest wall phantom are shown in Fig. 3.5. Note that the chest wall phantom almost entirely fills the imaging tank; the clearance between the chest wall phantom and the inner surfaces of the tank is $1\,\mathrm{mm}$ on both sides.

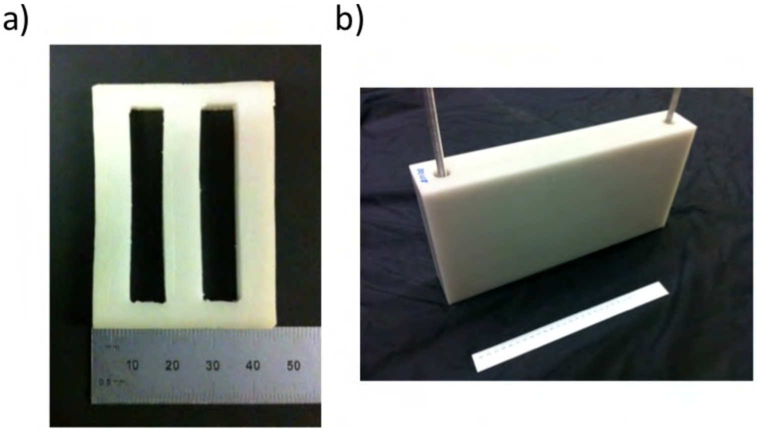

Figure 3.5: Phantoms used in the experiment. a) $6\,\mathrm{mm}$ thick bar target with $\mu_\mathrm{a} = 0.2\,\mathrm{cm}^{-1}$ and $\mu_\mathrm{s}' = 7.5\,\mathrm{cm}^{-1}$ has slots $48\,\mathrm{mm}$ tall and $9\,\mathrm{mm}$ wide. The outer dimensions are $60 \times 50\,\mathrm{mm}^2$. b) The chest wall phantom with $\mu_\mathrm{a} = 0.1\,\mathrm{cm}^{-1}$ and $\mu_\mathrm{s}' = 5.0\,\mathrm{cm}^{-1}$.

3.3 Methods

The experiments are straightforward. I first fill the tissue phantom tank with the background Intralipid suspension, and I collect baseline image data by cycling through each of the source positions and deriving a CCD-image output for each source position. Then I introduce the bar target into the suspension, and I insert the chest wall phantom into the suspension above the bar target (from the top). I then carry out another imaging measurement, i.e., obtaining CCD images while cycling through the source positions, with the bar target and chest wall phantom in the suspension and separated by a fixed distance. Lastly, I vary the distance between the bar target and the chest wall phantom and repeat the imaging procedure; I do this for multiple target-wall separation distances.

The data from the reference measurement and with the phantoms present are denoted by $I(\mathbf{r}_d, \mathbf{r}_s)$ and $I(\mathbf{r}_d, \mathbf{r}_s)$ (Eqns. (2.28) amd (2.29) from Chapter 2) where $\mathbf{r}_d$ $\mathbf{r}_s$ which are the two dimensional vectors specifying the lateral positions of the detector and source on the respective surfaces of the tank. Image reconstruction is carried out using the methods described in Chapter 2 (see Section 2.2.1.2 and 2.2.1.4). In this way, full 3D DOT reconstructions of the breast phantom and bar target are obtained as a function of the distance between the chest wall phantom and the bar target. This methodology permits characterization of the utility of the various methods in the presence of the chest wall, and it also permits exploration of selective data rejection schemes to ameliorate image artifacts. Below, I will describe this data rejection process in more detail.

In practice, a typical DOT measurement necessarily involves some rejection of data, i.e., rejection of data from source-detector pairs that are deemed unreliable or too noisy [28, 89, 170, 171]. This data rejection could be a result of signals that are too small, uncontrolled fluctuations of the apparatus/subject, etc. In the usual approach, data are rejected based on *a priori* knowledge or a statistical model without specific regard for the location of the rejected source-detector pairs. In the present case, data restriction is used with a somewhat different goal to minimize systematic error effects due to the chest wall. Here particular data are rejected based solely on location. The purpose is not to suppress noise in the strictest sense, but rather to investigate the effects of imaging window restrictions and the effects of the proximity of the chest wall phantom and bar target on the quality of the image reconstructions. Importantly, the positions and distances of sources and detectors in close proximity to the chest wall are explored to determine which of them can be used, i.e., which source-detector pairs lead to reconstructions wherein the target is not significantly distorted or contaminated by chest wall systematics.

The distance between the top of the bar target and the bottom of the chest wall phantom as indicated in the figure is denoted d. Data is collected for $d = 2$, 5, 8, 11, 14, and $17\,\mathrm{cm}$. The various data sets are graphically illustrated in Fig. 3.6. In Fig. 3.6(b), red lines show the

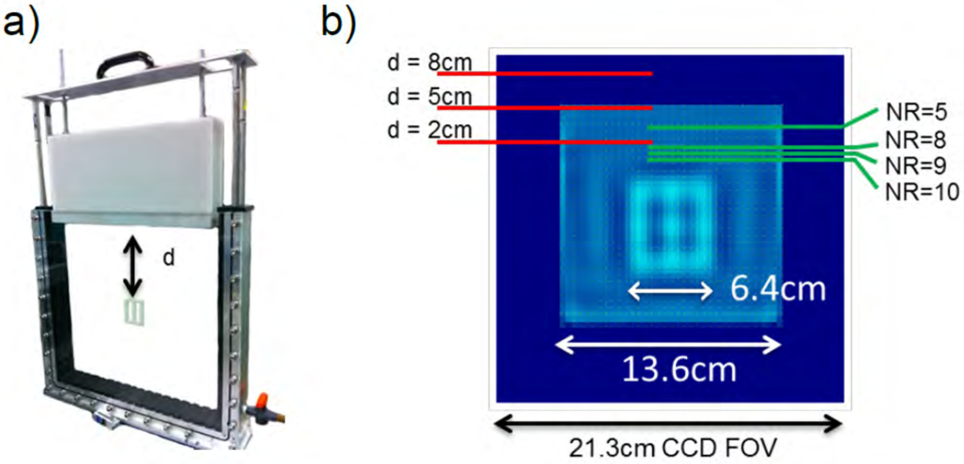

Figure 3.6: Models for data restriction. (a) Photograph of the drained imaging tank illustrating the position the bar target with respect to the chest wall phantom. (b) Schematic of the imaging tank. (c) Illustration of the various data sets used for the reconstructions. The dark blue square is the CCD FOV; the inner light blue square indicates the reconstruction region. White dots in a square grid indicate the source positions. To illustrate the target shape and position, a slice of a sample reconstruction is superimposed with the drawing. Red lines indicate the three lowest positions of the chest wall phantom (other positions are outside of the CCD FOV), and the green lines illustrate the restricted data sets wherein all the sources and detectors situated above a given green line have been discarded.

positions of the lower edge of the chest wall phantom corresponding to different values of d which fall within the CCD field-of-view (e.g, $d = 8$, 5, and $3\,\mathrm{cm}$). In this figure the source positions are shown as a small square grid of dots. Note, the image is to scale, and a slice of the sample reconstruction is superimposed with the drawing in order to indicate the target shape and position. The large dark blue square corresponds to the field-of-view (FOV) of the CCD camera.

The linear reconstruction techniques (analytical and algebraic) discussed in Section 2.2.1 are applied to the experimental data obtained using the apparatus described above. These techniques are able to handle large data sets and permit comparison to previous work [52]. The maximum number of independent source-detector pairs is $(512 \times 35)^2 \simeq 3.2 \times 10^8$. However, only a fraction of this data (albeit still a large data set) was used in the reconstructions. Some data was eliminated by "windowing" (i.e., in the algebraic image reconstruction); other data were eliminated by a relatively sparse sampling of the detectors (e.g, in the algebraic reconstructions, every second detector was used), and still other data were eliminated by numerical data restrictions (described below). Thus the maximum data set utilized for reconstruction (in this case, for the algebraic reconstruction) was still very large, i.e., it consisted of $\simeq 2 \times 10^7$ measurements.

In obtaining algebraic reconstructions, the reconstructed volume was divided into cubic voxels. The voxel size h was taken to be equal to 8 CCD pixels p. Thus, $h = 8 \times 0.416\,\mathrm{mm} \simeq 3.3\,\mathrm{mm}$. The grid consisted of 41×41 voxels in the lateral direction and 17 voxels in the depth direction. Therefore, the discretized volume was a parallelepiped with the dimensions $13.6 \times 13.6 \times 4.3\,\mathrm{cm}^3$ consisting of $N = 21853$ voxels. This parallelepiped was positioned from each surface of the slab. The target was situated approximately in the middle of the discretized volume. The computation of A^*A (see Section. 2.2.1.4is greatly accelerated by sampling the detectors for the purpose of computing the product A^*A, but not for computing the projection $A^*\phi$. In this way, the number of data points and the voxels used is not reduced but the computation time is shortened dramatically with no or minimal effects on the image quality. Indeed, we have verified that A^*A can be computed by using the method in Ref. [172] in about 2 hrs with very minimal degradation of image quality.

An additional feature of the algebraic method is that it does not require that the set of detectors used be independent of the position of the source. We have taken advantage of this feature and have excluded the data points that are very far off-axis. Specifically, for each source, we have used only such detectors that are situated no further from the axis of the source than a given radius R. We have used $R = 6.25\,\mathrm{cm}$, so that R is slightly larger than the width of the slab ($6\,\mathrm{cm}$). The justification for discarding the strongly off-axis data points is that these measurements contain predominantly noise.

The critical sources and detectors for the chest wall problem are those whose location is physically near the chest wall. An important question concerns how close to the chest wall one can collect data and maintain good image fidelity. Thus, for the present study, numerical data restriction involved removing all sources and detectors above one of the green lines shown in Fig. 3.6(c). In the case of algebraic reconstruction, sources **and** detectors above these lines were simply not used; thus no additional approximation was made. In the case of the analytical reconstruction (i.e., using analytic inversion formulas), data points cannot be excluded even for points above the green line. Rather it was assumed that the corresponding data points for these source-detector pairs (b_m) are zero ($I = I_0$), i.e., no change in intensity from the reference measurement (see Section. 2.2.1.1 in Chapter 2). In the upcoming discussion, NR denotes Numerical Data Restriction and is defined as the number of the source row (counting from top to bottom) above which no sources and/or detectors are included in the reconstruction. For example, $NR = 5$ excludes the four top-most lines of sources and all detectors that lie above the fifth line of sources. In the test reconstructions, $NR = 5, 8, 9, 10$ were used; for each value of NR, an image reconstruction was performed with all available values of d. Table 1 summarizes the subsets of data used for each value of NR.

Table 3.1: Data Restriction Sizes.

Numerical Data Restriction (NR)	Number of sources	Number of distinct source-detector pairs
No restriction	$35 \times 35 = 1,225$	$20,591,492$
5	$35 \times 31 = 1,085$	$16,479,152$
8	$35 \times 28 = 980$	$14,661,145$
9	$35 \times 27 = 945$	$14,074,728$
10	$35 \times 26 = 910$	$13,457,507$

3.4 Results

In this section we report on the application of analytical and algebraic reconstruction methods (Section 2.2.1.2 and 2.2.1.4) to the data sets collected as described above. The reconstruction results are displayed. In particular, I will show various reconstructions of the bar target with the chest wall at different distances d.

The reconstructed image contrast in all figures of this section is $x(\mathbf{r}) = \alpha(\mathbf{r})/\alpha_0 + 1$ where $\alpha = c\delta\mu_a$. Note we have redefined α (different from the more general form in Section 2.2.1.1, Chapter 2) for this experiment where only the absorption was reconstructed and scattering was assumed to be constant. This function is non-negative since the medium does not amplify light. However, the image reconstructions will employ various approximations. Sometimes a particular approximation can produce an unphysical negative value of absorption in the reconstruction; these volume elements are shown in the figures by the color black (note, the same color scale is used for all images). In practice, the occurrence of negative absorption can be avoided by using a positivity constraint in the algebraic reconstruction method. The positivity constraint can be directly incorporated into the conjugate-gradient descent algorithm, which was used to invert the matrix A^*A. However, in practice the areas of negative absorption appear mostly for the analytic image reconstruction method, and it is not possible to incorporate the positivity constraint into the analytic inversions. By contrast, the algebraic reconstructions have produced either no areas of negative absorption, or artifacts so severe (e.g., when $d = 2\,\mathrm{cm}$ and no numerical data restriction is used) that the positivity constraint was unnecessary. Since no situation occurred wherein the positivity constraint was simultaneously numerically sensible and useful, it was not employed for the images shown in this chapter.

3.4.1 Analytical Reconstruction Results

Reconstructions of the central slice of the medium ($3\,\mathrm{cm}$ from either of the slab surfaces) obtained with varying values of d and various numerical data restriction (NR) are shown in Fig. 3.7. It is apparent that the analytical inversion with no data restriction (the topmost row of images) produces severe image artifacts when chest wall is at distances of $d = 2\,\mathrm{cm}$ and even $d = 5\,\mathrm{cm}$ away from the target. To remove artifacts associated with the chest wall completely, $NR = 10$ is required. The data restriction with $NR = 5$ results in a reasonable, yet suboptimal, image quality when $d = 5\,\mathrm{cm}$, but not when $d = 2\,\mathrm{cm}$.

Interestingly, when the data restriction $NR = 8, 9, 10$ is used in conjunction with the analytical reconstruction, it yields an additional image artifact, which is unrelated to the chest wall phantom. To see that this is true, consider the images for $d = 17\,\mathrm{cm}$, which are not affected at all by the chest wall phantom, yet exhibit the additional artifact just mentioned. This artifact is evident as a black area wherein the reconstructed absorption coefficient is negative; therefore, it is outside of the physically-allowable range. Thus, it is reasonable to conclude that reconstructing the target via the analytical reconstruction method is feasible, especially with the use of the appropriate data restriction, but additional image artifacts can arise where the absorption is underestimated.

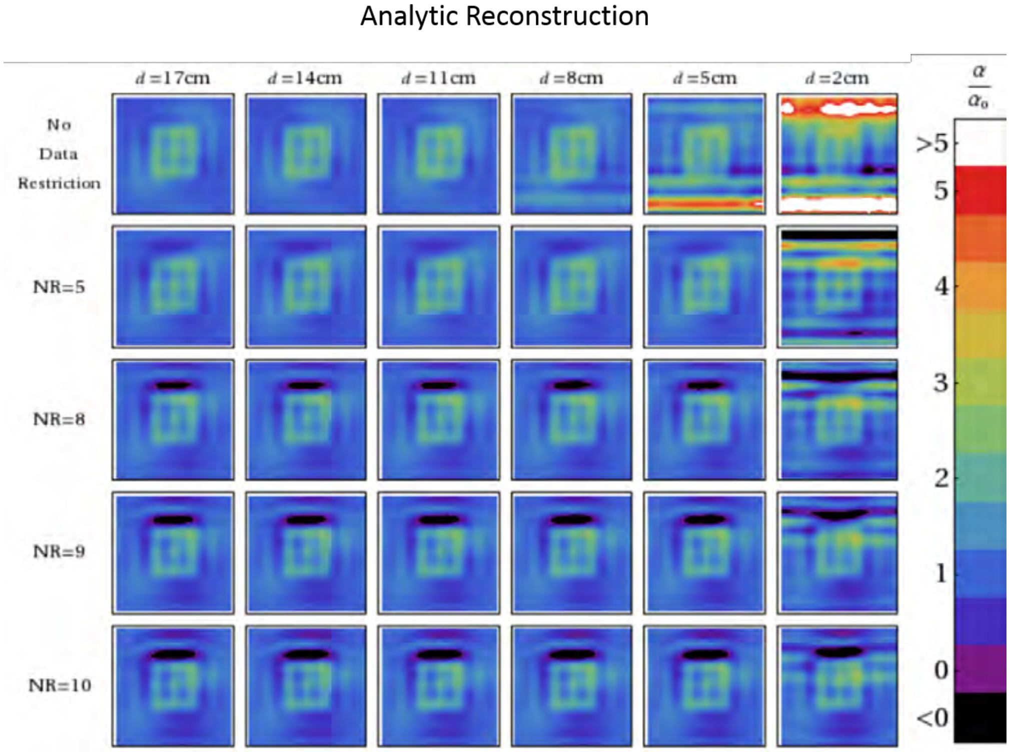

Figure 3.7: Images of the central slice obtained by analytical reconstruction method. Different columns show data obtained with the chest wall phantoms at different distances d from the bar target. Different rows of images correspond to different data restrictions NR, as indicated.

In fact, the appearance of this artifact can be understood. As mentioned above, the data restriction used with the analytical reconstruction amounts to assuming that the truncated data points are zero. In other words, if it is assumed (even in the presence of the target) that the truncated source-detector pairs would have measured the same intensity as in the homogeneous slab, then $I(\mathbf{r}_d, \mathbf{r}_s) = I_0(\mathbf{r}_d, \mathbf{r}_s)$ for the truncated source-detector pairs (see Section 2.2.1.1, Chapter 2). The reconstruction algorithm seeks a contrast function $\delta\alpha(\mathbf{r})$, which is compatible with this assumption. For a purely absorbing target, however, the actual intensity $I(\mathbf{r}_d, \mathbf{r}_s)$ is smaller than $I_0(\mathbf{r}_d, \mathbf{r}_s)$ when at least one of the points $\mathbf{r}_d, \mathbf{r}_s$ is located not too far from the target (in the lateral direction) due to increased optical absorption. Whenever such data points are discarded,

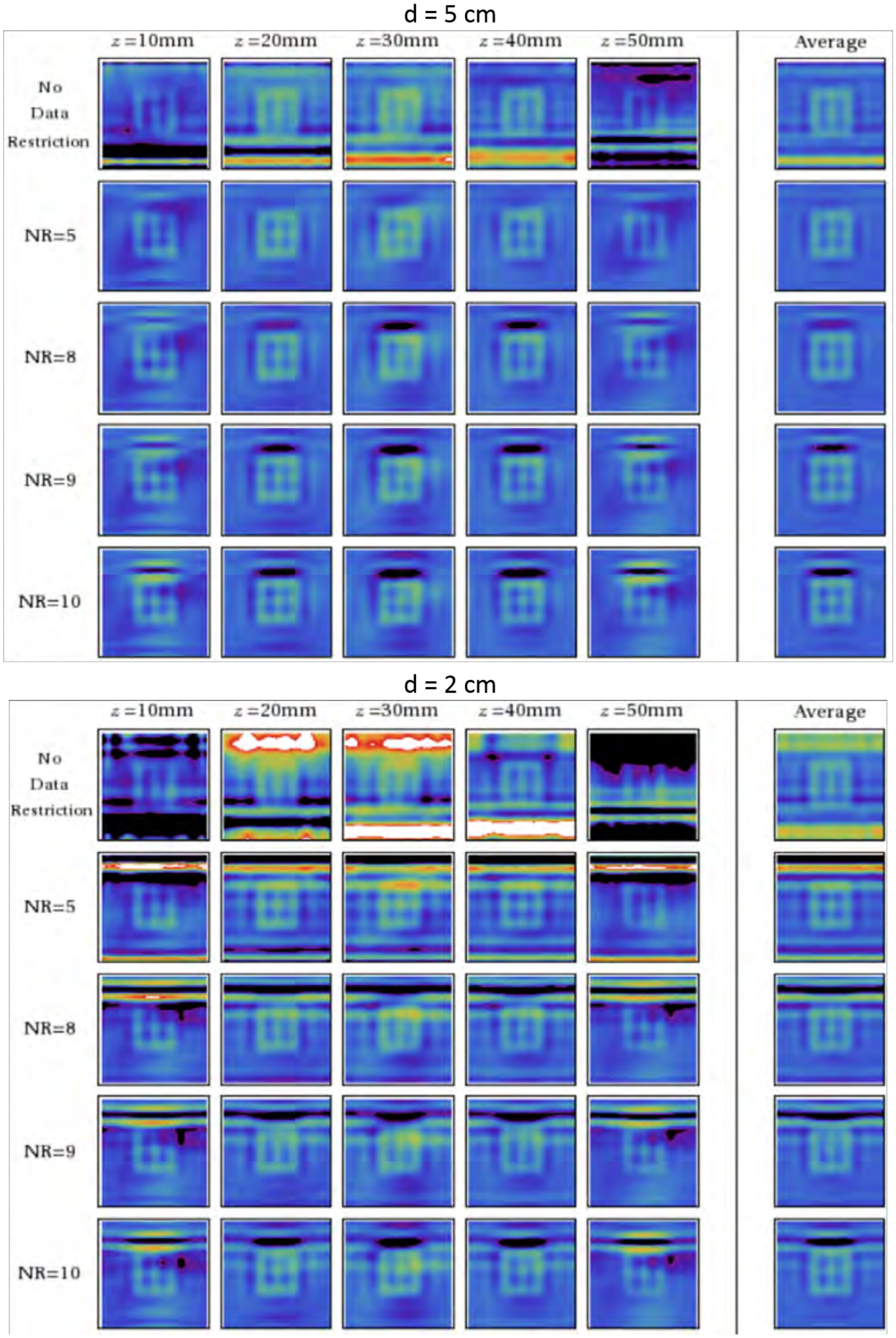

Figure 3.8: Slices through the medium drawn at different depths (from plane of sources). The analytical inversion reconstruction method used for $d = 5\,\mathrm{cm}$ and $d = 2\,\mathrm{cm}$.

an artifact with negative $\delta\alpha$ is produced by the reconstruction algorithm to compensate for the absorption in the target. It can be seen that this artifact is located between the target and the region of source-detector pairs, which have been discarded. Of course, this analysis applies to the case when the position and optical contrast of the target is known. In general, it may be difficult to predict the position of this artifact or to distinguish it from a true occurrence of negative $\delta\alpha$. There may also be a spatial overlap of the artifact and a true inhomogeneity.

3.4.2 Algebraic Reconstruction Results

In the algebraic reconstructions in Fig. 3.9 with the unrestricted data set, the image quality is still poor when the chest wall is to close. However, when the data restriction is gradually introduced these artifacts disappear. In the case $NR = 10$ and $d = 2\,\mathrm{cm}$ (the image in the bottom right corner), the target is clearly visible, and the image quality is about the same as with the use of the unrestricted data set and $d = 17\,\mathrm{cm}$. Thus, introduction of data restriction does not result in substantively additional image artifacts or image quality degradation when the algebraic method is used.

3.4.3 Comparison of Reconstruction methods and Projection Images

Figs. 3.8 and 3.10 show slices drawn through the medium at different depths. Fig. 3.8 displays the results of the analytical image reconstruction for $d = 5\,\mathrm{cm}$ and $d = 2\,\mathrm{cm}$ and Fig. 3.10 displays analogous data obtained by the algebraic reconstruction. In addition, in the right-most column of images, a different kind of image is shown; these images are reconstructions derived by averaging the full 3D tomogram over the depth of the sample (that is, averaging over the different slices). Note that, in all cases 13 slices in the tomogram are separated by the distance

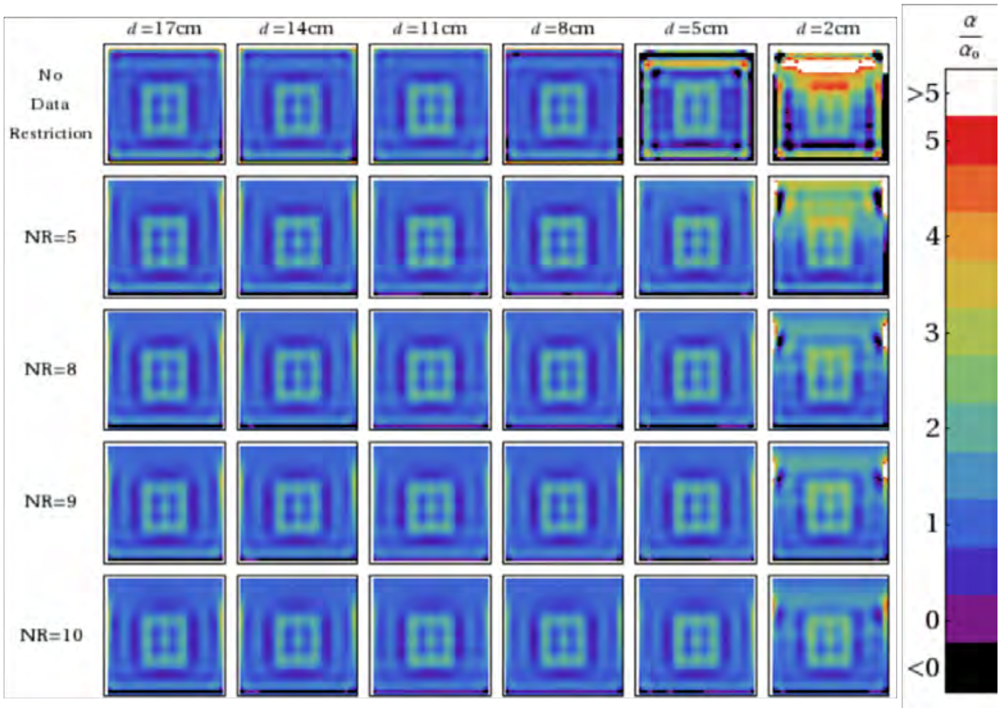
Algebraic Reconstruction

Figure 3.9: Images of the central slice obtained by algebraic reconstruction method. Different columns show data obtained with the chest wall phantoms at different distances d from the bar target. Different rows of images correspond to different data restrictions NR, as indicated.

of $\approx 3.328\mathrm{mm}$, with the central slice located exactly in the mid-plane of the slab. The "average" reconstruction (in the right-most column of the images) was obtained by computing the arithmetic average of all 13 slices.

These averaged ("projection") images correspond to the usual radiological projections obtained with a parallel beam of X-rays. Interestingly, the qualitative conclusions that can be drawn from Figs. 3.8 and 3.10 are largely the same as given above for the full tomograms. The analytical reconstruction produces reasonable image quality for the smallest chest wall-target separation $d = 2\,\mathrm{cm}$ and $NR = 10$, but at the cost of an additional image artifact. The algebraic reconstruction is free from this artifact, but it underestimates the image contrast relative to the

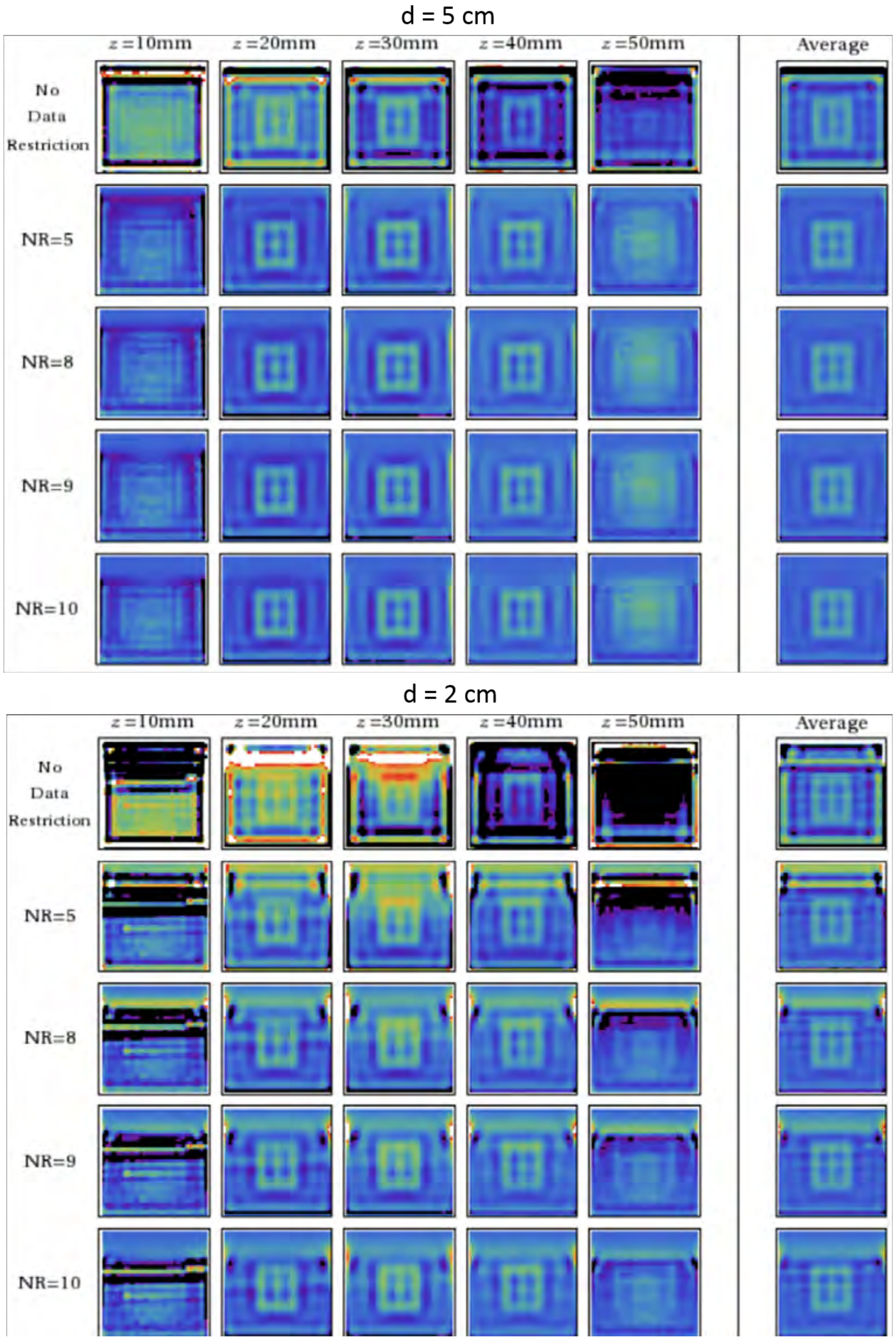

Figure 3.10: Same as in Fig. 3.8, but I this case the images are obtained by algebraic reconstruction

analytic method (see below). The depth resolution is slightly better in algebraic reconstructions but, overall (i.e., in both methods), depth resolution is worse than lateral resolution. This effect is typical for DOT images.

Another interesting feature can be discerned from both types of image reconstructions. Generally, the projection images discussed above are more stable and exhibit reasonable quality even when the individual slices contain substantial artifacts. For example, consider the $d = 2\,\mathrm{cm}$ algebraic reconstructions without data restriction (Fig. 3.10). Even though all slices drawn through the medium are corrupted by the artifacts associated with proximity of the chest wall phantom, the projection image shows the target clearly. Moreover, the edge of the chest wall phantom is also clearly visible at the correct location. I was surprised, and indeed our group was surprised by this result. It can be useful in situations when the depth resolution is not of essence. However, it should be emphasized that obtaining the projections still requires knowledge of the three-dimensional distribution of the absorption coefficient; the projections cannot be computed or measured directly without such knowledge.

Finally, note that in both types of image reconstructions, an underestimation of the contrast for the target phantom is observed compared to the expected value. This underestimation can be attributed to the poor transverse (depth) resolution of the three-dimensional reconstruction which results in the "spreading" of the contrast in that direction. Indeed, consider the depth-integrated contrast, $H(x, y) = \int [\alpha(x, y, z)/\alpha_0 - 1]\,\mathrm{d}z$, where x, y are the coordinates in the plane of the slab and z is the transverse (depth) coordinate. Inside the target, $\alpha(x, y, z)/\alpha_0 \simeq 4$ and the target thickness in the transverse direction is $\Delta z = 0.6\ \mathrm{cm}$. Therefore, the actual value of H for a line passing through the target and perpendicularly to the slab surface is $H \simeq$

$1.8\,\mathrm{cm}$. In the reconstructed images, the transverse thickness of the target is overestimated and is equal, approximately, to $2\,\mathrm{cm}$ while the quantity $\alpha(x, y, z)/\alpha_0$ is underestimated and is equal, approximately, to 2. By using the reconstructed values to estimate the integrated contrast, one obtains $H \simeq 2\,\mathrm{cm}$, which is reasonably close to the actual value. Again, this effect (and analysis scheme) can be useful in practice.

3.5 Summary

The aim of my experiment was to assess the effects of the chest wall on DOT and ultimately to explore methods to mitigate the effect of the chest wall on DOT reconstructions. Both the analytical and the algebraic data-intensive linearized image reconstruction methods produce reasonable results, provided the data points are appropriately restricted to exclude measurements that are strongly influenced by the chest wall. Under these conditions, an absorbing target with sub-ccentimeter features can be clearly reconstructed in the middle of a 6 cm slab, even when the chest wall is only 2 cm from the target. This situation corresponds to breast tumors very near the chest wall. Specifically, good images of the target were obtained even in the presence of a large chest wall phantom that introduces significant nonlinearities into the inverse problem, i.e., due to its larger absorption coefficient compared to the background as well as its large size.

A data restriction condition was discovered such that the presence of the chest wall phantom imposes minimal artifacts or distortions in the image. The image quality of the projections was good and it would be of interest to explore the utility of these reconstructions for improved 2D imaging or improved quantification or in combination with other 2D modalities. The performance of both algebraic and analytic image reconstruction methods were then compared under this condition and, while neither method is perfect, it appears that a role for both methods in DOT exists, the choice depending upon the particular clinical application. For example, the analytical method provides faster reconstruction while suffering from minor artifacts and flexibility. While the algebraic reconstruction method provides slightly better image quality, it will require a library of weight matrices for faster inversion that would have to be stored ahead of time before measurements (see Section 2.2.1.4. We hope to build on these techniques in the future, especially by implementing non-linear approaches or by modification of the Green's function used to account for the chest wall region and its optical properties.

Chapter 4

CCD-based Multispectral Frequency-domain DOT: Instrumentation, Pre-clinical and Clinical Results

4.1 Introduction

Our group at Penn has played a leading role developing Diffuse Optical Tomography (DOT) for breast imaging and, more generally, translating DOT techniques to the clinic [9, 12, 15, 38, 45, 107–110]. My work improves on this research by addressing critical limitations of the early DOT imagers, that last of which I will refer to herein as the Gen2 instrument. These limitations were ascertained through various clinical studies [44, 45, 47, 49, 53, 105].

My DOT imager, which I will refer to herein as the Gen3 instrument, introduced significant new capabilities for improved breast-DOT: 1) A multispectral *frequency-domain* mode of operation in the transmission geometry that employs heterodyne detection; 2) the world's *largest* clinical source-detector *data set* to facilitate high-fidelity 3D DOT reconstruction; 3) multiple channels for *real-time normalization* of instrument phase and amplitude shifts/drifts; and 4) a projection-camera *profilometry system* for defining breast boundaries and thereby facilitating improved breast segmentation; 5) an improved clinical *patient interface*. In this chapter, I will provide an overview of the Gen3 instrument design, and I will discuss its new features. Then I will describe experiments that characterize instrument performance, mainly using tissue simulating phantoms. Finally, first clinical results from breast cancer patients will be presented.

4.2 The Early Optical Breast Imaging Instrument (Gen2)

In order to appreciate the new instrumentation I have built (Gen3), it is necessary to review the inner workings of the Gen2 device. The Gen2 imager is shown schematically in Figure 4.1, and it is described in detail in reference [47, 53]. The Gen2 device derived images of the breast from transmission data, with light traveling through the parallel plate compression geometry. Importantly (and in contrast to Gen3), the Gen2 sources are continuous wave (CW). Source fibers couple input CW light from the diode lasers to the tissue surface; then this illuminating light travels through the breast tissue, and after transmission through the breast the CW light is detected by a CCD camera. Without phase information in the transmission signals (i.e., without information that is only available when the light sources are frequency-modulated or pulsed), the average/background tissue optical properties were estimated from a few frequency-domain

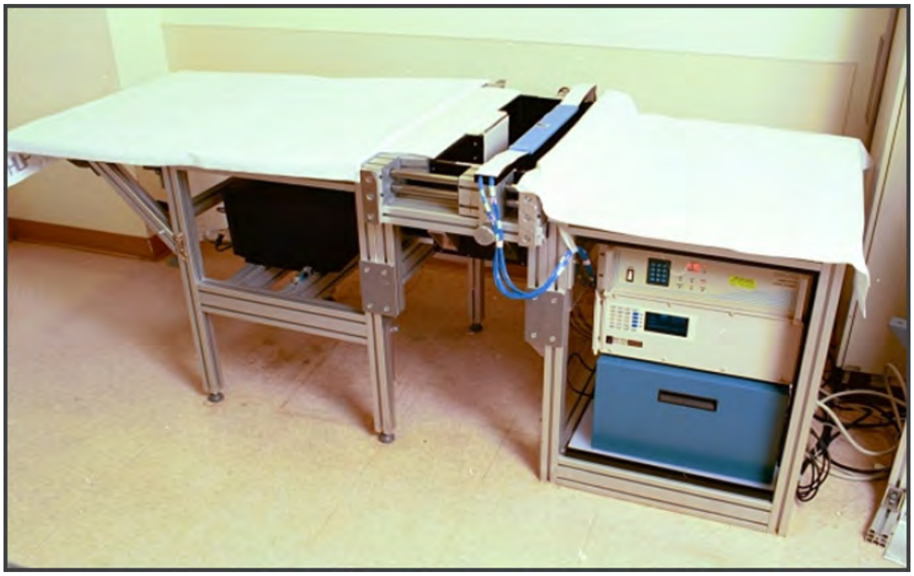

Figure 4.1: Photograph of the previous generation Gen2 breast scanner located at the Hospital of the University of Pennsylvania (HUP).

measurements in remission. Then, by combining these sparse remission frequency-domain data with dense multi-spectral CW transmission data, it is possible to carry out DOT reconstructions.

The DOT measurement is made with the patient lying prone on a flat bed with her breast inserted inside a recessed box. This box has a grid of source fibers on one side (source plate) and a window on the other side (detector plate). The source plate is translated axially to softly compress the breast between the source and detector plates. The box is filled with a matching fluid whose optical properties are similar to those of the average human breast. The matching fluid consists of water, india ink (for absorption) and Intralipid (for scattering).

The Gen2 source plate has 45 fiber positions arranged in a 9x5 square grid with a spacing of 16 mm between nearest neighbors (Figure 4.2). The light is launched in series into the medium using cascading optical switches (DiCon Fiber Optics). At each source position, up to six different light source wavelengths were switched in from the fiber-coupled diode lasers (e.g., at

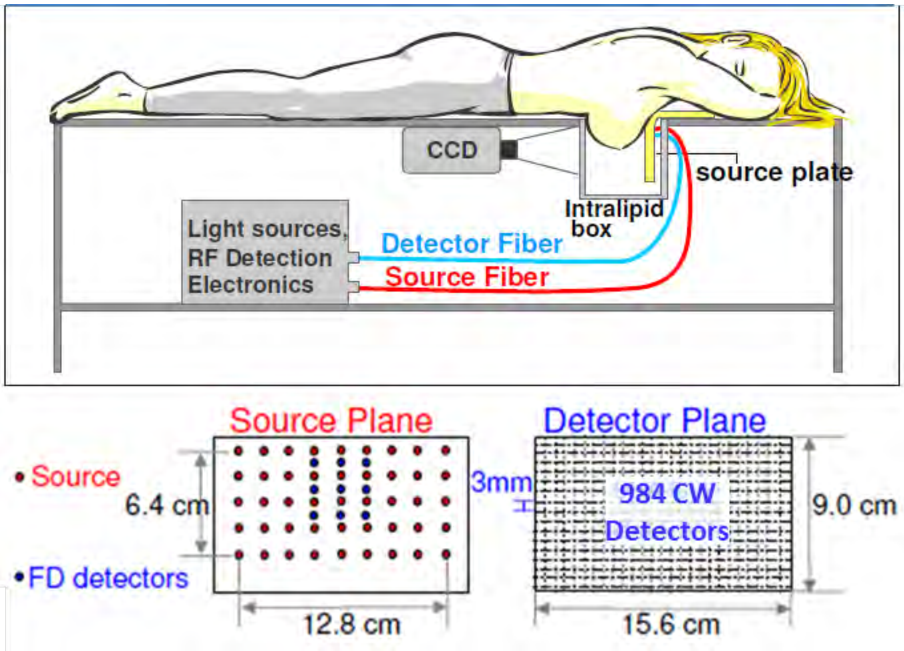

Figure 4.2: Schematic of the Gen2 breast scanner. CW transmission and frequency-domain (FD) remission measurements are taken simultaneously. The patient lies prone, and her breast is compressed axially with the sources and FD detectors on top of the breast and the CCD detection window against the bottom of the breast. The source plate consist of 45 source positions and 9 FD detectors with 16mm spacing between the sources. For the CW transmission measurements, a subset of 984 detectors (pixels) with 3 mm spacing is selected from the CCD for reconstruction. This Figure is adapted from a similar schematic by R. Choe [80]

wavelengths of 650, 690, 750, 785, 830, 905 nm). On the detection side, a CCD camera (Roper Scientific, Trenton, NJ, VersArray:1300F) collected the exiting light in the transmission geometry. A full CCD image is thus obtained for each source (and each laser/wavelength combination) with an exposure time of 500 ms. From each image, a grid of data is selected from the CCD after a 2×2 hardware binning of its pixels. For the frequency-domain remission measurements, typically four lasers ($690, 750, 786$, and 830 nm) are modulated at $70\,\mathrm{MHz}$; measurements are made in remission with 3 mm diameter detector fibers arranged on the source plate in a 3×3 grid with $16\,\mathrm{mm}$ spacing. The light from these remission fibers are collected by an avalanche photodiode for homodyne frequency-domain analysis.

Of course, much was learned using this device, and these studies informed the design and development of my current DOT breast imager. Perhaps most significantly, it was particularly difficult to eliminate cross-talk between tissue absorption and scattering when employing only CW measurements (see Chapter 2). This difficulty is well known in the community; it arises because both tissue parameters (i.e., scattering and absorption) attenuate detected diffuse light when the intervening medium is turbid (e.g., like breast tissue). By using multi-spectral measurements in transmission and sparse frequency-domain measurements in remission, we were able to ameliorate this problem to some degree. However, it was apparent that the apparatus would benefit from a full frequency-domain approach, an approach that I incorporate in my Gen3 instrument with *heterodyne* detection techniques.

Another problem concerned breast compression. The Gen2 instrument carried out breast compression in the axial geometry. For comparison to other medical imaging techniques such as MRI, however, the sagittal compression geometry is better and more common than the axial. The Gen3 device employs sagittal compression. Furthermore, a rotation stage in the Gen3 instrument enables DOT measurements in both sagittal and axial compression geometries.

Still another problem concerned instrumental drifts during the patient data-taking period. We did not measure these drifts *in situ* with the Gen2 instrument. As will be described later in the chapter, I implement two types of reference signals for real-time normalization in the new instrument.

In addition, we employed (in Gen2) only very crude means to define the breast boundaries. For example, we used the primary CCD camera image of the breast (before adding Intralipid) to indicate the position of the breast boundary and then we approximated the remainder of the boundary as an ellipsoidal 3D surface. Improvements on this scheme for specification of the breast boundaries should lead directly to improvements in DOT image reconstructions.

Finally, the patient interface needed improvements to increase patient comfort, breast coverage, and to reduce the extent of the air-Intralipid boundary present in the Gen2 instrument configuration. Taken together, all of the noted limitations and potential improvements (as well as the substantially larger amount of data that was possible to obtain with Gen3) motivated us build a whole new instrument system.

4.3 Clinical Breast Imaging Device (Gen3)

The instrumentation and schematic for the Gen3 clinical breast imager that I built is shown in Figures 4.3, 4.4, 4.5, 4.6, 4.7, 4.8, and 4.9. Here, the patient lies prone and perpendicular to the modified biopsy bed (Figure 4.4) while one breast is centered and sagittally compressed between the source plate and window in the breast tank (Figure 4.8). Typical thickness of compression varies between $56\,\mathrm{mm}$ and $70\,\mathrm{mm}$. As before, the tank is filled with a solution of Intralipid and india ink mixture to match with the tissue optical properties of the patient in the near-infrared (NIR) wavelength range.

The breast imager has several key components. Briefly, the laser system encompasses optics and electronics for generating frequency-modulated source light at various NIR wavelengths. This light is sent through a custom switch to one of 209 source positions on the inside a breast tank wherein the breast is inserted. The breast tank has two sets of profilometry cameras and projectors for determination of the breast boundary which, in turn, facilitates 3D segmentation for image reconstruction. Finally, gain-modulated detection is applied to the transmitted light

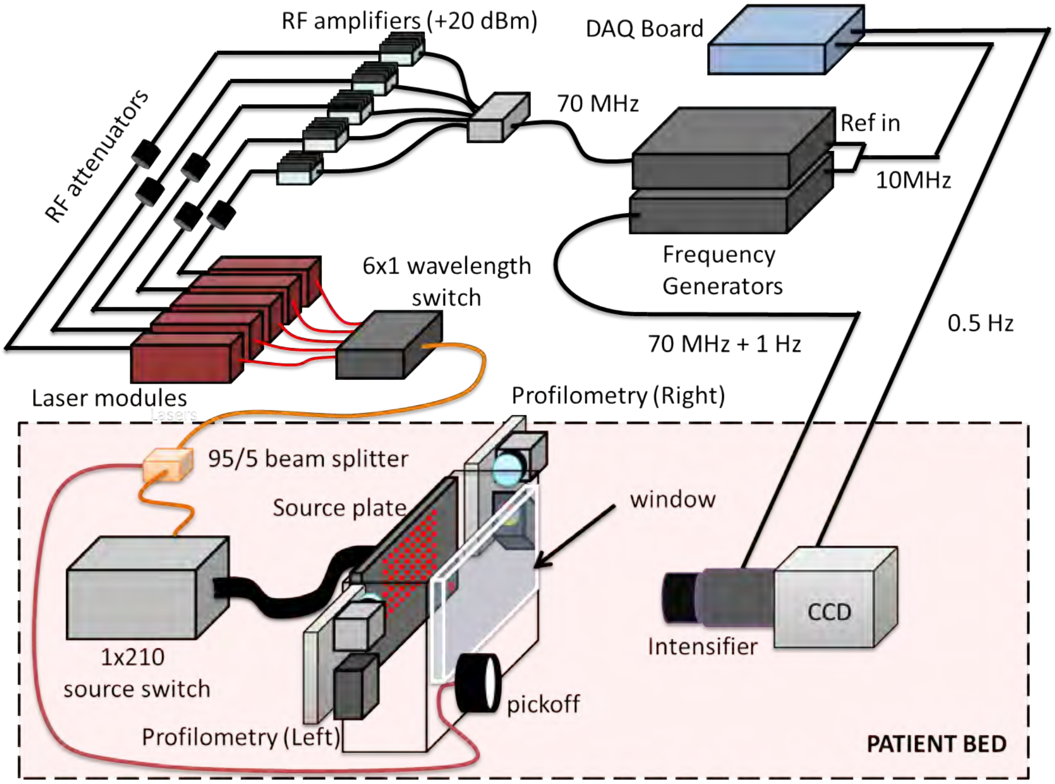

Figure 4.3: Schematic of the DOT breast imager. The source-lasers and detection-system are RF modulated at slightly different frequencies. Five RF modulated laser modules are switched through each source position (in series) to yield multi-spectral data. A 210 channel galvo switch directs the laser light to 209 source positions and a calibration source on the input plate. The patient breast is inserted in the tank between the source plate and window. Profilometry devices on either side of the tank image the sides of the breast. Laser light exiting the tank window is measured by a RF gain-modulated intensifier and CCD.

using an image intensifer mounted on the CCD-camera apparatus.

First and foremost, my DOT breast imaging device improved on the Gen2 instrument through the incorporation of multispectral frequency-domain (FD) laser source illumination and CCD-based heterodyne detection; the latter was enabled by gain-modulation of an image intensifier placed between the sample output and the CCD-detector. These new capabilities improve separation of tissue absorption from tissue scattering and thus improve the quantification capability of the 3D DOT reconstruction. Furthermore, by using an improved CCD camera for detection,

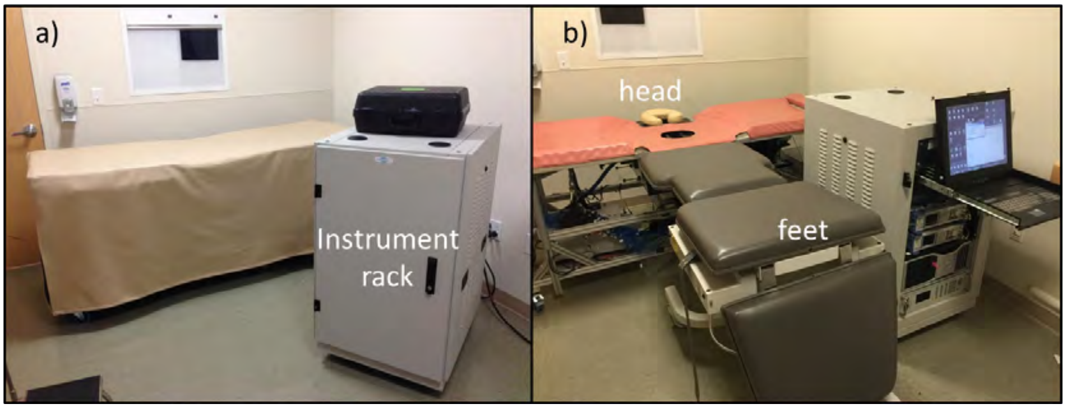

Figure 4.4: The breast imaging instrumentation in the mammography wing of Perelman Center for Advanced Medicine at the Hospital of the University of Pennsylvania (HUP). a) Gen3 instrument when not in use. b) Gen3 instrument set up for patient measurement. The patient would lie in the prone position with her head on the head rest and body along the grey exam table. More details about each sub-part of the instrument will be given throughout this chapter.

we were able to collect a very large number (10^6) of source-detector pairs in parallel, again facilitating improved resolution and image fidelity. In fact, my instrument collects the largest number of source-detector pairs compared to any DOT instrument in the world today, e.g., by factors of 100x or more. I will describe how these components work in later sub-sections of this chapter.

The temperature in the hospital is not be well controlled (i.e., compared to typical physics labs), and the shift from CW to FD electronics makes the instrument susceptible to long term drifts and signal jitter. These issues are especially important when working with RF electronics and long optical fibers ($> 5\,\mathrm{m}$). To address these issues, we have engineered both front-end solutions such as RF shielding and temperature control to improve laser signal stability, and we have also introduced *active concurrent reference measurements* for real time signal correction and normalization. These improvements are novel and are further discussed in Section 4.4.

As noted above, every 3D reconstruction can benefit from knowledge of the breast boundary. In principle, one could use the slab boundary conditions and reconstruct the breast boundary

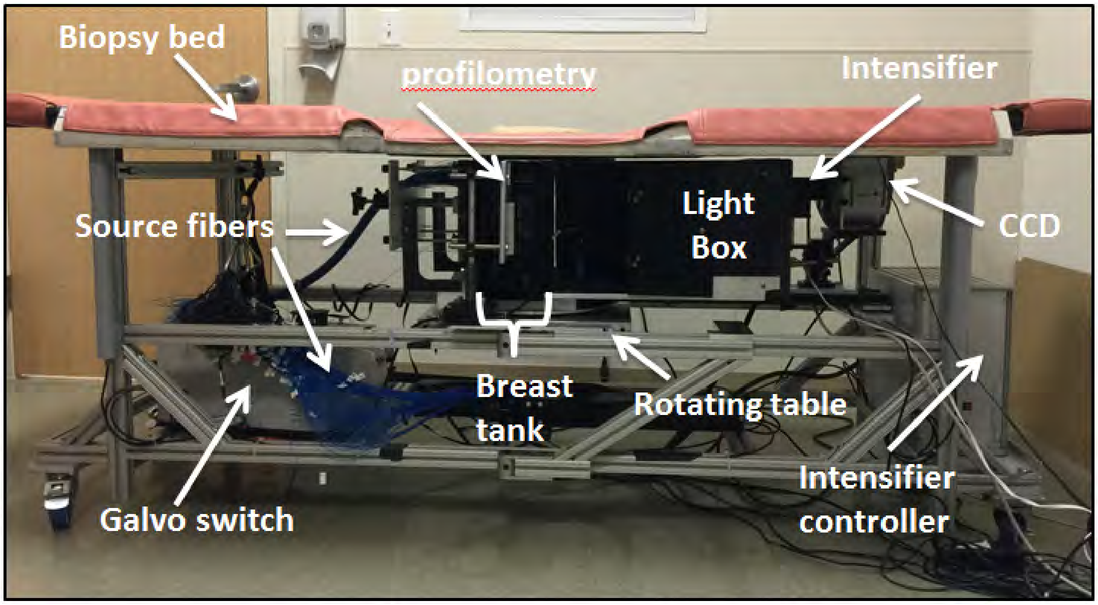

Figure 4.5: Photograph of the of the Gen3 bed with components shown. The bed frame was constructed using 80/20 Industrial erector set for easy modification.

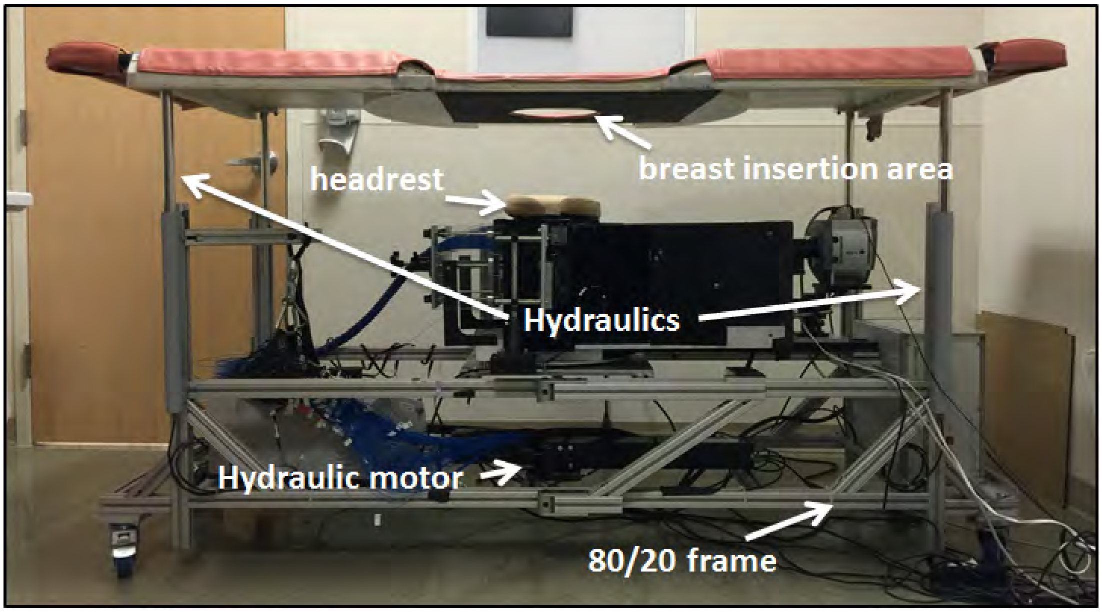

Figure 4.6: Hydraulic system installed on the Gen3 bed for maintenance and setup. It is motorized to be able to lift the heavy stainless steel bed.

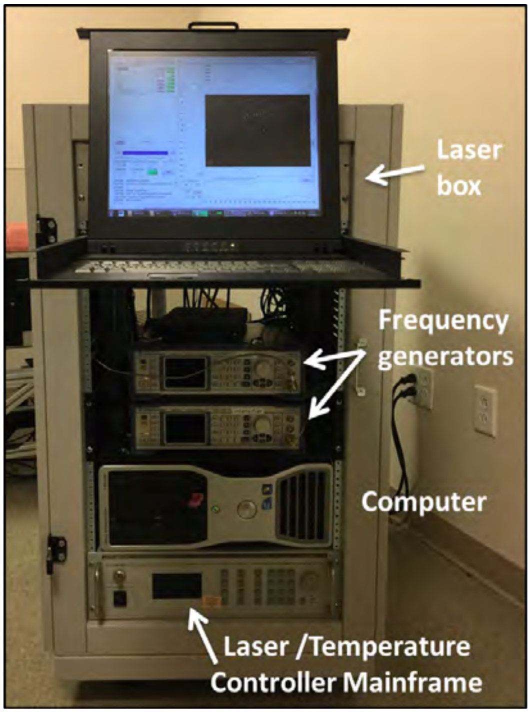

Figure 4.7: Photograph of the instrument's primary electronics rack and related components. This rack contains most of the electronics, as well as the computer that run the Gen3 device. The rack is set next to the patient bed.

directly; in practice, however, if one knows the location of the breast boundary, then one can segment the reconstruction and substantially reduce the number of unknowns in the inverse problem. To this end, a pair of profilometry imaging systems were designed and were built into the new instrument to provide 3D surface information about the breast shape (discussed in Section 4.5). This ancillary instrumentation required overcoming several engineering challenges, e.g., capturing images in the same compression condition as the DOT data, building opto-electronics to work in small spaces (e.g., imaging within $< 6cm$ spacings), compensating and calculating surface information over areas wherein direct imaging could not be carried out, and developing fast acquisition speeds in hardware and software.

Finally, significant effort was made to build a clinical grade device with a patient interface that maximized comfort and minimized movement during measurement. To this end, we designed the bed around a modified breast needle biopsy bed. Since the biopsy bed is designed for maximum breast insertion underneath the bed, we also benefit from resulting greater access to tumors that lie closer to the chest wall. In addition, significant effort was devoted to the design of software for the imager to enable simple and streamlined operation by our clinical collaborators who have minimal technical training. These improvements are further detailed in Section 4.6.

4.3.1 Breast Tank and Patient Bed

The breast imaging system is built around a modified biopsy patient bed (Figure 4.5). The bed permits more of the breast to be inserted into the tank for greater breast coverage, i.e., compared to Gen2. A minor but ultimately important improvement was a translating head-rest that was added to improve neck positioning and comfort (Figure 4.8). The improved patient comfort led to reduced patient motion. In addition, an ultrasound bed permitted the patient to lie perpendicular to the biopsy bed which further improved patient comfort, ease of measurement, and measurement mechanical stability.

The breast tank is located beneath the hole in the biopsy patient bed. The tank consists of a source plate made from black Delrin that is rail-mounted to maintain parallel alignment between the source plate and window during compression. On the opposite side is an acrylic window with an anti-reflective coating in the NIR (Figure 4.9). The space between the window and the detection setup is covered by a light box with an inner lining made of black felt that prevents stray light from reaching the image intensifier and CCD. The tank is mounted above a ball-bearing surface which permits the breast tank, light box, and detection system to rotate 90 degrees for either sagittal or axial compression of the breast. The tank is designed to be fitted with a plastic bag (polyethylene, 3mil) so that the tank can be filled with Intralipid solution. Using an optically matching solution compensates for the uneven thickness of the compressed breast, reducing the dynamic range of the transmitted light signal and boundary effects.

The frame underneath the bed was custom built with 80/20 aluminum T-slot frames that enable further customization and easy modification in the future. The frame rolls on four castor lock wheels for easy movement and rigidity during measurements. Since the stainless steel bed is of considerable weight, hydraulic lifts (47105T23, McMaster-Carr) in Figure 4.6 were added to aid with maintenance and experiment setup/modification during non-clinical use.

4.3.2 Laser System

Source plate illumination is provided by a set of diode lasers operating at wavelengths of 660, 690, 785, 808, and 830 nm, respectively. Table 4.1 provides detailed characteristics of each laser module (Figure 4.11). The laser output on average is about 80 mW from the module fiber tip. The light delivered to the breast ranges in power from 10 to 15 mW. The diode lasers are mounted on a custom copper block coupled to a thermistor and a thermoelectric cooler (TEC) for temperature cooling and control at 13°C with stability within 0.1°C. Each diode laser is driven and temperature controlled by a dedicated ILX module (LDC 391672, ILX). Note, by comparison, the Gen2 instrument used controllers based around a simple driver (Thorlabs, IP500) and lacked temperature control for its lasers. The CW stability of each laser is quite good as a result of these front-end improvements, i.e., the intensity varies by less than 0.5% over three hour periods.

Figure 4.10 shows the schematic of the lasers being amplitude modulated at 70 MHz using a an RF signal from a frequency generator (Rhode and Schwartz, SMB100). More specifically, the

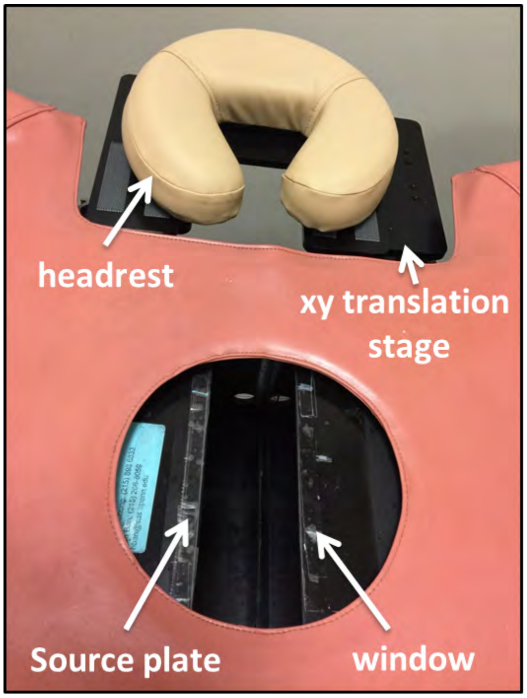

Figure 4.8: Photograph of the bed headrest and breast insertion area. The headrest sits on a translation stage that adjusts for left/right breast positions and height. The breast is compressed between the source plate and the window.

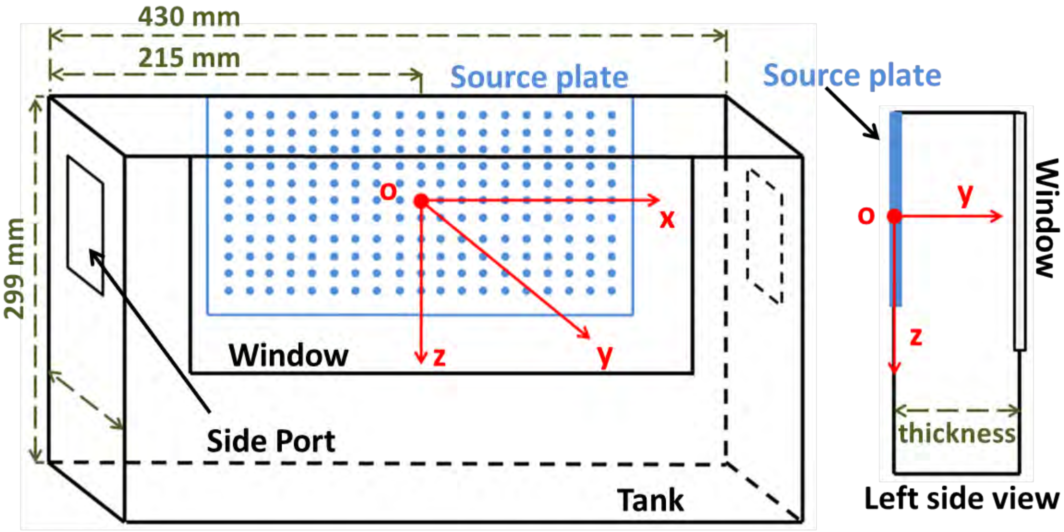

Figure 4.9: Schematic of the gen3tank. The coordinates shown are those used in reconstruction and breast profilometry describe in Section 4.5

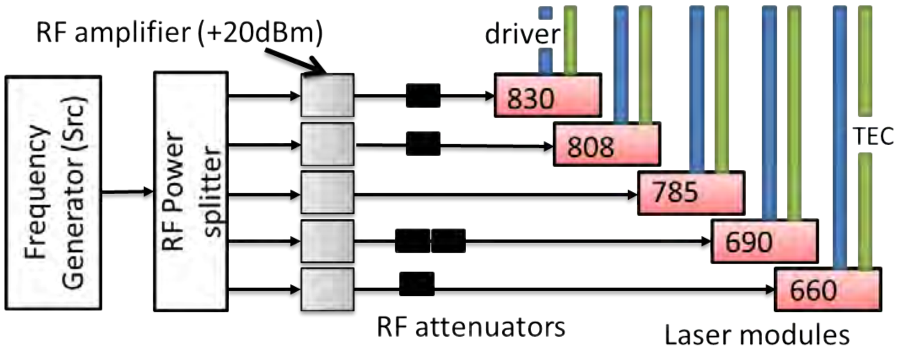

Figure 4.10: Schematic showing laser modules being RF driven. Signal from the frequency generator is divided with an RF power splitter. Each branch is amplified then attenuated to appropriate levels optimized for each laser. Each laser module has a driver and TEC control with feedback. The driver provides CW current which is combined with the RF signal inside the module.

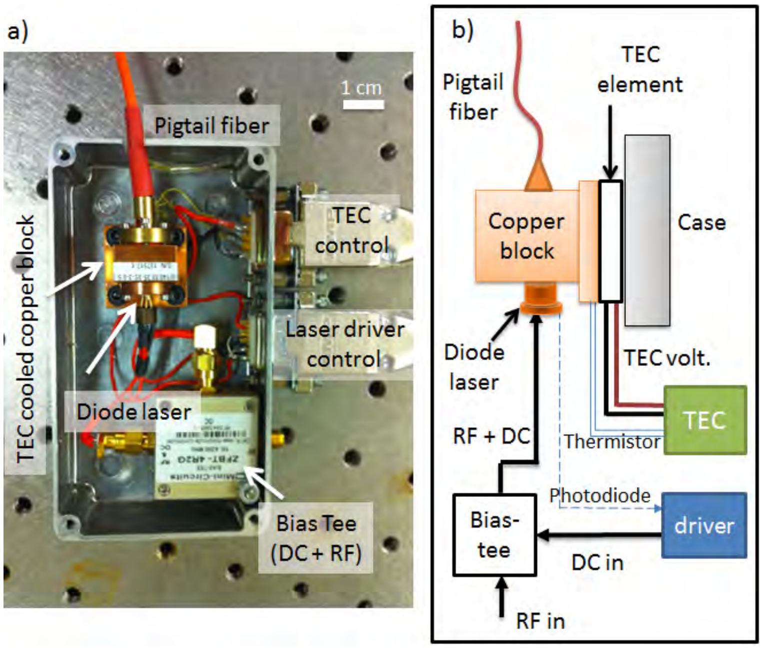

Figure 4.11: a) Photograph of the laser module. b) Schematic of the laser module. The laser module has three inputs: 1) the RF modulation and 2) the DC current drive, which are combined by the bias-tee; 3) the TEC voltage, which drives the cooling element. The module has two outputs: 1) the photodiode (if available) and the 2) thermistor. These outputs provide feedback for the driver current and temperature control, respectively. The cold side of the TEC element cools the copper block to the desired temperature, and heat is released into the module casing.

70 MHz RF signal from the frequency generator is combined with the DC current from the ILX driver for each laser with a bias-tee (Mini-circuits, ZFBT-4R2G). The DC and RF voltage input for each laser was optimized using RF amplifiers (Mini-circuits, ZHL-2010+) and RF attenuators (Mini-circuits, VAT series). The laser driver current is optimized for the best modulation depth (80%) and a sinusoidal waveform. The frequency-modulated light from each laser is then fiber coupled to a 6x1 100 μm core optical switch (Optojenna) which controls wavelength switching in series. A photograph of the laser box is shown in Figure 4.12.

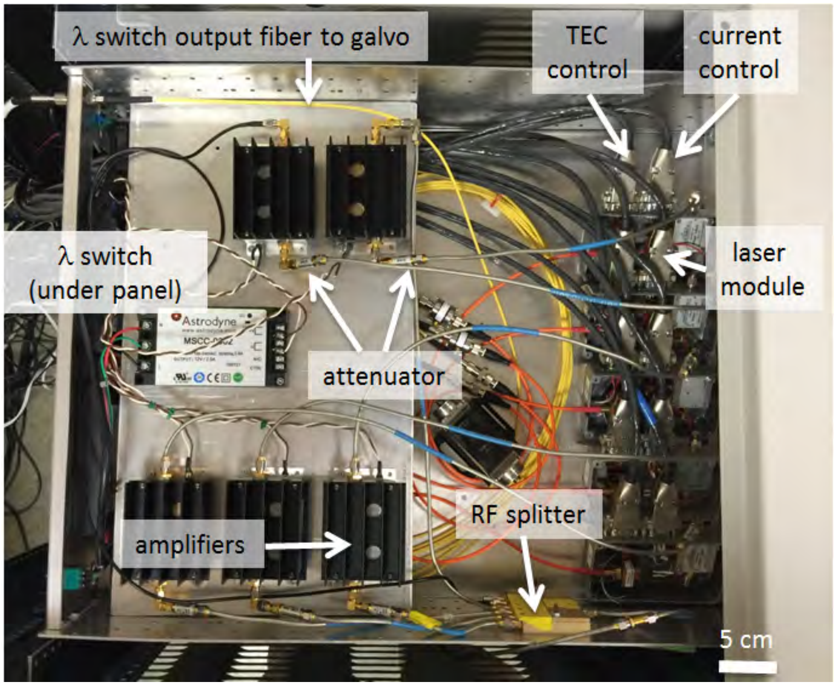

Figure 4.12: Photograph of the laser box. The RF signal (from frequency generator outside of box) is split into five branches, and each is sent through 20dBm amplifiers and then attenuated to the appropriate voltage for each laser module.

λ (nm)	Diode laser part no.	Pin type (Thorlabs)	spec. current typ./max (mA)	current ILX (mA)	AC input (dBm)	power (mW)
660	HL6545MG	H	170 / 210	110	23	45
690	V2561-2	C	768 / 800	425	20	96
785	L785P090	C	120 / 160	93	22	67
808	L808P200	A	230 / 300	180	20	80
830	L830P150	C	200 / 250	123	19	78

Table 4.1: Laser inventory and specifications for the Gen3 device. The ILX driver provides the DC current, and the AC modulation is derived from the RF frequency generator. The laser output power is measured at the end of the pigtail fiber from the laser. Throughput loss is $\sim 80\%$ from the laser module to the source plate.

4.3.3 Source Position Switch and Source Plate

The output fiber from the wavelength switch is connected in series to a $95/5$ fiber beam splitter with the 5% going to the pickoff for signal normalization (which will be discussed in Section 4.4), and 95% going to a custom 1x210 channel optical galvo-switch (Figure 4.13). We upgraded Gen3 to employ a galvo-switch for several reasons. By comparison, the Gen2 system switched through 210 channels with a conventional switch cascade, based on mechanical or prism mechanisms, and it was costly, slow, and had high throughput losses. The Gen2 system switching speed between sources ranged from 0.3 to $0.5\,\mathrm{s}$ and had an average throughput of 50%. More importantly, the Gen2 switches had throughput heterogeneity which ranged from 10% to 80% and which resulted in SNR variation between sources.

The Gen3 galvo-switch, by contrast, has more uniform throughput, i.e., with differences in intensity between sources no greater than 10%. In the galvo switch, input light from a $100\,\mu\mathrm{m}$ core fiber is collimated and sent towards galvo-controlled mirrors which then redirect light into a telecentric lens. This lens focuses the light onto a fiber bundle face with 210 fibers ($600\,\mu\mathrm{m}$ core) as shown in Figure 4.14. Each fiber from the bundle is connected to a custom source fiber with $600\,\mu\mathrm{m}$ core. The source fibers were hand-polished (to achieve 98% throughput) and fitted with FC/PC connector on the end towards the fiber bundle, and a custom ferrule on the end connecting to the delrin source plate.

The 209 source fibers are arranged on an 11x19 square grid on a black delrin plate with 8 mm spacing. The source plate is moved against the detection window and a picture is taken to determine source positions for reconstruction as shown in Figure 4.15. One of the remaining fibers is used as a calibration source and is thus placed far from the source grid. The purpose and implementation of this calibration source will be discussed in Section 4.4.

4.3.4 Image Intensifier mounted CCD

The detection system consists of a back-illuminated EMCCD (Andor iXon DV887, Ireland) with quantum efficiency optimized in the $500 - 700\,\mathrm{nm}$ range as shown in Figure 4.16. One of the most attractive features of this CCD is its "frame transfer" function which permits *shutter-less* continuous measurement; this feature is beneficial for our heterodyne measurement scheme which is described in Section 4.3.5. CCDs with frame transfer options feature a second CCD chip that acts as a buffer while the first chip continues to be exposed. The speed at which it shifts the data to this secondary chip is roughly $3\,\mu\mathrm{s}$ per row of pixels. This allows for a series of exposures to be taken continuously without a need for a mechanical shutter. The 512×512 pixel CCD is cropped to a field-of-view corresponding to the breast tank window; with a 2×2 hardware binning this set up produces an image 155×200 pixels with a dpixel of $1.2268\,\mathrm{mm/pixel}$ with a 16-bit depth. The CCD is mounted together with a relay lens and with a gain-modulated image intensifier (Lambert Instruments, II8MD GENIII, Netherlands) that has a P43 Phosphor screen with a peak emission at $545\,\mathrm{nm}$. The lens element in front of the image intensifier is a Xenon $25\,\mathrm{mm}$ $f/0.95$ C-Mount Lens for 1-Inch CCD (Schneider Optics, Germany).

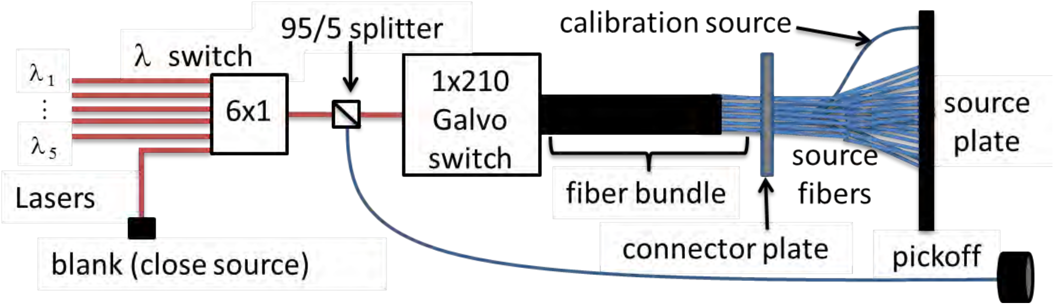

Figure 4.13: Schematic of switches and fibers in the Gen3 system. The output light from the laser modules are fiber-coupled to a 6×1 wavelength switch. Output of the wavelength switch is then directed through a beam splitter with 5% going to a pickoff source which is used as an instrument source reference. The remainder is input to a 1×210 galvo switch which redirects the light into one of 210 channels of a fiber bundle. The fiber bundle is connected via custom source fibers to the source plate. 209 of the fibers are arranged in a 11×19 square grid with $8\,\mathrm{mm}$ separation, and one of the channels is used as a (second) calibration source placed far from the breast measurement area.

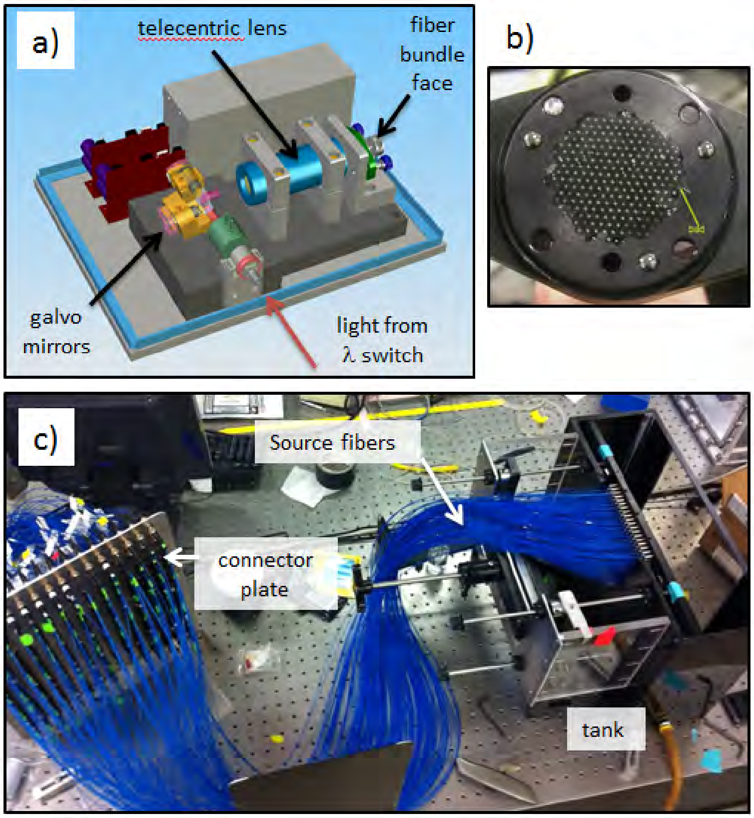

Figure 4.14: Photograph of the (a) galvo switch, (b) the input face of the fiber bundle, and (c) the custom source fibers and source plate

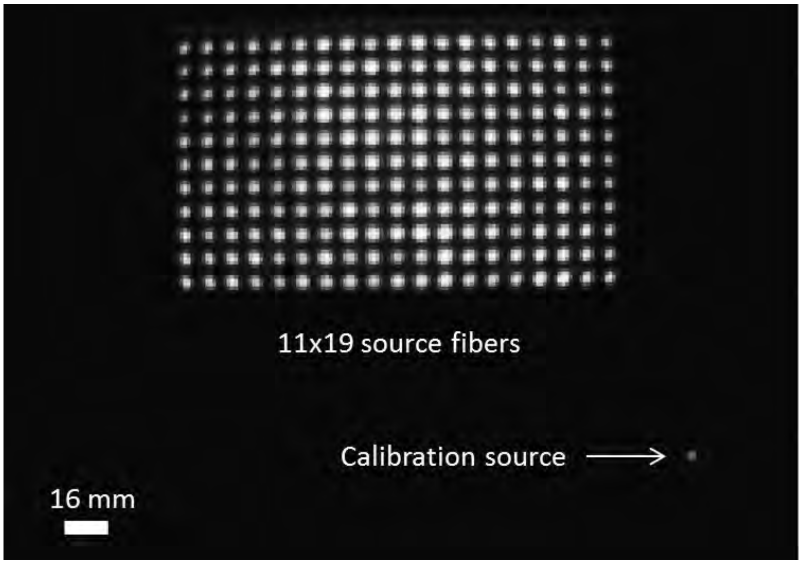

Figure 4.15: Source plate photograph taken by the Breast Imager CCD after it has been moved to the detection window. The fibers are lit by illuminating the back end of the fiber bundle. In practice, this image is used to provide fairly precise estimates of the source positions for the tomographic reconstructions. The spacing between sources are $8\mathrm{mm}$ between nearest neighbors.

Briefly, the image intensifier works by converting light into electrons which are then amplified electronically before being converted back to light again (at the phosphor screen). Specifically, incident light on the cathode (coated with a photosensitive compound) of the image intensifier is converted to electrons via the photoelectric effect. When the voltage applied to the cathode is negative, a potential difference between the cathode and anode is created and causes electrons to move (accelerate) towards the anode. When a positive voltage is applied to the cathode, the image intensifier is effectively ”off”; the electrons do not escape to the anode. When the intensifier is on, the electron travels through the multichannel plate (MCP) and the number of electrons is amplified/increased. These electrons are converted back into light when they strike the phosphor screen at the back of the intensifier. This amplified light signal is then focused onto the CCD by the relay lens. The electronic schematic for this process is shown in Figure 4.17.

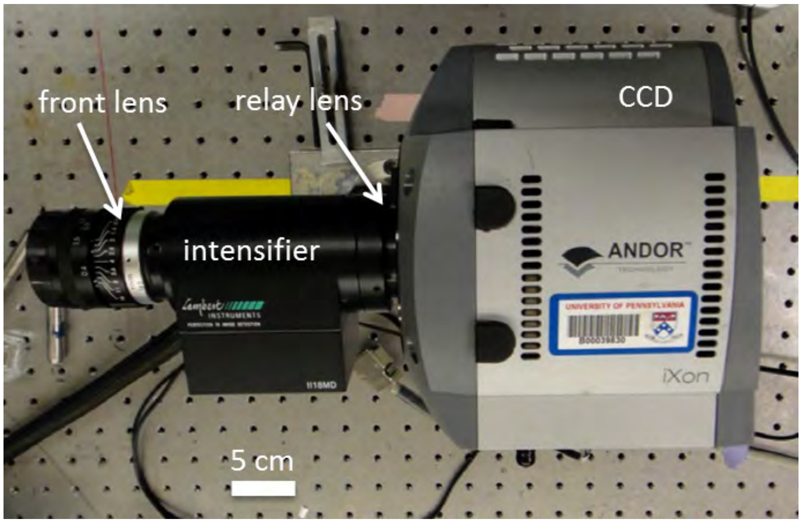

Figure 4.16: A photograph of our CCD with a Lambert instruments image intensifier mounted in the front.)

The gain on the image intensifier is modulated at the cathode with a frequency of $70\,\mathrm{MHz} + 1\mathrm{Hz}$, thereby permitting *heterodyne* detection as described in the next section.

4.3.5 Frequency-Domain Heterodyne detection

The primary goal of the frequency-domain DOT system is to measure the AC amplitude and phase components of the signal for each source detector pair. Generally, two approaches are used to demodulate a high frequency RF signals: homodyne and heterodyne. Several homodyne systems have been developed for diffuse optical imaging [173–175], including in our lab, but here we describe the heterodyne approach. The heterodyne approach usually has better signal-to-noise than homodyne schemes, as the signal can be filtered and is received at the cross-correlation frequency (f_{cc}); by working away from zero-frequency, the heterodyne measurement exposure to so-called pink ($1/f$) noise (and other noise) is less [112]. Heterodyne

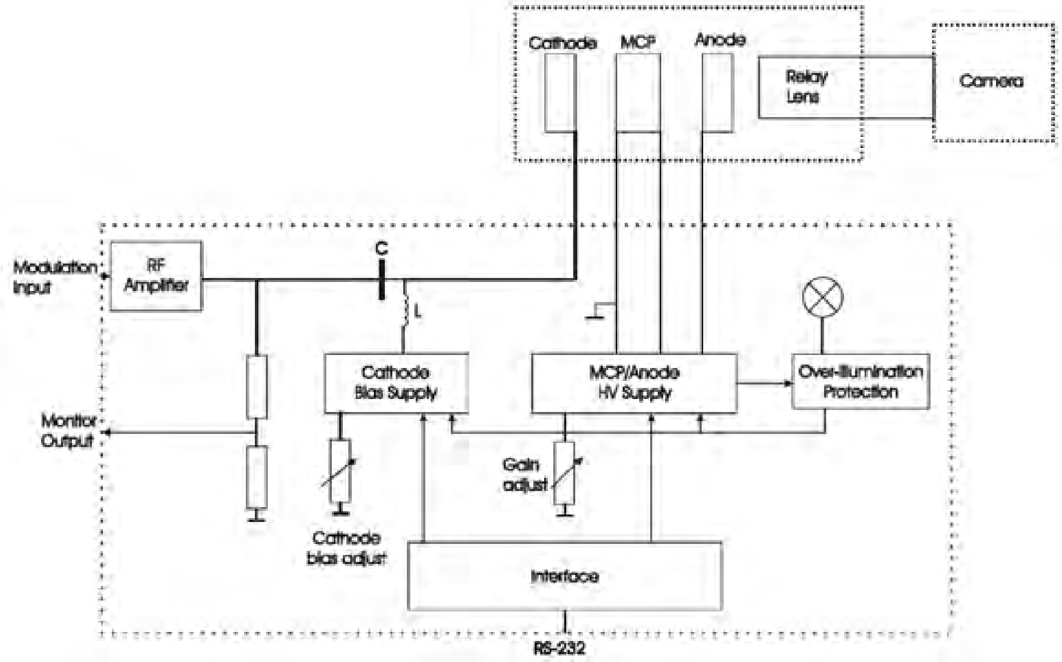

Figure 4.17: Schematic of the image intensifier electronics. The cathode converts light into electrons which are amplified by the MCP. The image intensifier gain is RF modulated at the cathode. (*Figure from Lambert Instrument manual for II8MD*)

detection also better enable concurrent amplitude and phase corrections via the pickoff normalization/calibration signals thereby facilitating corrections to long-term drifts (see Section 4.4.

Our system uses an optical heterodyne detection scheme wherein an input source is modulated at frequency, f_s, is mixed (nonlinearly) with a reference detection signal modulated at a similar frequency $f_d = f_s + f_{cc}$ where $f_{cc} = 1$ Hz. In our instrumentation, the reference signal is used to alter the detector gain. The result is that the detected light signal has a component that oscillates at the beat frequency f_{cc} from which the amplitude and phase data can be extracted. In our system, the modulation frequencies at f_s and f_d are provided by a pair of phase-locked frequency generators (Rohde and Schwarz, SMA100A).

The lasers are amplitude modulated at $f_s = 70\,\mathrm{MHz}$. Therefore, the light source power density in the sample entrance is given by

$$S_s(\mathbf{r}_s, t) = S_{dc}(\mathbf{r}_s) + S_{ac}(\mathbf{r}_s)\cos(2\pi f_s t)\ . \tag{4.1}$$

Here the angular frequency and the frequency are related according to $f = \omega/2\pi$, and $\mathbf{r_s}$ denotes the spatial position of the source. For example, for a point-like source, the source function would be a delta function in space. (Note, unlike Chapter 2, here we are not using complex notation for the source and fluence rate.) When the light passes through the breast tank (i.e., through breast and/or Intralipid solution), then the measured fluence rate, Φ, will be of the form

$$\Phi(\mathbf{r}_s, \mathbf{r}_d, t) = \Phi_{dc}(\mathbf{r}_s, \mathbf{r}_d) + \Phi_{ac}(\mathbf{r}_s, \mathbf{r}_d)\cos(2\pi f_s t + \theta(\mathbf{r}_s, \mathbf{r}_d))\ . \tag{4.2}$$

Here Φ_{dc}, Φ_{ac}, and θ represent the DC amplitude, AC amplitude and AC phase shift, respectively. These factors all depend on source and detector positions; of course, in addition, the properties of the medium are impressed onto the light fluence-rate as it traverses the medium from the source position $\mathbf{r}_s$ to detector position $\mathbf{r}_d$. Thus, these are the functions that contain information about the sample. This information about the sample properties is ultimately derived from the data via DOT inversions (see Chapter 2). The inversions yield optical absorption and scattering coefficients, i.e., tissue optical properties. Herein I will drop $\mathbf{r}_s$ and $\mathbf{r}_d$ and assume that the equations refer to diffuse light measured for a specific source-detector pair (i.e., a single light source and a single pixel detector); these omissions simplify notation in the equations below.

The detection gain response of the image intensifier is shown in Figure 4.18. The gain is controlled by the voltage level applied to the cathode. In our experiments, we apply a reference

RF voltage signal to the cathode which has both DC offset and AC voltage modulation. The reference modulation frequency is f_d. When the voltages are set properly, the reference signal turns the image intensifier gain on and off and thus produces a time-dependent gain. This time-dependent gain effectively serves as a diffuse light signal sampler which, in turn, enables us to derive Φ_{ac}, and θ.

Specifically, the cathode DC voltage is set by the intensifier controller, and the AC voltage modulation is derived from the second frequency generator (modulated at $70\,\mathrm{MHz} + 1\,\mathrm{Hz}$). Typically, the cathode DC offset is set to $0.8\,\mathrm{V}$ and the amplitude of the AC modulation is set to $1.8\,\mathrm{V}$. (As an aside, this corresponds to a frequency generator output setting of $-13\,\mathrm{dBm}$.) The gain is ”off” until the modulation causes the bias to run up and down the linear part of the gain curve at cathode voltages below $-1\mathrm{V}$, as shown in Figure 4.18. The overall effect of this reference modulation signal is to produce a gated gain curve with frequency f_d; the gain modulation is essentially a series of pulses with narrow time-width and a repetition period set by the reciprocal of f_d. This method is a commonly used technique for gated detection and sampling.

In our analysis, we will approximate the time-dependent gain function by a series of Dirac delta functions; the delta functions peak at $t = nT_d$, where $T_d = 1/f_d$ and n is an integer. In our instrument, of course, each pulse in the comb will have a finite temporal width, but this width will only change our results by a proportionality constant.

We thus model our detection system gain as a Dirac comb of pulses modulated at $70\,\mathrm{MHz} +$

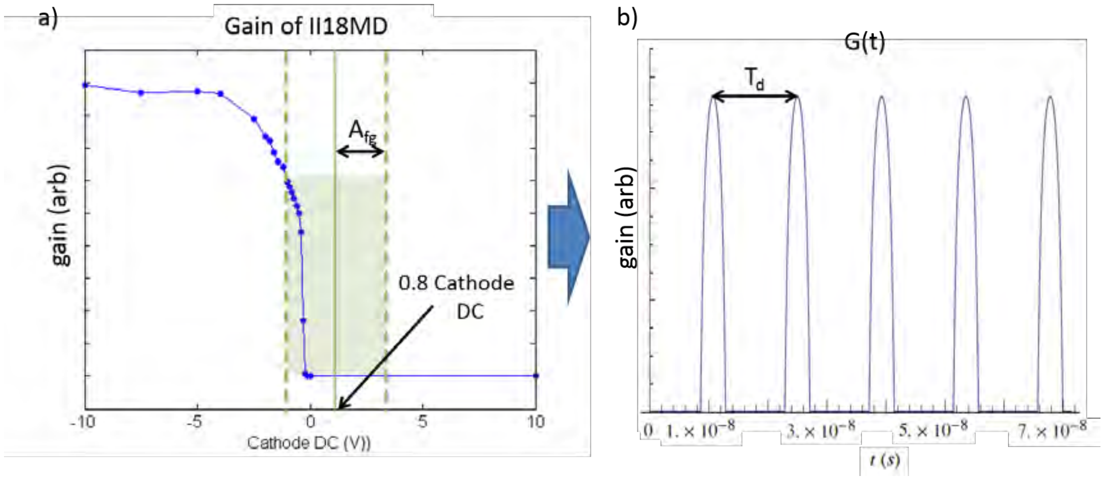

Figure 4.18: a) Measured gain response curve for the image intensifier for various cathode voltage values. Green solid line shows where the cathode DC value is set to $0.8\,\mathrm{V}$. Shaded region between dotted lines show the input AC voltage modulation range from the frequency generator with an amplitude of $1.8\,\mathrm{V}$. b) Schematic of intensifier gain as a function of time (due to the reference modulation). These curves will be approximated as a comb of delta functions for the analysis.

1 Hz. The equation for the gain, in this case, is:

$$G(t) \equiv \sum_{n=-\infty}^{\infty} \Bigg(G_0\, \delta(t - nT_d)\ . \tag{4.3}$$

where G_0 is some effective gain constant which will ultimately be normalized out and $T_d = 1/f_d$ is the repetition period of our gain modulation. The measured signal, M, at the CCD is therefore simply the product of Equation 4.2 and 4.3:

$$\begin{aligned} M(t) &= \Phi(t)G(t) \\ &= (\Phi_{dc} + \Phi_{ac}\cos(2\pi f_s t + \theta)) \quad \sum_{n=-\infty}^{\infty} \Bigg(G_0\, \delta(t - nT_d)\Bigg)\Bigg(. \end{aligned} \tag{4.4}$$

To further simplify this equation we will utilize the convolution theorem. To do so we take the Fourier transform of the fluence rate and gain. The Fourier transform for the fluence rate is

$$\begin{aligned}\hat{\Phi}(f) &= \int_{-\infty}^{\infty} \left(\Phi_{dc} + \Phi_{ac}\cos(2\pi f_s t + \phi)\right) e^{-2\pi i f t} dt \\ &= \Phi_{dc}\delta(f) + \frac{\Phi_{ac}}{2}\left(\delta(f - f_s)e^{i\theta} + \delta(f + f_s)e^{-i\theta}\right) \ . \qquad (4.5)\end{aligned}$$

The Fourier transform of a Dirac comb is

$$\hat{G}(f) = \frac{1}{T_d}\sum_{n=-\infty}^{\infty} G_0\,\delta\left(f - \frac{n}{T_d}\right) \ . \qquad (4.6)$$

Now the convolution of Equation 4.5 and 4.6 is

$$\begin{aligned}\hat{M}(f) &= \hat{\Phi} * \hat{G} \\ &= \int_{-\infty}^{\infty}\left[\Phi_{dc}\delta(f') + \frac{\Phi_{ac}}{2}\left(\delta(f' - f_s)e^{i\theta} + \delta(f' + f_s)e^{-i\theta}\right)\right]\hat{G}(f - f')df' \\ &= \Phi_{dc}\hat{G}(f) + \frac{\Phi_{ac}}{2}\left(\hat{G}(f - f_s)e^{i\theta} + \hat{G}(f + f_s)e^{-i\theta}\right) \ . \qquad (4.7)\end{aligned}$$

Using the definition of the Dirac Comb in Equation 4.3, Equation 4.7 becomes

$$\begin{aligned}\hat{M}(f) = \frac{G_0}{T_d}\sum_{n=-\infty}^{\infty} &\left[\Phi_{dc}\delta\left(f - \frac{n}{T_d}\right)\right. \\ &\left. + \frac{\Phi_{ac}}{2}\left(\delta\left(f - f_s - \frac{n}{T_d}\right)e^{i\theta} + \delta\left(f + f_s - \frac{n}{T_d}\right)e^{-i\theta}\right)\right] . \qquad (4.8)\end{aligned}$$

Next, we compute the lower order terms. Expanding the first term ($n = 0$) we get

$$\hat{M}_0(f) = \frac{G_0}{T_d}\left[\Phi_{dc}\delta(f) + \frac{\Phi_{ac}}{2}\left(\delta(f - f_s)e^{i\theta} + \delta(f + f_s)e^{-i\theta}\right)\right] . \tag{4.9}$$

For which the inverse Fourier transform is

$$M_0(t) = \mathcal{F}^{-1}\left[\hat{M}_0(f)\right] = \frac{G_0}{T_d}\left(\Phi_{dc} + \Phi_{ac}\cos(2\pi f_s t + \theta)\right) . \tag{4.10}$$

For $n = 1$

$$\begin{aligned} M_1(f) &= \frac{G_0}{T_d}\left[\Phi_{dc}\delta\left(f - \frac{1}{T_d}\right) + \frac{\Phi_{ac}}{2}\left(\delta\left(f - f_s - \frac{1}{T_d}\right)e^{i\theta} + \delta\left(f + f_s - \frac{1}{T_d}\right)e^{-i\theta}\right)\right] \\ &= \frac{G_0}{T_d}\left[\Phi_{dc}\delta(f - f_s - f_{cc}) + \frac{\Phi_{ac}}{2}\left(\delta(f - 2f_s - f_{cc})e^{i\theta} + \delta(f - f_{cc})e^{-i\theta}\right)\right] . \end{aligned} \tag{4.11}$$

Here I have made the substitution $f_d = f_s + f_{cc}$ in the last step. The corresponding inverse Fourier transform is

$$M_1(t) = \frac{G_0}{T_d}\int_{-\infty}^{\infty}\Big[\Phi_{dc}\delta(f - f_s - f_{cc}) \tag{4.12}$$

$$+ \frac{\Phi_{ac}}{2}\left(\delta(f - 2f_s - f_{cc})e^{i\theta} + \delta(f - f_{cc})e^{-i\theta}\right)\Big]e^{2\pi i f t}df . \tag{4.13}$$

Similarly for $n = -1$

$$M_{n=-1}(t) = \frac{G_0}{T_d}\int_{-\infty}^{\infty}\Big[\Phi_{dc}\delta(f + f_s + f_{cc}) \tag{4.14}$$

$$+ \frac{\Phi_{ac}}{2}\left(\delta(f + f_{cc})e^{i\theta} + \delta(f + 2f_s + f_{cc})e^{-i\theta}\right)\Big]e^{2\pi i f t}df . \tag{4.15}$$

Combining M_1 and M_{-1} gives us

$$\begin{aligned}
M_1(t) + M_{-1}(t) = {} & \frac{G_0\Phi_{dc}}{T_d}\int_{-\infty}^{\infty}\Big(\delta(f - f_s - f_{cc}) + \delta(f + f_s + f_{cc})\Big)e^{2\pi i f t}df \\
& + \frac{G_0\Phi_{ac}}{2T_d}\int_{-\infty}^{\infty}\Big(\delta(f - 2f_s - f_{cc})e^{i\theta} + \delta(f + 2f_s + f_{cc})e^{-i\theta}\Big)e^{2\pi i f t}df \\
& + \frac{G_0\Phi_{ac}}{2T_d}\int_{-\infty}^{\infty}\Big(\delta(f - f_{cc})e^{i\theta} + \delta(f + f_{cc})e^{-i\theta}\Big)e^{2\pi i f t}df \\
= {} & \frac{G_0\Phi_{dc}}{2T_d}\cos(2\pi f_s t) + \frac{G_0\Phi_{ac}}{4T_d}\cos(2\pi(2f_s + f_{cc}) + \theta) \\
& + \frac{G_0\Phi_{ac}}{4T_d}\cos(2\pi(f_{cc}) + \theta)\ . \qquad (4.16)
\end{aligned}$$

One can then write down the full series for $M(t)$ as

$$\begin{aligned}
M(t) = {} & \frac{G_0}{T_d}\Big(\Phi_{dc} + \Phi_{ac}\cos(2\pi(f_s + f_{cc})t + \theta)\Big) && (M_0\,\text{term}) \\
& + \frac{G_0\Phi_{dc}}{2T_d}\cos(2\pi f_s t) + \frac{G_0\Phi_{ac}}{4T_d}\cos(2\pi(2f_s + f_{cc}) + \theta) && \\
& + \underline{\frac{G_0\Phi_{ac}}{4T_d}\cos(2\pi(f_{cc}) + \theta)} && (M_{\pm 1}\,\text{term}) \\
& + \frac{G_0}{T_d}\sum_{n=2}^{\infty}\Big[\frac{G_0\Phi_{dc}}{2}\cos(2\pi n f_s t) + \frac{G_0\Phi_{ac}}{4}\Big(\cos(2\pi(f_s - n f_d)t + \theta) && \\
& \qquad + \cos(2\pi(f_s + n f_d)t + \theta)\Big)\Big]\ . && (n \geq 1\,\text{terms})
\end{aligned}$$

$$(4.17)$$

This equation provides the light fluence-rate incident on the CCD for a given pixel. Note that one DC and one $1\,\text{Hz}$) term arise. All other terms oscillate at a frequency of $\sim$ 70MHz or greater.

In the experiment, the response time of the detection is limited by our CCD exposure time which is only very slightly less than $\sim 100\,\text{ms}$ (note also, the frame transfer function of the CCD is 10Hz). Any term with a modulation frequency greater than $10\,\text{Hz}$ (and certainly any term in the MHz range) will average to zero:

$$M(t) \propto G_0\Phi_{dc} + \underline{\frac{G_0\Phi_{ac}}{4}\cos(2\pi f_{cc}t + \theta)} + 0\,\big(\text{higher freq. terms}\big)\ . \tag{4.18}$$

Of course, in practice the measurement is scaled with the camera aperature, gain pulse width, exposure time, pixel size, etc., all of which affect the number of electrons that charge up the CCD pixel (and all of which are canceled out by normalization). Equation (4.18) is the equation we use to determine the values of Φ_{dc}, Φ_{ac} and θ from the raw data. This conversion is the first step in our data preprocessing.

4.3.6 DOT measurement and timing

The measurement timing is controlled using a National Instruments DAQ board (NI USB-6351) which has an onboard clock, as well as analog and digital I/O that can be programmed with Labview (Figure 4.3). The DAQ board output two synchronized clocked TTL signals at $10\,\mathrm{MHz}$ and $0.5\,\mathrm{Hz}$. The $10\,\mathrm{MHz}$ goes to the reference input of the two frequency generators to phase-lock the two generators. The 0.5Hz signal is sent to the CCD to trigger the 17-point sequential measurement series, thereby synchronizing to the heterodyne measurement (see Figure 4.3).

In our measurement protocol we switch through all the source positions for each wavelength in series. The measurement at each source position takes two seconds (each triggered by the $0.5\,\mathrm{Hz}$ DAQ signal) resulting in a total measurement time per scan of $2\,\mathrm{s} \times 209\,\mathrm{sources} \times 5$ wavelengths $\sim$ 35 minutes. For each two second measurement, 17 exposures are captured at at $10\,\mathrm{frames/s}$ for a total of $1.7\,s$. The remaining $300\mathrm{ms}$ is used to write data from the camera buffer to the computer hard-drive and to switch to the next source position and/or wavelength.

4.4 Data Preprocessing

The raw data captured by the Gen3 imager must be preprocessed to determine the Φ_{ac} and θ values for each source-detector pair (i.e., pixel) from the heterodyne measurement discussed in Section 4.3.5. A 17-frame series measurement for a single source position and wavelength is shown in Figure 4.19 (a). Notice, in the bottom left corner of this image we can observe the pickoff reference signal; its variation (as measured by a single pixel) is shown over time at the top of Figure 4.19 (b). In the center of the field-of-view, we exhibit the signal image from source position 200. Data from several of the nearby pixels (indicated by 2-5 in a)) are shown on the bottom of Figure 4.19 (b). Note the decrease in the AC and DC amplitude, as well as the shift phase with increasing pixel number (i.e., with increasing source-detector distance).

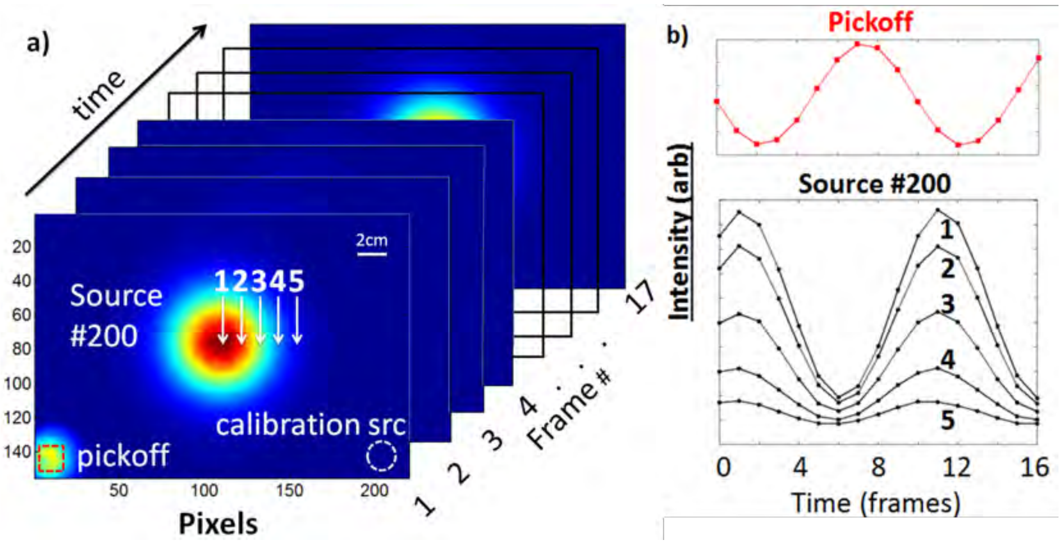

Figure 4.19: a) Full field time series of light measured by the CCD. The pickoff is in the bottom left corner and measured concurrently. The calibration source is located on the bottom right and taken in series b) (Top) Light signal for a pixel in the pickoff region as a function of time (17 frames shown). (bottom) Light signal for different pixels (indicated in (a)) as a function of time. This data is fit to derive Φ_{ac}, and θ.

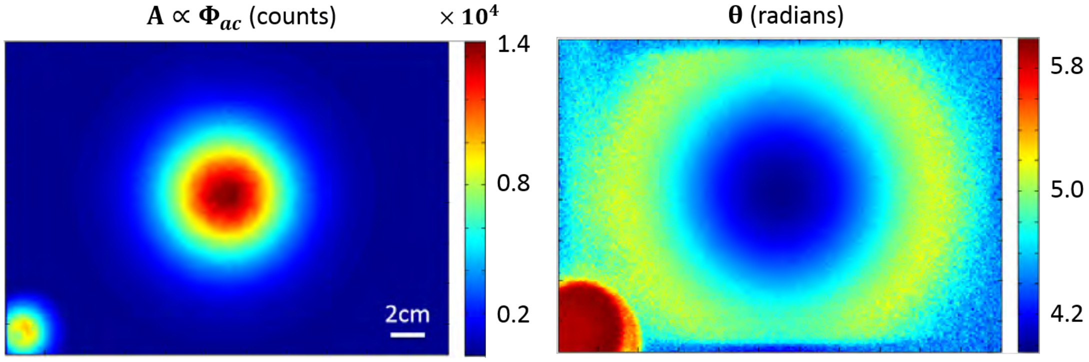

Figure 4.20: Φ_{ac} and θ images after preprocessing for source 200. Every pixel in each image corresponds to a specific source-detector pair with an assigned value for $\Phi_{ac}(\mathbf{r_d}, \mathbf{r_s})$ and $\theta(\mathbf{r_d}, \mathbf{r_s})$

The Gen3 instrumentation utilizes the pickoff channel shown in Figure 4.3 to correct for changes in phase due to laser or RF instabilities; this pickoff channel, however, will only account for fluctuations that occur in the source-chain section before the light enters the galvo-switch. This is the reason that we picked off five percent of the light using the $95/5$ optical beam splitter; the 5%-light is coupled into a fiber whose output is set in front of the detection window. Further, a 1-inch thick white delrin is placed in front of the fiber tip and is used as a light diffuser. Importantly, because it is placed in the field-of-view (FOV) of the detection window, this reference signal is obtained concurrently with each source measurement. (Note, an attenuator is added into the pickoff signal pathway so that the light level will be appropriate for the gain and dynamic range of the DOT measurement).

Using the pickoff channel signal, preprocessing of the data is implemented in two steps:

1. First fit pickoff signal to obtain: $A_{pick} \sin(2\pi f_{cc} t + \theta_{pick})$ (red dotted square shown in Figure 4.19).
2. Then fit signal of remaining pixels over time to obtain: $A \sin(2\pi f_{cc} t + \theta - \theta_{pick})$.

After these operations, we have obtain A (which is $\propto \Phi_{ac}$) and θ, with the phase offsets from the detection system (i.e., θ_{pick}) corrected. The preprocessed data is shown in Figure 4.20.

A single breast scan enable us to determine $A = C\Phi_{ac}$ and θ (with some constant source-detector offset θ_{offset}). (See the equations in Section 4.3.5; C is some unknown coupling constant that, ideally, is expected to be a unique number for each source-detector pair). However, the quantities that we are interested in are Φ_{ac} and θ (i.e., without the coupling factor and offset) which are due solely to the optical properties of the breast. By taking a second reference scan with the Intralipid solution alone, we can divide out coupling constants C and subtract out the source offset. For example, from Equation 4.18 we can fit the data to derive the amplitude and phase associated with each source-detector pair for the breast/phantom measurement and for the reference Intralipid measurement. In this case, the needed amplitude ratio and the needed phase shift between sample and reference measurements are readily determined for each source-detector pair, i.e.,

$$\frac{A_{breast}}{A_{ref}} = \frac{C\Phi_{ac,breast}}{C\Phi_{ac,ref}} = \frac{\Phi_{ac,breast}}{\Phi_{ac,ref}} \; ; \tag{4.19}$$

$$\left(\theta_{breast} - \theta_{offset}\right) - \left(\theta_{ref} - \theta_{offset}\right) = \left(\theta_{breast} - \theta_{ref}\right) . \tag{4.20}$$

This kind of normalization method is critical to implement, but, unfortunately, the approach has limitations, especially since measurements are taken in series. Specifically, since each scan takes 35 minutes, any drifts that occur in the signal (due to temperature changes, movement in the fibers, etc.) will introduce additional errors into the data in addition to the phase that was corrected for with the pickoff signal.

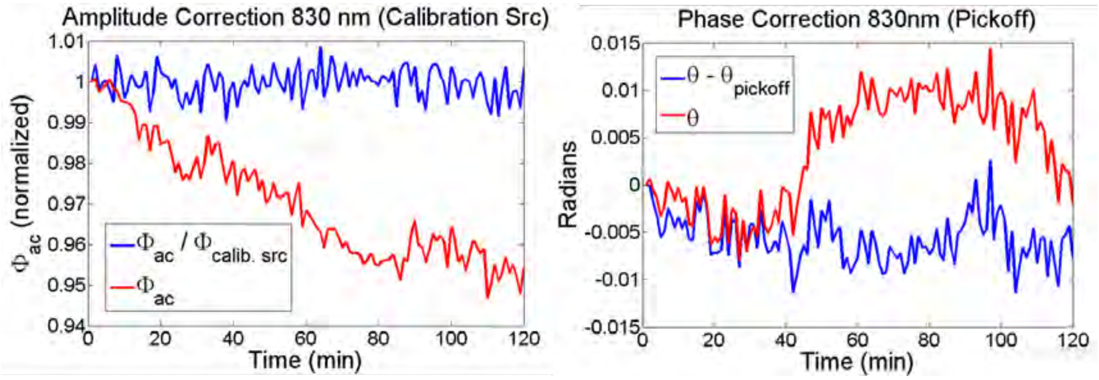

Figure 4.21: Time series data showing value of real-time data normalization methods used for the amplitude (Φ_{ac}, left) and phase (θ, right). The red curve is the uncorrected signal, and blue curve is the corrected curve. The amplitude is corrected using the calibration source and the phase is corrected with the pickoff. This data is with 2×2 pixel binning.

Therefore, in addition to the concurrent reference measurement described in Section 4.4, the Gen3 instrumentation utilizes one additional source for normalization. This additional source channel is obtained after the galvo-switch (it is the light in the 210th channel; its output is placed far from where the breast signals will be measured as shown in Figure 4.15 and Figure 4.19. We refer to this signal as the calibration source. This calibration signal passes through the sample and is taken from another source position fiber; thus, the measurement is not taken concurrently with the other DOT measurements, but rather in series with the DOT measurements. The calibration measurement is typically taken once for every 10 source positions scanned. The advantage of this calibration source is that, unlike the pickoff, the calibration source corrects for changes that might arise due to the galvo or due to the tank and its contents; it is therefore extremely useful for correcting additional relatively-short- and long-term drifts within the system.

Finally, the measurement error σ_Φ and σ_θ of each pixel is calculated by taking the spatial standard deviation of 5×5 pixels centered on that pixel. This was done using the *stdfilt* function in Matlab over the images in Figure 4.20.

4.5 Profilometry

4.5.1 Basics of Profilometry

To further improve our DOT reconstruction quality, we have built two sets of traditional imaging devices based on the fringe projection profilometry technique. A review describing various implementations of this technique can be found in [176]. We do not provide a comprehensive discussion of the methodology here, as it is already worked out. Here we simply implement the techniques proposed by Zhang et. al [177], with its emphasis on speed and reduced dependence on the need for projector gamma calibrations (which are time consuming). The details of this section can be skipped with little cost to the overall understanding of my work.

Figure 4.22 shows a picture of the profilometry device and the corresponding schematic with related coordinate systems for the camera, projector, and the world/object coordinate. The basic steps involved in measuring a 3D surface image with profilometry is the following:

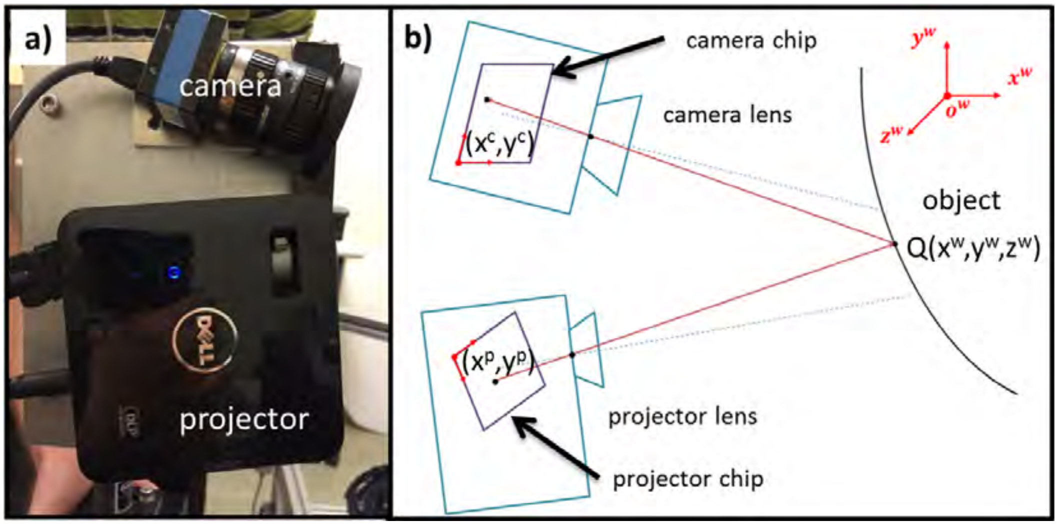

Figure 4.22: a) Profilometry setup consisting of a camera and portable projector. b) Schematic with the coordinate systems for the camera, projector, and the world or object coordinate.

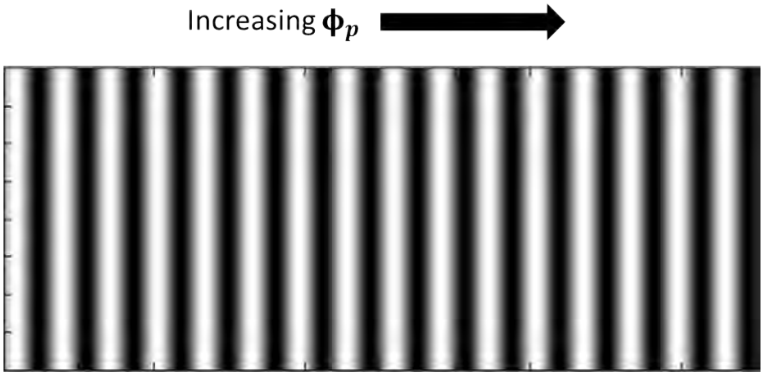

Figure 4.23: Phase map used by the projector based on fringe projection.

1. Project an function, in our case sinusoidal, with increasing phase $\phi_p(x_p)$ along the x-axis of the projector screen onto a flat surface (Figure 4.23).
2. Image phase map with camera at an angle (see Figure 4.22) with an object placed in the phase map projection. The object will distort the phase $\phi_p(x_p)$ recorded on the camera pixel location x_c, y_c. Solve for x_p from $\Phi_p(x_p)$.
3. Convert (x_c, y_c, x_p) to the world spatial coordinate (x_w, y_w, z_w) (calibrations needed) which gives us our surface 3D map.

In practice, a sinusoidal fringe projection (as shown in Figure 4.23) where each column on the projector screen have the same value of $\phi_p(x_p)$. Objects that are moved into the field of view of this phase map will shift the columns of the fringe pattern (note that the shift direction depends on the position of the camera relative to the projector). The magnitude of this shift will contain information in the height of the object as bigger objects will result in bigger shifts in the fringe patterns. Alternatively, the projector can be thought of defining a plane with a particular phase value, while the pixel of the CCD defines a line that intersects the plane from its point-of-view. The place where the line intersect with the plane will define a point in space from which we get our surface information.

Thus one only needs to record the the value of $\phi_p(x_p)$ at a given camera pixel at (x_c, y_c), solve for x_p from $\phi_p(x_p)$ (which is known), then map coordinates (x_c, y_c, x_p) to the world spatial coordinate (x_w, y_w, z_w). Implementing the three steps above for fringe profilometry we have:

Step 1: Project fringe patterns onto the object we (Figure 4.24) (a):

$$\begin{aligned} \phi_p(x_p, y_p) &= 2\pi f_p x_p \; ; & (4.21) \\ P_{p,1}(x_p, y_p) &= \frac{P_{p,max}}{2}\frac{P_{p,max}}{2}\cos(\phi_p(x_p, y_p) - 2\pi/3) \; ; \\ P_{p,2}(x_p, y_p) &= \frac{P_{p,max}}{2}\frac{P_{p,max}}{2}\cos(\phi_p(x_p, y_p)) \; ; \\ P_{p,3}(x_p, y_p) &= \frac{P_{p,max}}{2}\frac{P_{p,max}}{2}\cos(\phi_p(x_p, y_p) + 2\pi/3) \; . & (4.22) \end{aligned}$$

Here P_{max} is the maximum intensity of the projector and $\phi_p(x_p, y_p) = \phi_p(x)$ is the encoded phase on the projector. f_p is the spatial frequency of the fringe and scales with the change in height variation that is expected in the objects we would like to measure and is determined experimentally. Subscript p denotes that we are in the projector coordinates (more on this later). In the above case we made $\phi_p(x_p, y_p) = \phi_p(x)$ such that each column of the projector chip is encoded with one phase value. Three projections are made with offset phase so that we can solve for the phase when we measure the fringe patterns with the camera. Solving Equation 4.21 gives us $x_p = \phi_p/(2\pi f_p)$.

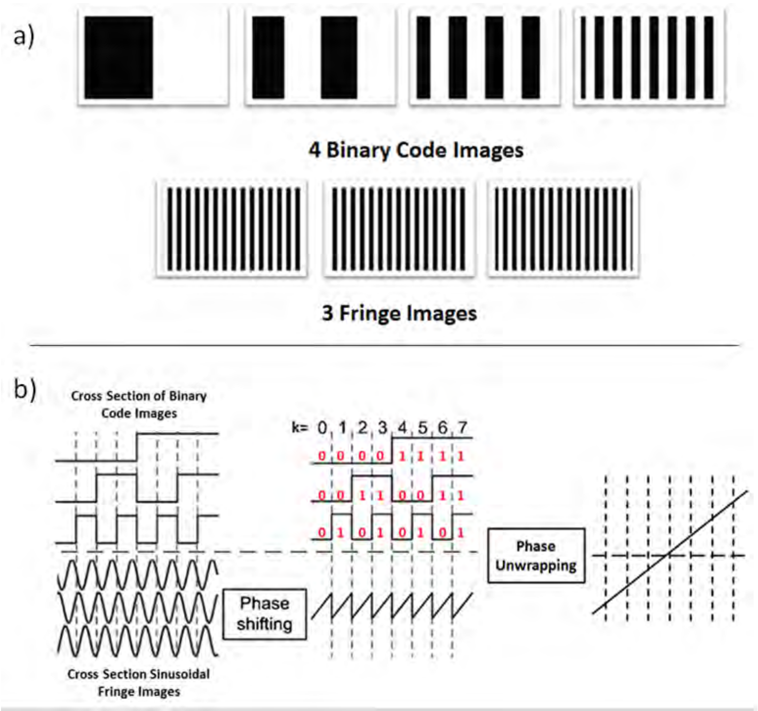

Figure 4.24: a) Binary and fringe projections from the projector. b) Unwrapping scheme proposed by Zhang et al. that uses the binary information encoded by the binary projections.

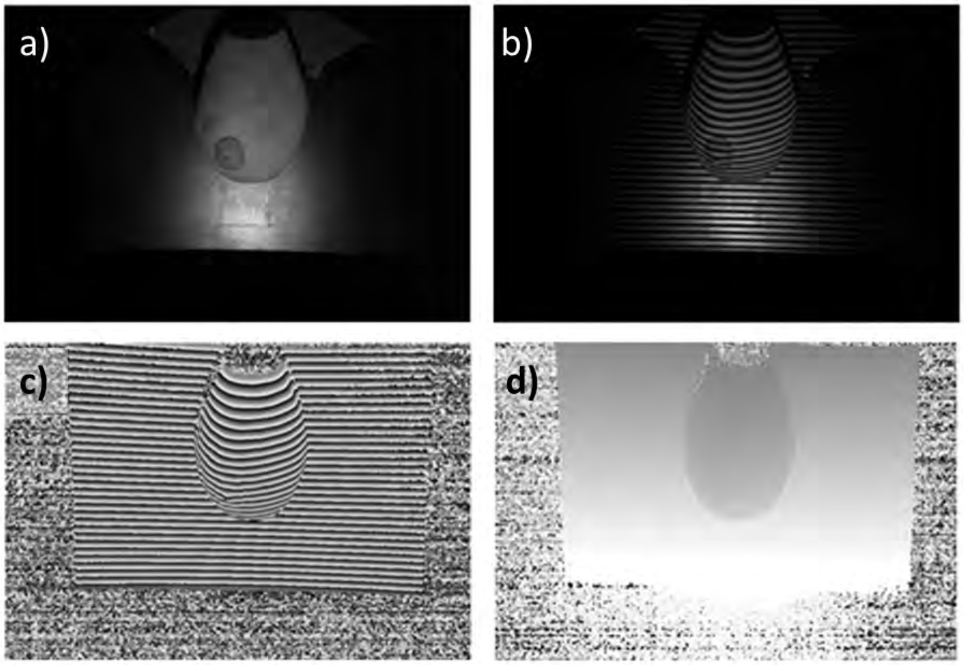

Figure 4.25: a) Object image, b) fringe patterns projected onto object, c) phase image, and d) unwrapped phase image.

Step 2: Measure fringe patterns with camera and solve for the distorted phase due to the object.

$$\begin{aligned}
M_{c,1}(x_c, y_c) &= M_{c,dc}(x_c, y_c) + M_{c,ac}(x_c, y_c)\cos(\phi_c(x_c, y_c) - 2\pi/3) \\
M_{c,2}(x_c, y_c) &= M_{c,dc}(x_c, y_c) + M_{c,ac}(x_c, y_c)\cos(\phi_c(x_c, y_c)) \\
M_{c,3}(x_c, y_c) &= M_{c,dc}(x_c, y_c) + M_{c,ac}(x_c, y_c)\cos(\phi_c(x_c, y_c) + 2\pi/3) \qquad (4.23) \\
\phi_c(x_c, y_c) &= \arctan\big(\frac{\sqrt{3}(P_{c,1}(x_c, y_c) - P_{c,3}(x_c, y_c)}{2P_{c,2}(x_c, y_c) - P_{c,3}(x_c, y_c)}\big)\Bigg(\qquad (4.24)
\end{aligned}$$

where $M_{c,dc}$ is the measured average intensity, $P_{c,dc}$ is the modulation amplitude and ϕ_c is the phase value we want to solve for. The subscript c denotes the camera reference. Equation 4.24 can be used to solve for ϕ_c. Fortunately, since we chose to increase the phase map along one axis, aligning the camera and projector parallel to this axis allow the approximation that $\phi_c = \phi_p$. Before we can solve for our surface map, we need to unwrap as sinusoidal projections repeat in phase over $[-\pi, \pi]$:

$$\Phi_c(x_c, y_c) = \phi_c(x_c, y_c) + 2\pi \cdot k(x_c, y_c) \qquad (4.25)$$

Here k is called the fringe number. The value of k cannot be solved without additional information. The value of k can be encoded into our camera by projecting an additional set of images to encode binary information spatially [177]. A schematic diagram of the projections used and the binary encoding method is shown in Figure 4.24(a). Using a set of four binary code images encode each camera pixel with 4-bit information corresponding to a value of k. An example is shown in Figure 4.24(b) for a 3-bit case. Implementing these steps, we are able to unwrap the phase as shown in Figure 4.25(b).

Step 3: Convert $(x_c, y_c, x_p) \rightarrow (x_w, y_w, z_w)$ At this point we have x_c, y_c, and x_p. We can convert these values to a point in space with the following equations:

$$\begin{aligned}
x_c &= P_{c,11}x_w + P_{c,12}y_w + P_{c,13}z_w + P_{c,14}\ ; \\
y_c &= P_{c,21}x_w + P_{c,22}y_w + P_{c,23}z_w + P_{c,24}\ ; \\
x_p &= P_{p,11}x_w + P_{p,12}y_w + P_{p,13}z_w + P_{p,14}\ ,
\end{aligned} \tag{4.26}$$

where $P_c = A_{i,c}[R_c, t_c]$ and $P_p = A_{i,p}[R_p, t_p]$ where A_i is the intrinsic parameter matrix (which take into account the focal length and skew), R is the rotational matrix, and t is the translational matrix. Solving Equation 4.26 gives us (x_w, y_w, z_w) for every (x_c, y_c, x_p) which, in turn, give our 3D surface map! I will not go into details of the calibration method to find the values of A_i, R, and t for the camera and projector, but I refer interested reader to [176, 178–180].

4.5.2 Profilometry Setup and Breast Shape Measurement

The profilometry setup used in the Gen3 system is shown in Figure 4.22(a). The setup consists of a projector (M110, Dell) and a small CMOS camera (DMK 72AUC02, The Imaging Source) with a $5\ \mathrm{mm}$ lens (H0514-MP2, The Imaging Source) mounted on a custom aluminum block. Once the projector and camera positions are fixed relative to each other, the coordinate and height calibrations are made. Two profilometry setups are used in the Gen3 system and mounted on the sides of the imaging tank as shown in Figure 4.26.

After the breast is inserted into the imaging tank, profilometry images are taken from the sides. Figure 4.28 shows data from a human subject. In most cases, the area covered by the two profilometry sets is not large enough to obtain a 3D surface image of the whole breast. Thus, the bottom side of the breast must be generated with a 3D surface fit based on data in Figure 4.28(a)

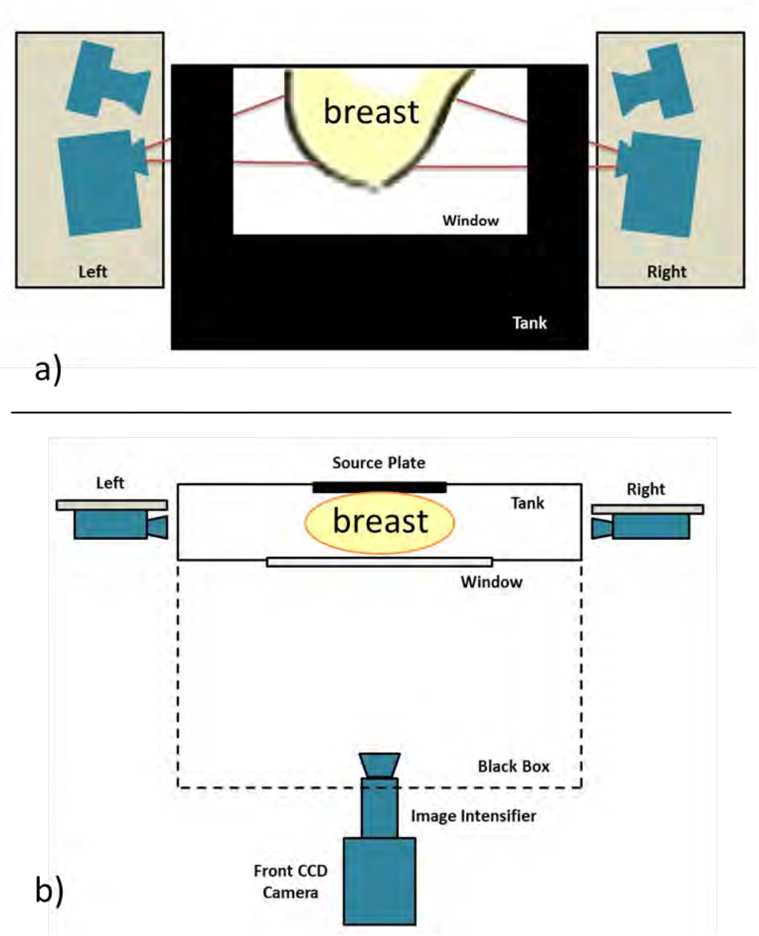

Figure 4.26: a) Front view of profilometry system from Gen3 CCD perspective b) top view.

Figure 4.27: Photograph of the profilometry positioning calibration target use to map the images from the profilometry sets and the Gen3 CCD onto the same space. The white plate, with three holes, hangs down in the tank and is used to align the rotational and translational position of the profilometry 3D surface images relative to one another.

and (b). To improve the accuracy of this bottom surface fit, a sagittal image from the CCD is acquired in addition to the profilometry data (see Figure 4.28(c)). The saggital image is used to determine outer edge of the breast shown by a red line, which, in turn, is used to aid the bottom surface fit.

The relative positions of the two profilometry surfaces are linked together with one additional measurement obtained using a positioning calibration target shown in Figure 4.27. The three holes in the target helps with the profilometry sets, i.e., helps to align their position and rotation relative to each other. The target is designed to always fit into the tank in the same position; this feature helps us match the profilometry sets to the Gen3 CCD (and the red line from the sagittal image).

To generate the 3D surface image, the two surface point clouds generated by the profilometry sets are combined with the outer trace (red line) of the breast image from the CCD to derive the surface on the bottom side of the breast that was not illuminated by the profilometry projectors. The resulting 3D surface fit is then used to generate a tetrahedral volume mesh to be used in the DOT image reconstruction.

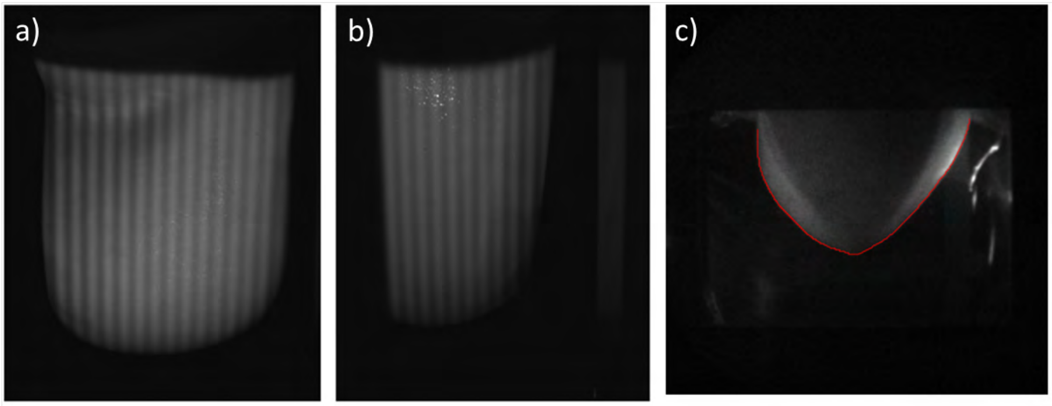

Figure 4.28: a) Fringe pattern projected on the breast (left side of tank), b) fringe pattern on right side of tank, and c) sagittal view of breast from front CCD. Red line shows outer edge of breast traced by hand.

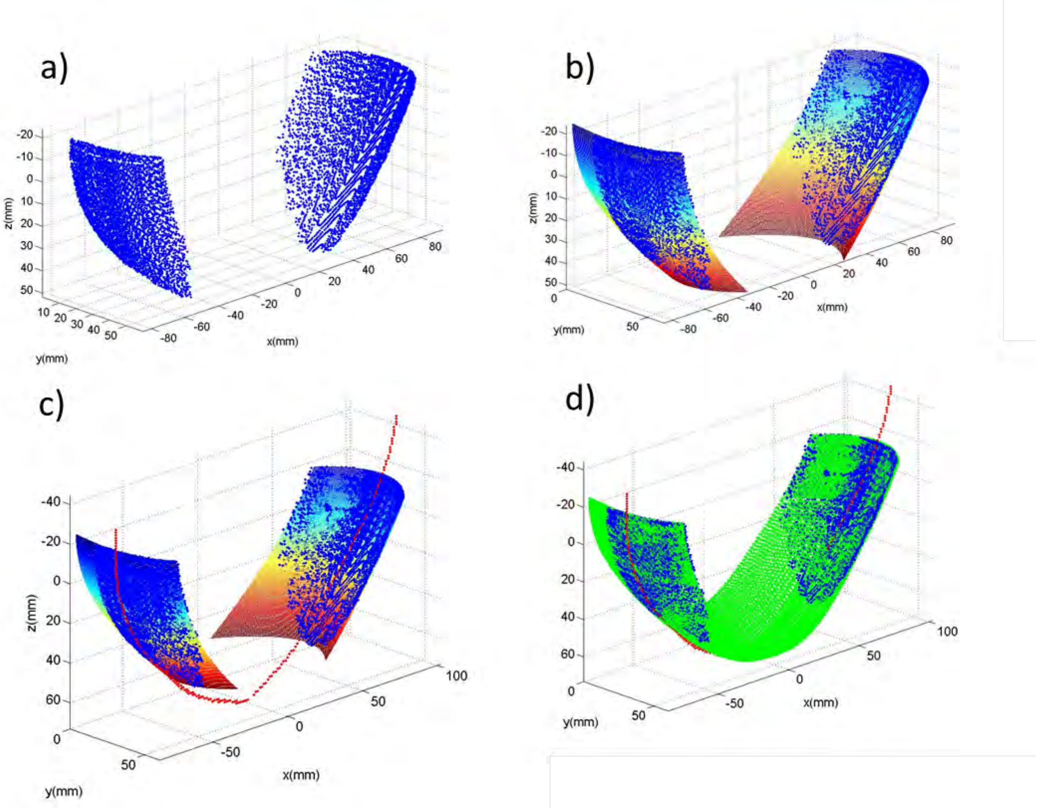

Figure 4.29: a) 3D point cloud generated by fringe profilometry b) surface fit of 3D point cloud c) line trace (red) from front CCD camera scaled and translated to match side surfaces d) 3D surface fit of whole breast generated from fringe profilometry data and front image trace.

4.6 Clinical Software

The software for the Gen3 device was written in Labview. Two sets of software were written to run measurements on the Gen3 device. The Experimental Software permits an advanced user to fully control the Gen3 device hardware settings and measurement sequences. This Experimental Software is also used to generate a configuration file used in experiments where various CCD settings can be set and saved for use on the Clinical Panel.

The Clinical Software was written with our clinical coordinators in mind (see Figs. 6.1). Five modules in sequence take the user from tasks that organize the output files to tasks that choose the source and wavelength configuration, tasks that optimize the detection gain and output light levels, and finally to screens that allow the user to start the measurement sequence and see its progress. For detailed description of the software I refer the user to Appendix A.

4.7 Instrument Characterization

4.7.1 Spectroscopy

Although the data used in DOT reconstructions are normalized to measure relative changes in optical properties (see Section 4.4), one way to test the imaging system is to compare a measurements that extract absolute values of μ_a and μ_s' in a Intralipid solution to slab theory predictions. In particular, this scheme enable us to evaluate the data quality of the frequency-Domain (FD) detection capabilities of the Gen3 imager. Figure 4.30 shows data from the FD transmission data that has been preprocessed; comparison to a slab solution model is also shown. The light was from a source near the center of the detection lens. Figure 4.30 shows the slab solution fit for

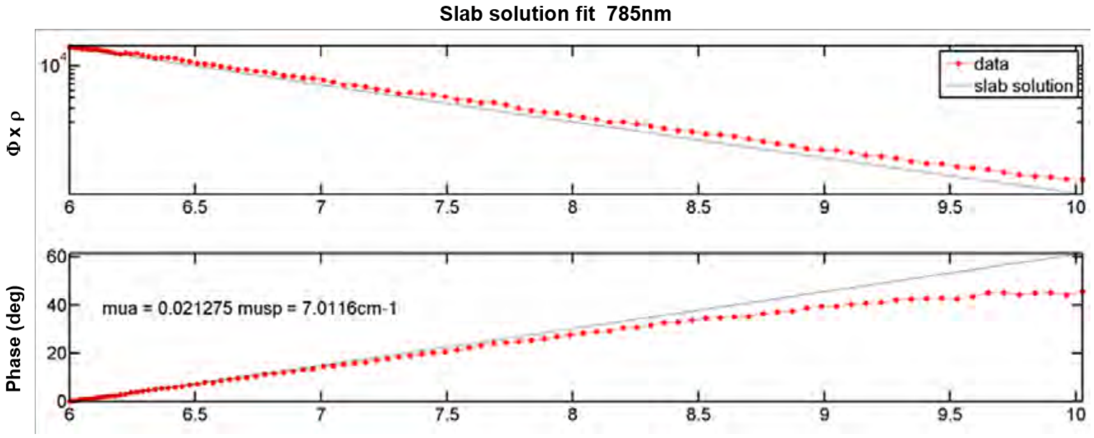

Figure 4.30: Comparison of $\ln(\Phi_{ac} \times \rho)$ and Phase (θ) vs ρ of the Gen3 data from a line of pixels and the analytical slab solution fit to the data for μ_a and μ_s'. Expected values were $\mu_a = 0.021cm^{-1}$ and $\mu_s' = 8cm^{-1}$

μ_a and μ_s' of a homogeneous Intralipid solution; the results exhibit reasonable agreement with expected values.

In general, determination of the absolute value of μ_a and μ_s' in this way cannot take advantage of all source locations, e.g., due to vignetting and barreling that occurs when light travels too far from the center of the detection lens. However, when normalized with a reference measurement as described in Section 4.4, then optical property changes can be measured using all source-detector pairs. This is because one can account for the pathologies associated with each source-detector.

To get a sense of these deviations in the data (in absolute terms), in Figure 4.31 and 4.32 we plot the preprocessed data from all the detectors (CCD pixels) for every source and every wavelength. The two data sets are derived from tissue phantom (red: two target–see next section) and a Intralipid reference measurements (blue), respectively. This particular dataset should overlap as the only differences in the measurement are due to two small perturbations. Figure 4.33 shows plots the normalized amplitude, Φ_{target}/Φ_{ref}, and the phase shift $\Delta\theta = \theta_{target} - \theta_{ref}$ for 660

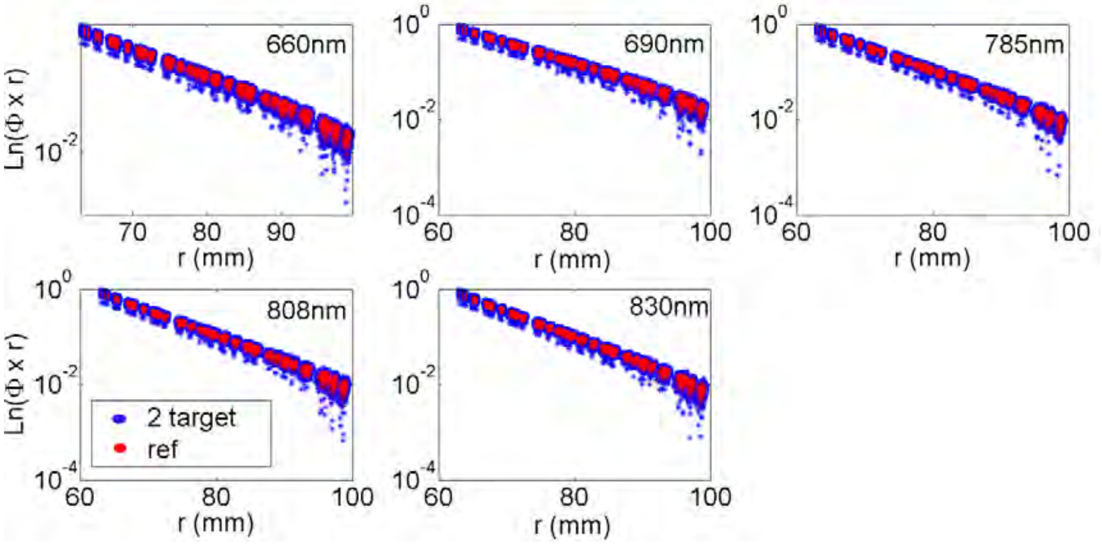

Figure 4.31: $\ln(\Phi_{ac} \times r)$ vs r plot for all 209 sources at all 5 wavelengths. The tank thickness is 63 mm. Usually, the data usage is cut off around $r = 85$ mm where noise starts to become significant. Repeatability between target and reference data (blue vs red) as well as linearity vs r provide criteria by which we can judge data quality.

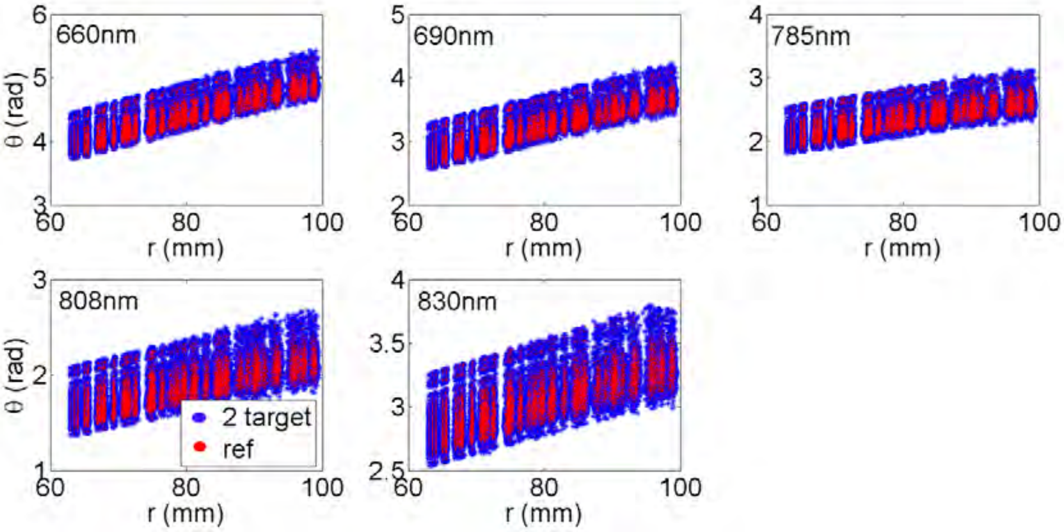

Figure 4.32: θ_{ac} vs r plot for the same data set in Figure 4.31. The distribution of values for $\theta(63\ \mathrm{mm})$ is due (in part) to variations of the source fiber length, i.e., since the fibers were assembled by hand (see Section 4.3.3)

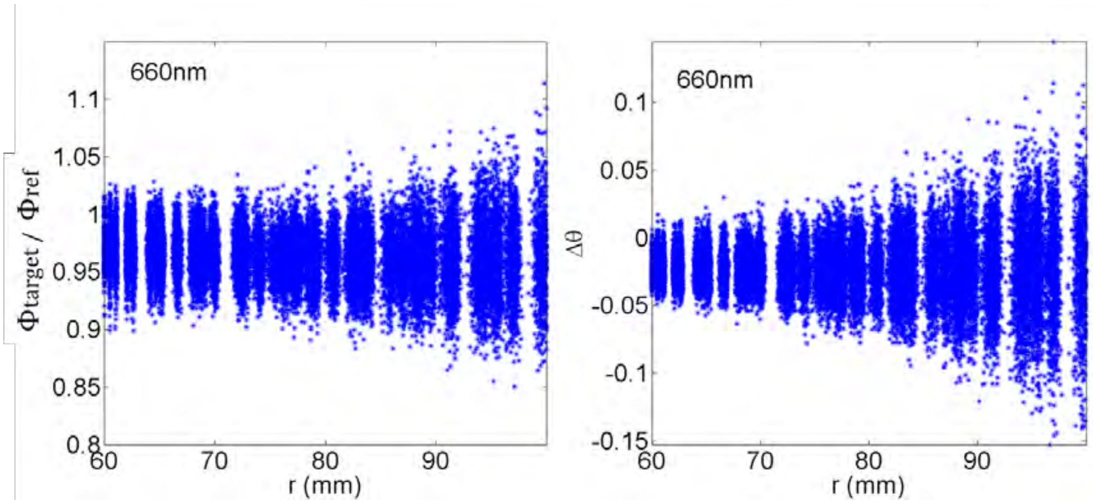

Figure 4.33: Plot of Φ_{target}/Φ_{ref} (left) where the two target scan in Figure 4.31 is divided by the reference scan (normalized) for each source detector pair. $\Delta\theta = \theta_{target} - \theta_{ref}$ (right, radians) where the two target scan in Figure 4.32 for the two target and reference measurements (at 660 nm) for all source detector pairs. The width of the differences is used to derive a criteria for how large a source-detector separation ($\sim$ $80mm$) we should use before noise becomes important.

nm. Thus the quality of the reference normalization can be determined the general agreement in the data points. The SNR of the signal also determines how large r can be before the fluence rate ($\ln(\Phi_{ac} \times r)$) and θ begin to lose linearity (e.g., around 85 mm).

4.7.2 Targets for Imaging Experiments

The frequency-domain capabilities of the Gen3 imager make it easier to reconstruct both absorption and scattering contrast properties. This capability was relatively weak in the Gen2 system. As a result we developed new kinds of targets appropriate for frequency domain experiments. The targets we use are typically hollow containers filled with contrast media for imaging. Our old targets were made from translucent cylinder plastic containers (1.5 cm in diameter and 1.5 cm in height) connected to thin Tygon tubing for loading contrast media. For these targets, the

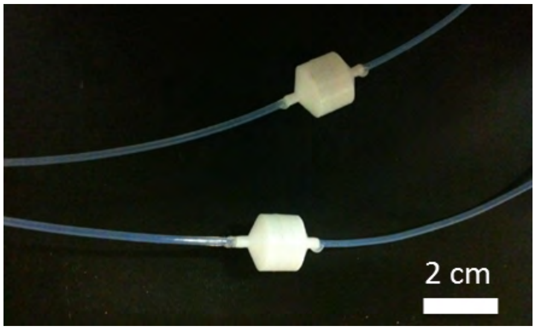

Figure 4.34: Photograph of custom targets used for imaging liquid phantoms. The targets are made of white delrin with 16 mm diameter and 1 mm thick walls. The targets are attached to a thin nylon tubing and sealed with silicone gel. The targets are hung vertically and shaped so that air bubbles freely escape.

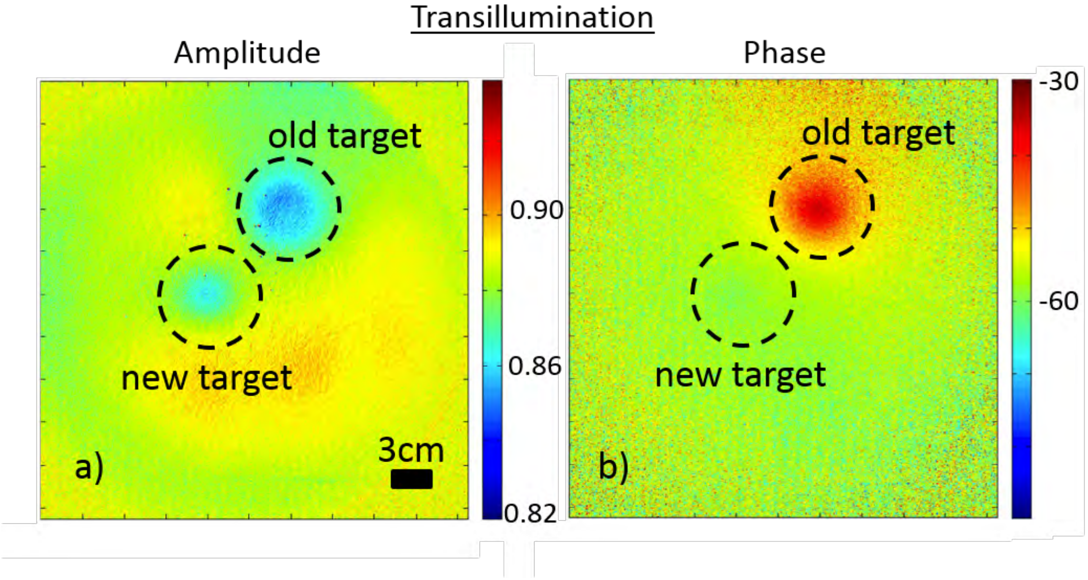

Figure 4.35: a) Transillumination images of Delrin target (bottom left) and a typical translucent plastic target. White delrin is a good choice as it has scattering and absorption properties similar to Intralipid. (left) Transillumination amplitude data of Intralipid filled targets in the background fluid (normalized intensity). (Right) Transillumination phase data (degrees).

perturbation to absorption was low (Figure 4.35(b), but the target material contributed significant phase contrast (Figure 4.35(c). In fact, we can more readily detect these phase contrast signals with the new (Gen3) frequency domain system. Several translucent or white materials were tested with the transillumination experiment shown in Figure 4.35. Targets filled with the background Intralipid ($\mu_a = 0.041cm^{-1}$, $\mu_s' = 8cm^{-1}$) were suspended inside the reference solution in a tank (the same tank used in Chapter 3) and the amplitude and phase data were collected. Importantly, we found that white Delrin with thin PTFE tubing (microbore, Cole Palmer) introduced the lowest amplitude and phase contrast artifacts (Figure 4.34).

4.8 Simulations

The data from the Gen3 imager was reconstructed using a software suite called TOAST++ (Time-resolved Optical Absorption Scattering Tomography) [146]. TOAST employs FEM for the forward problem and Newton-type (Gauss-Newton, Levenberg-Marquardt, etc.) or gradient-type (Conjugate Gradient) methods for the inverse problem. Simulation results based on the Gen3 imager configuration (and related to actual experiments performed with the Gen3 imager) are presented in this section.

Simulations are valuable. They permit testing of constraints for the geometry, source-detector pair arrangement, and data type of a particular imaging system (e.g., Gen3). Furthermore, limitations of the reconstruction method can be tested, and control parameters (e.g., regularization parameters) can be adjusted with repeated reconstructions to reduce and optimize the parameter space for ultimate experiments with real data.

4.8.1 2D Reconstructions of Simulated Data

We carried out a set of simulated 2D reconstructions on noiseless data. These test-studies enabled us to confirm that we obtain expected results in situations wherein all aspects of the problem are fully under control and the target medium is fully understood. Although significant differences

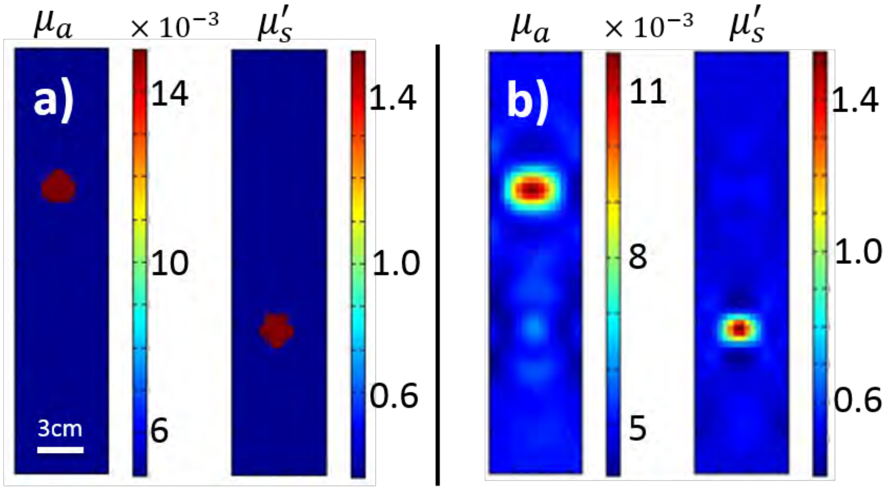

Figure 4.36: Simultaneous 2D reconstruction of μ_a and μ_s' with 3:1 contrast targets for both based on simulated data. a) Exact image of the target absorption $\mu_a = 0.015\ \mathrm{mm}^{-1}$ (left) and scattering $\mu_s' = 1.5\ \mathrm{mm}^{-1}$ (right) with target background $\mu_a = 0.005\ \mathrm{mm}^{-1},\ \mu_s' = 0.5\ \mathrm{mm}^{-1}$ b) Gauss-Newton reconstruction of $\mu_a,\ \mu_s'$ from forward data obtained with this simulated phantom with uniform regularization and scaling of both scattering and absorption heterogeneities to their average/background.

can arise between 2D and 3D data, as well as for reconstructing with and without noise, the 2D simulations we carry out significantly reduce the scale of the problem and enable us to explore limitations of the reconstruction methods within a short period of time (i.e., on the order of minutes per reconstruction in 2D, rather than hours in 3D).

Figure 4.36 shows the target medium from which simulated data was generated, as well as the 2D reconstruction of the absorption and scattering targets. The reconstructed area is a 80×20 pixel (3 mm/pixel) with μ_a and μ_s' inclusions that are 1.8 cm in diameter (Figure 4.36(a)). The first column shows the true absorption contrast in the target medium and the second column shows the true scattering contrast in the target medium. The reconstruction of these inclusions is shown in Figure 4.36(b).

Notice that the reconstructed absorption target in the simulation is larger than the scattering target by about a factor of $\sim 50\%$. Further, the scattering target is close to the same size as the test inclusion, but the absorption target is not. Also, a very small amount of crosstalk is evident wherein the scattering inclusion shows up in the absorption reconstruction. We can partially understand the size discrepancy between the absorption and scattering inclusions by considering the sensitivity plots shown in Figure 4.37. The sensitivity plots show the spatial sensitivity of the measured amplitude (Φ_{ac}) and phase (θ) data with respect to μ_a and μ_s' for a particular source-detector pair. The plots in Figure 4.37 show that μ_a sensitivity spans over a larger spatial area compared to scattering; this observation helps to explain the larger size of the absorbing target in the reconstruction. Conversely, the μ_s' sensitivity is spatially smaller and more localized than absorption, which presumably helps to produce a more spatially defined target (i.e., compared to absorption) in the reconstructions. We will return to describe a regularization strategy that can cope with this observation of asymmetry between absorption and scattering reconstruction.

Before moving to the regularization strategies and tests, I describe one more technical effect that we noticed about these systems from the simulations. This effect concerns the trade-off between resolution/contrast and field-of-view angle. In our experimental data, for the typical image slabs, the transverse distance that we can access above the noise level is approximately $8.5\ \mathrm{cm}$. This transverse distance (and the slab separation) defines a maximum field-of-view angle for the data set. In the simulation studies, since we have no noise, we were able to carry out reconstructions for different transverse distances (at fixed slab thickness) and compare the reconstructions. Figure 4.38 shows reconstructions wherein the transverse distance is set to be a)$\mathbf{r} = 8$ and b) $\mathbf{r} = 10\ \mathrm{cm}$. As expected the larger $\mathbf{r}$ improves our resolution overall, but mostly

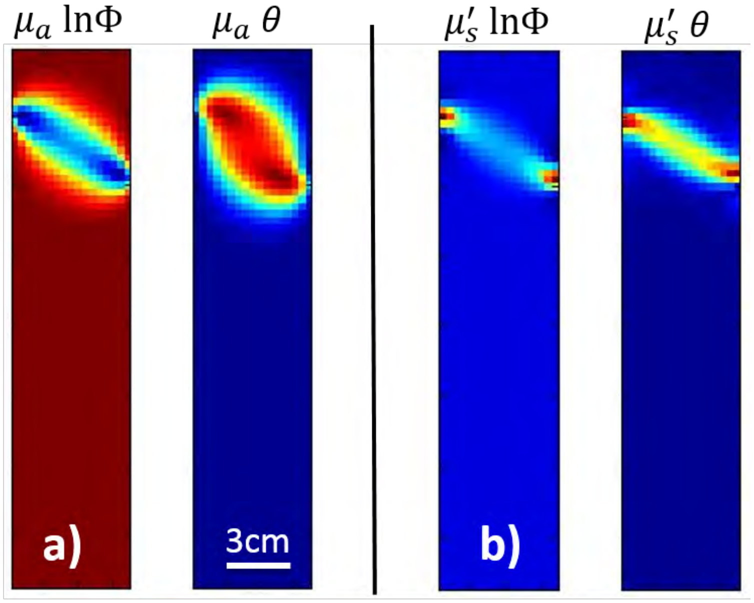

Figure 4.37: Plot of the sensitivity regions (Jacobian) for a source-detector pair. a) The two images are the sensitivity of $\ln \Phi_{ac}$ and θ to changes in μ_a; b) the two images are the sensitivity of $\ln \Phi_{ac}$ and θ to changes in μ_s'. Notice, $\ln \Phi_{ac}$ and θ have a broader area of sensitivity to changes in the absorption compared to changes in scattering.

the improvements occur for the absorption heterogeneity. Therefore, this small but focused 2D simulation investigation informs us that substantial resolution gains can be made with our apparatus, if the signal-to-noise ratio (SNR) of our system can be improved, i.e., if we can make collect data at larger source-detector separations.

We now return to the regularization issue. To our knowledge, researchers in the DOT community have treated absorption and scattering on the same footing. However, we have shown that the absorption target reconstruction is worse than the scattering target reconstruction (i.e., with sensitivity curves and with the reconstructions of simulated data). This observation suggests that it might be better to apply separate regularization for each of these parameters. We explored this approach using Total Variation (TV) regularization, which is largely oriented towards the

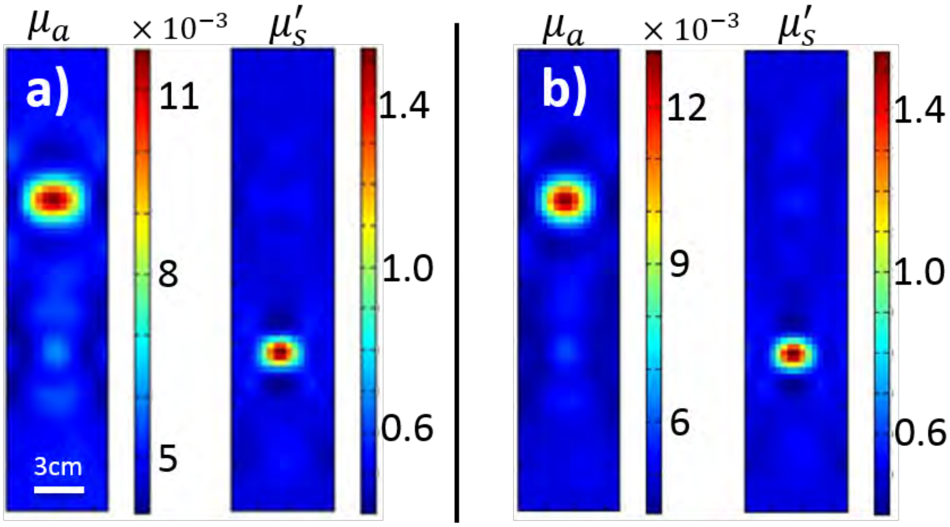

Figure 4.38: a) Same reconstruction as Figure 4.36(b) where the maximum transverse distance (along the detection plane) for data taking is $\mathbf{r} = 8$ cm. b) Reconstruction with maximum transverse distance set to $\mathbf{r} = 10$ cm. Larger $\mathbf{r}$ produces better resolution in the reconstruction.

spatial gradient of the optical properties and thus has the effect of conserving edge shapes. Total Variation (TV) regularization was used here, because we found it to have an improved effect on the resolution of the reconstructions of simulated data. Figure 4.39 shows the TV regularization applied to our previous reconstruction with various hyperparameters and the TV parameter β (see Section 2.2.2.6 in Chapter 2). By varying the parameters and then carrying out a corresponding reconstruction, it was determined that the parameters $\Lambda = 1 \times 10^{-4}$, $\beta = 1 \times 10^{-3}$ for μ_a, and $\Lambda = 1 \times 10^{-3}$, $\beta = 1 \times 10^{-2}$ for μ_s', gave the best fidelity for absorption at the cost of some scattering contrast. This choice of regularization also brought the size of the reconstructed absorption and scattering targets into the same range, which is also an improvement.

Therefore, from our 2D reconstructions we learned that it can be useful to separately regularize absorption and scattering, and that it is important to optimize this regularization combination.

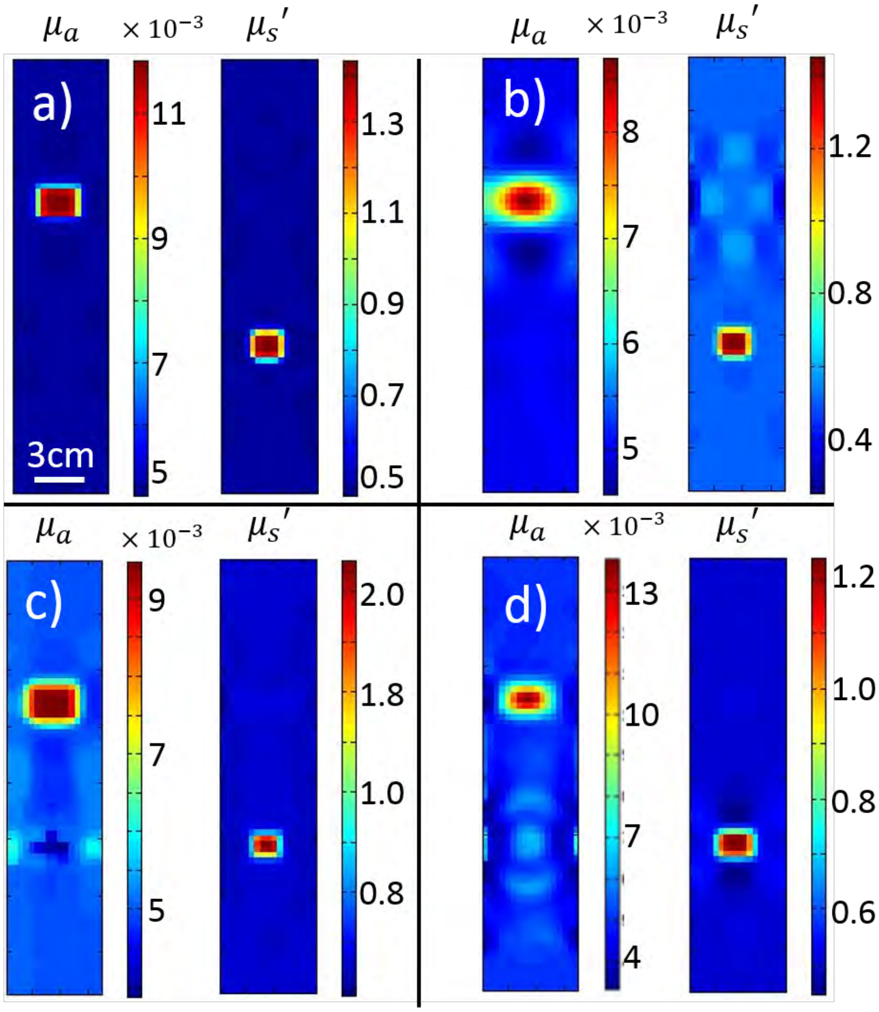

Figure 4.39: 2D reconstructions for inclusions in Figure 4.36(a) but with Total Variation (TV) regularization. Values for Λ the hyperparameter and β the TV parameter for μ_a are varied separately. μ_s': $\Lambda = 1 \times 10^{-3}$, $\beta = 1 \times 10^{-2}$ for all images. μ_a: a) $\Lambda = 1 \times 10^{-2}$, $\beta = 1 \times 10^{-3}$; b) $\Lambda = 1 \times 10^{-3}$, $\beta = 1 \times 10^{-1}$; c) $\Lambda = 1 \times 10^{-2}$, $\beta = 1 \times 10^{-3}$; d) $\Lambda = 1 \times 10^{-4}$, $\beta = 1 \times 10^{-3}$.

Without this scheme, the reconstructed absorption spatial resolution (and contrast) is considerably worse than that of scattering. This effect was rationalized with the sensitivity curves, and an effort was made to find the independent regularization parameters for which the reconstructed μ_a and μ_s' resolution was about the same. We will use these values, i.e., from 2D, in most of the other reconstructions (both simulations and experiment); ultimately, we will want to carry out a more comprehensive investigation of the independent regularization parameters for 3D simulated data and experimental reconstructions. Note, we also tried other regularization schemes (e.g., Tikhonov, PM), but we found that Total Variation (TV) regularization worked best, at least in the 2D simulations. Unfortunately, these additional degrees of freedom in regularization open up a great deal more phase-space for reconstruction optimization. On the other hand, and perhaps most importantly, we have discovered an important new avenue for image improvement!

4.8.2 3D Reconstructions of Simulated Data

Having explored different regularization schemes and parameter values in 2D simulations, we next moved to consider 3D simulations. Figure 4.40 is a 3D reconstruction of two targets with the same diameter as in the 2D reconstructions and located in 3D within a 60 mm thick slab. The top slices are closer to the source plane, and the lower slices are closer to the detector plane. The center slice at 30 mm is shown. The sub-figures a) and b) are 3D reconstructions with uniform versus independent TV regularization. Figure 4.40(b) employs separate regularization for μ_a, μ_s', and we again see that the absorption spatial resolution and contrast improve. The gains exhibited in 3D thus appear to parallel our 2D results, and they reaffirm our expectation that improvements in 2D reconstructions translate to the 3D case. Of course, more work needs to be done to test whether the optimal regularization parameters are the same for 2D and 3D, but these initial results are encouraging.

Figure 4.44 shows the simulated 3D reconstruction of two targets with a $3\times$ absorption (with spectrum corresponding to the dye IR806, upper left) and a $3\times$ scattering (corresponding to Intralipid, lower right) contrast. (Here we use targets in the simulations which are somewhat

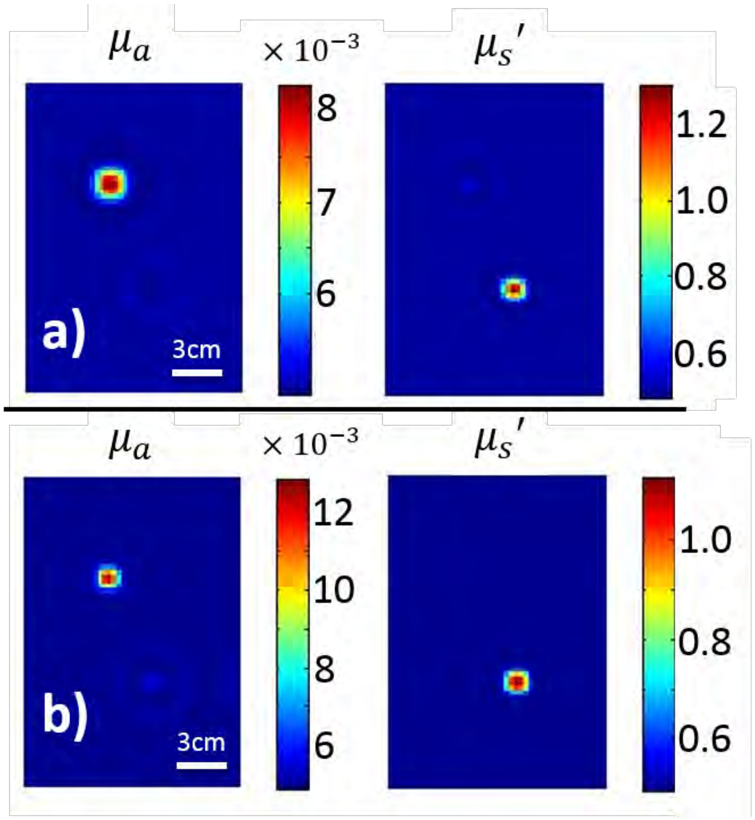

Figure 4.40: Simulated 3D reconstruction with TV regularization. a) μ_a, μ_s': $\Lambda = 1 \times 10^{-4}$, $\beta = 1 \times 10^{-2}$, b) μ_a: $\Lambda = 1 \times 10^{-4}$, $\beta = 1 \times 10^{-2}$, μ_s': $\Lambda = 1 \times 10^{-3}$, $\beta = 1 \times 10^{-2}$

close to those in our 3D tissue phantom experiments.) For these reconstructions, the conjugate-gradient method was used with TV regularization. A CW reconstruction where only amplitude (Φ_{DC}) information is used, and a FD reconstruction where both amplitude (Φ_{ac}) and phase (θ) data is used, are both shown in the figure. Slices are shown at 10 mm intervals and are parallel to the source and detector planes. The slices stretch from the source plane (top) to the detector plane (bottom). The simulations clearly show, as expected, that without FD data (i.e., without amplitude and phase information), decoupling of μ_a and μ_s' is poor. With FD data, importantly, most of this cross-talk is eliminated. Interestingly, even with noiseless data there is still some

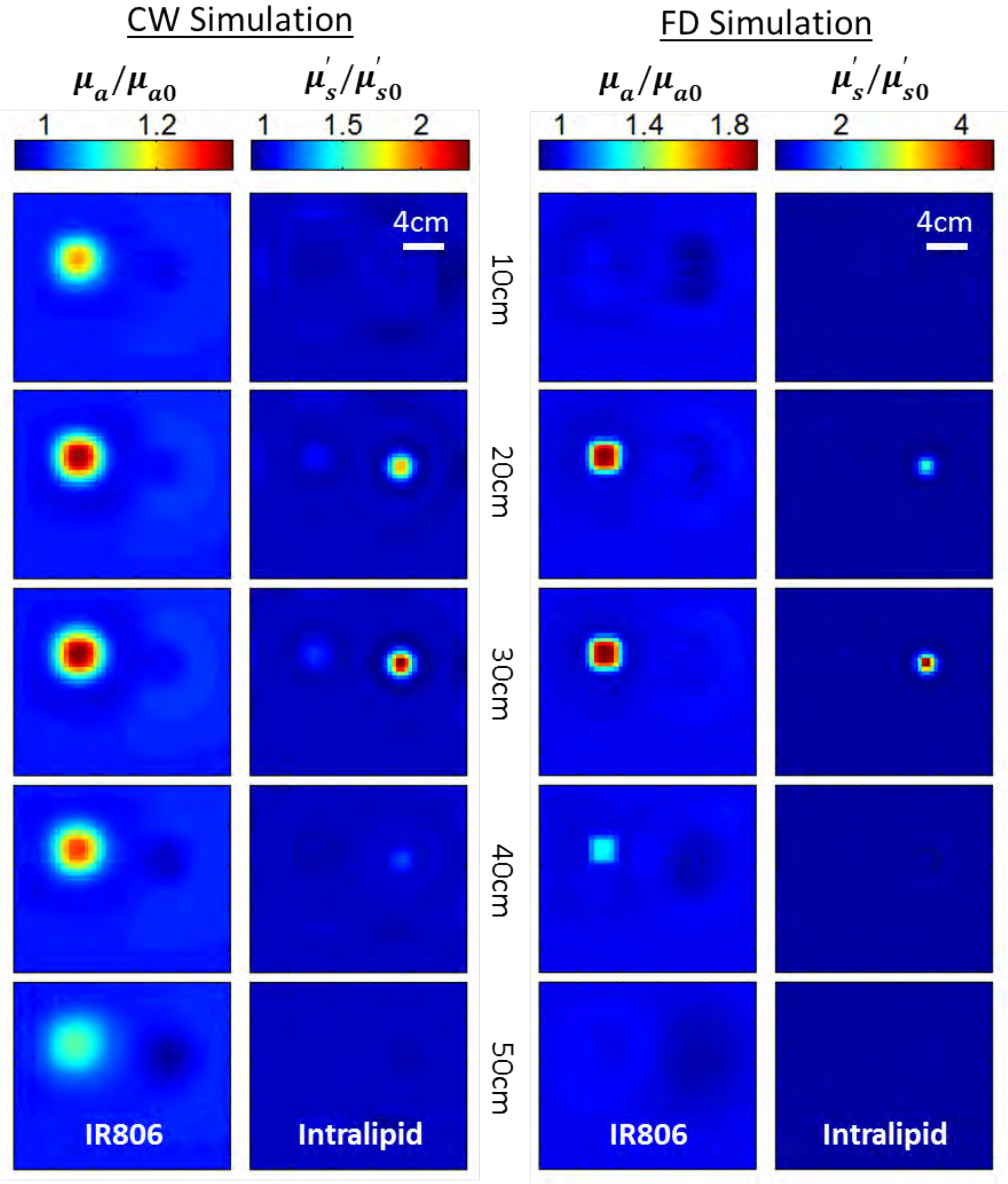

Figure 4.41: Simulation 3D reconstructions of an absorption target (top left) and scattering target (bottom right) with continuous-wave and frequency-domain data using TV regularization. The simulation shows that most of the crosstalk between absorption and scattering is mitigated with FD. The FD reconstruction of μ_a shows a 40% contrast (($0.15\ \mathrm{cm}^{-1}$ expected) with a 10% crosstalk from μ_s'. The FD reconstruction of μ_s' shows a 60% contrast ($15\ \mathrm{cm}^{-1}$ expected) at the scattering target with minimal crosstalk from the absorption target. Top slices are closer to the source plane and the lower slices are closer to the detector plane.

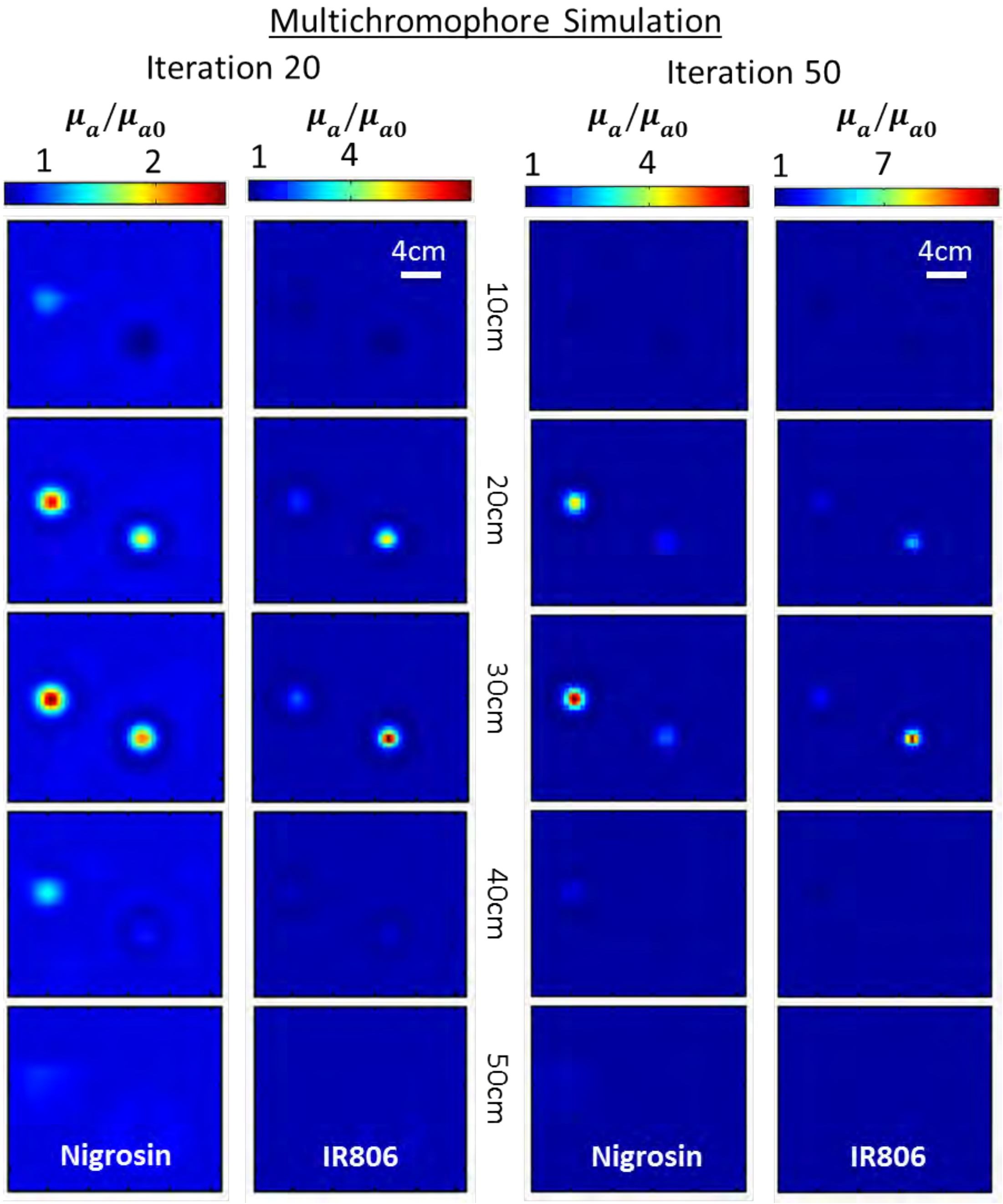

Figure 4.42: Simulated 3D reconstruction of the two targets with different chromophores as shown in Figure 4.43(b). The upper left target is filled with a Nigrosin contrast, and the bottom right target is filled with IR806 contrast. Each has an expected absorption that is twice the background Intralipid. The left columns show an early iteration wherein there is still crosstalk in the chromophores, but reasonable contrast. At late iterations the crosstalk is diminished, but the contrast is very high and the inclusion size small.

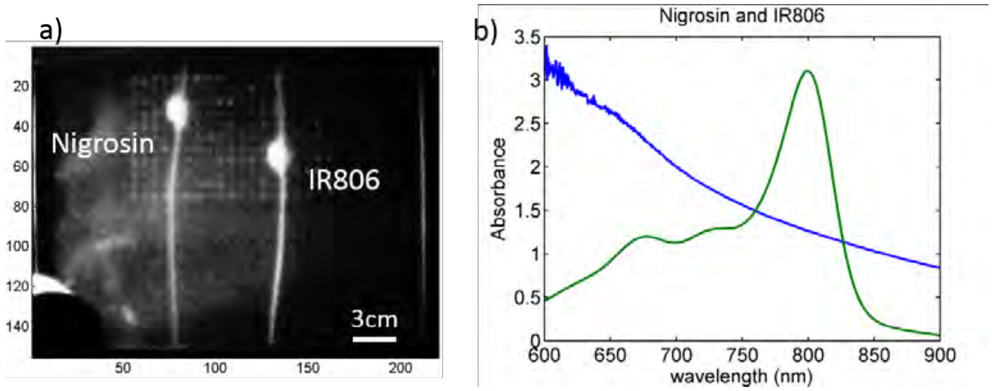

Figure 4.43: a) Photograph of the two targets used in the multi-chromophore experiment; the images was taken by the Gen3 CCD. b) Spectra of the Nigrosin (blue) and IR806 (green) chromophores that were used in the multi-chromophore simulation and experiment.

crosstalk from μ_s' to μ_a (10% in this case) for our particular source-detector arrangement and geometry. Although the target medium inclusions are exactly in the slab center for both μ_a and μ_s', there also seems to be a tendency for the reconstructed targets to be closer to the source plate. This shift might be caused by the sparse number of sources compared to the large number of detectors; in these simulations we have used just 60 sources (selected symmetrically out of the 209 total sources) and 209 detectors to speed up our reconstructions for our analysis. This type of issue is something that we intend to explore more with further reconstructions.

Finally, we also ran a simulation of two target inclusions with different chromophores (but the same scattering); this reconstruction can in principle utilize spectral information. The contrast of the two dyes, Nigrosin and IR806, was again utilized to roughly match one of our tissue phantom experiments for which the spectral information is known (see Figure 4.43). The simulation, in this case, shows how we can separate the two chromophores based on their spectral information. In the clinical case, of course, it is desirable to differentiate the chromophore concentrations of oxy- and deoxy-hemoglobin in tissue. Figure 4.42 shows the results at different iterations of the multi-chromophore reconstruction. Notice that at iteration 20, the reconstructed inclusions attain realistic values of the chromophore contrasts but there is still some crosstalk. At iteration 50, the chromophores are clearly differentiated spatially, but the contrast overshoots the expected values. Again, more work is needed to clarify these observations and derive approaches to minimize the problems that surely could arise in real experiments.

4.9 Tissue Phantoms

After our work with simulations, we tested the Gen3 imager and reconstruction schemes with tissue phantoms that roughly mimic optical the properties and contrast of breast tissue. Hollow targets, $16\ \mathrm{mm}$ in diameter (Figure 4.34) with $1\ \mathrm{mm}$ thick walls, were filled with optical contrast and submerged in a background solution.

Figure 4.44 shows the reconstruction using data from our Gen3 imager with the tissue phantoms. The background solution was mixed with India ink and Intralipid to have an approximate absorption and scattering of $\mu_a = 0.05\ \mathrm{cm}^{-1}$ and $\mu_s' = 5\ \mathrm{cm}^{-1}$ at $785\ \mathrm{nm}$. The targets were filled to have $3\times$ chromophore concentration (India ink, upper left) and $2\times$ scattering (Intralipid, lower right) relative to the background. The top slices are closer to the source plane and the lower slices are closer to the detector plane as in the 3D simulations.

Again, as expected (but this time with experiment rather than simulation), we find that FD imaging reduces the crosstalk between absorption and scattering quite dramatically. There is a "frame" of higher contrast levels on the edges of the absorption image in the FD reconstruction in Figure 4.44, but that region lies outside the sensitivity range of our measurement and suggests

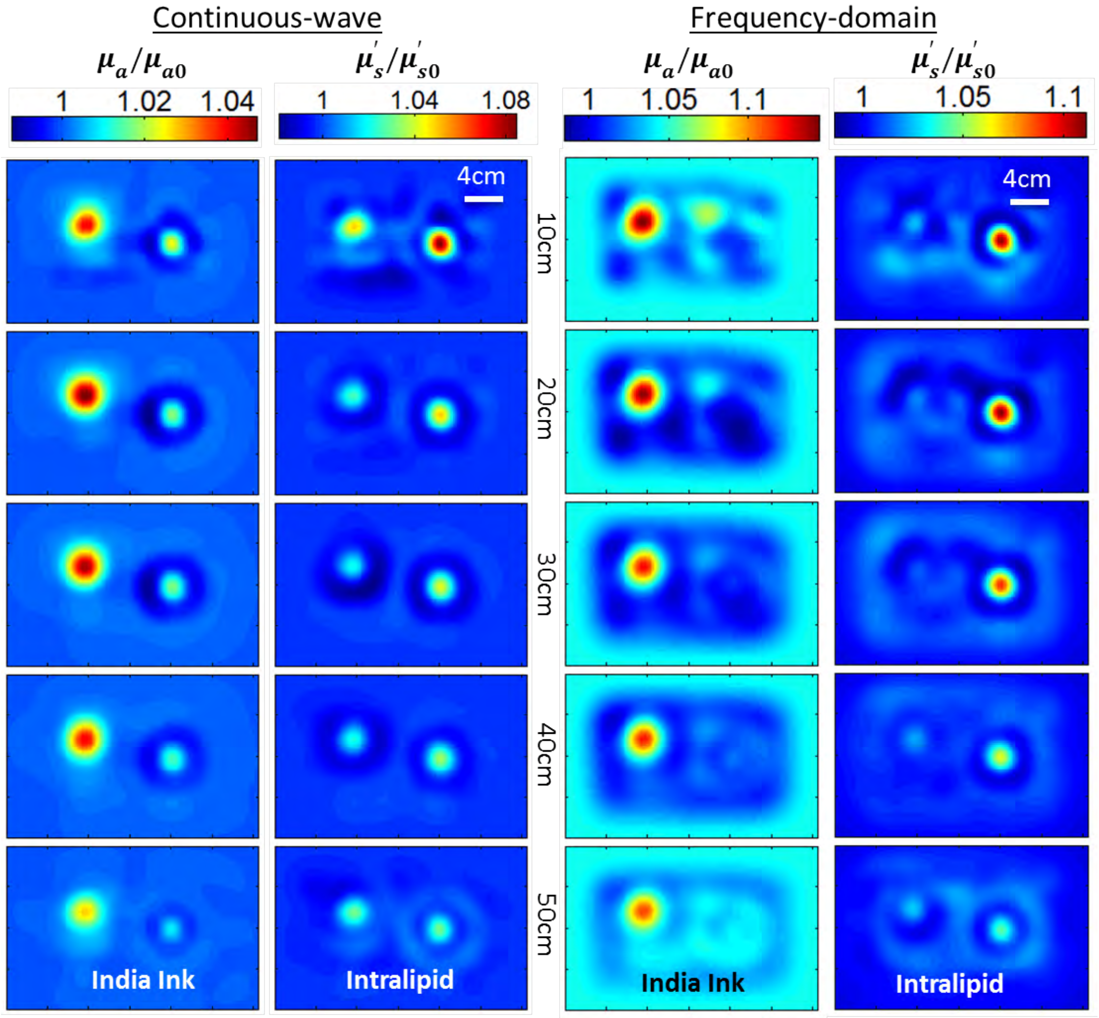

Figure 4.44: 3D reconstruction of tissue phantom. The upper left target is India ink with $3\times\ \mu_a$ contrast and the lower right target has a higher Intralipid concentration with $2\times\ \mu_s'$ contrast compared to the background. The CW reconstructions (left) have relatively low contrast and high crosstalk while the targets are well resolved spatially. In the FD reconstructions (right) noticeable artifacts near the source are apparent, but significantly less crosstalk between μ_a and μ_s' is observed. The top slices are closer to the source plane and the lower slices are closer to the detector plane (as in the 3D simulations).

that updated/better initial guesses of the background properties could improve our reconstruction. In addition, the image appears to suffer from artifacts near the source plane; these artifacts near the source and detector surfaces are known to arise in DOT, and methods exist that can be employed to ameliorate them, e.g., spatially variant regularization. However, we did not implement the spatially variant regularization technique here; it will be explored in future work. Nevertheless, the spatial structure of the reconstructed targets are well resolved in the transverse direction with some target broadening/elongation towards the source plate for both absorption and scattering objects. Again, a lower number of sources (60 of 209) and detectors ($\sim$ 320 of 5000 pixels) was utilized in the tomography so that we could carry out the reconstructions faster ($\sim 6-8$ hours/reconstruction) with this data set. (Note, the small number of detectors is perhaps less of an issue than the sources, because adjacent pixels are averaged in software to increase the SNR.)

Although the spatial structure of the images is reasonably good, one nagging question concerns contrast (or lack thereof) of the tissue phantoms and to a lesser extent, contrast in our 3D simulations. The actual reconstructed contrast is less than expected. This effect has been observed previously in DOT devices [10,44,181], and it has largely been attributed to the spreading of the reconstruction contrast that arises when the target (in the reconstructed image) is spread out in size compared to the true target dimensions. The effective contrast in such images depends on a product of the target volume and target contrast (e.g., when a reconstructed absorption target is broadened in size (volume), then its absorption contrast is decreased in proportion to the volume). This problem is exacerbated in 3D, since there is an additional stretching in the longitudinal direction. In addition, some of the underestimation of optical contrast is also due to systemic offsets inherent in the instrument or reconstruction method which can be compensated with calibration phantoms [182]. In fact, an area of research that these results suggest should be pursued, concerns how to rescale the image contrast; one approach to this problem is to utilize standard targets as part of every experimental run. In the case of our absorption and scattering

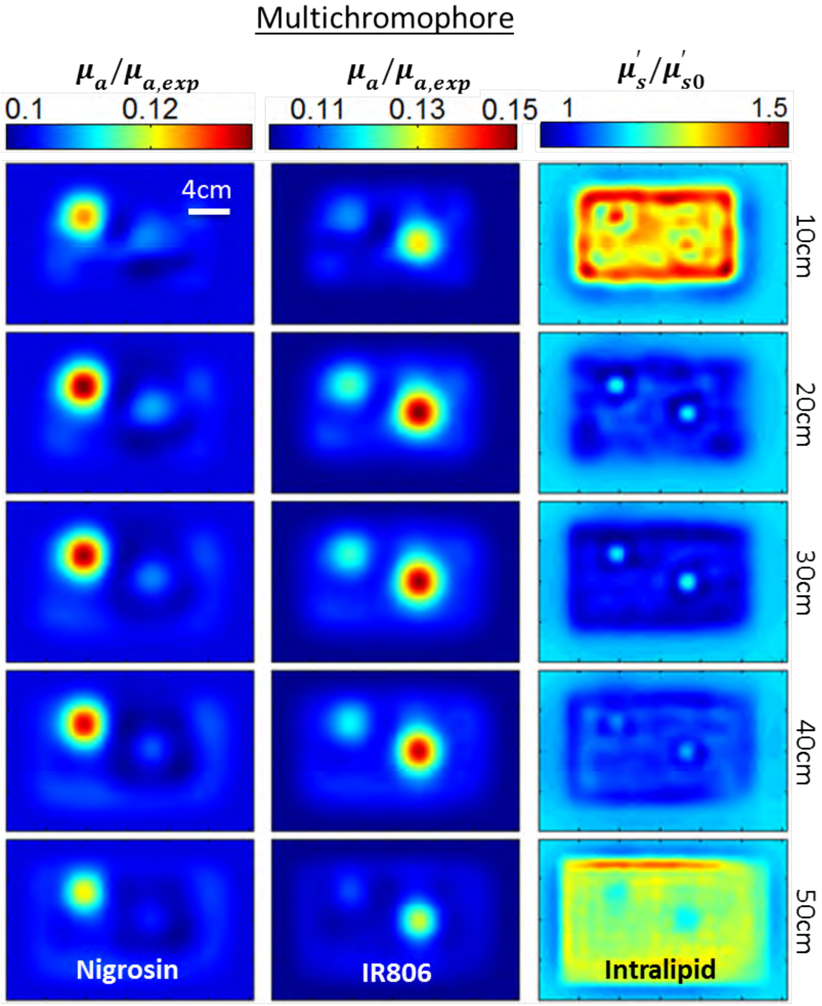

Figure 4.45: 3D reconstruction of the multi-chromophore data with Nigrosin (top left) and IR806 (bottom right) dyes with 2× background absorption. The absorption reconstructions looks similar to earlier iterations in the simulation (Figure 4.42(a)). Increasing iterations past ~ 40 for the data does not improve image quality as it is noise limited. Contrast level is low, but the main spatial features separate nicely.

targets, the integrated signal is $\Gamma = \delta\mu_a \cdot V$, where $\delta\mu_a$ is the fractional difference from the background, and V is the target volume. Here we will use the approximate shape of the target object to estimate volume; using the FWHM to determine the bounding volume and integrating the $\delta\mu_a$ absorption within that volume, we determine $\Delta\Gamma^{\mu_a} = \Gamma^{\mu_a}_{recon}/\Gamma^{\mu_a}_{expected} = 0.35$. This result (i.e., obtained by integration over the volume of the target object) is reasonable, especially given that our contrast is very large and will thus contribute to the signal in the nonlinear regime (i.e., outside of the small perturbing limit), and given that the object shapes are not perfect spheres, and given that our target objects have optical index of refraction differences with respect to the background that are not accounted for in the reconstructions. Similarly for the scattering contrast we found $\Delta\Gamma^{\mu_s'} = 0.36$. For comparison, in the CW case, we found $\Delta\Gamma^{CW,\mu_s'} = 0.16$ and $\Delta\Gamma^{CW,\mu_s'} = 0.05$. The resolution of the scattering target is quite good (except in the longitudinal direction as we have discovered with our simulations, but remember we do not employ any spatially variant regularization here). As expected the absorption targets are broader and larger than the scattering targets; in the future, we will explore more TV parameters to increase the absorption resolution.

In a different type of study, we employed two tissue phantoms to test the multi-spectral capabilities of the Gen3 imager. The two targets shown in Figure 4.34 were each filled with Nigrosin and IR806, respectively, to give approximately $2\times$ the absorption and the same scattering as the background Intralipid solution at 785 nm ($\mu_a = 0.04\ \mathrm{cm}^{-1}$, $\mu_s' = 8\mathrm{cm}^{-1}$). For this data set we increased the number of sources (209 of 209), while keeping the number of detectors the same as the previous experiment ($\sim$ 320 of 5000).

Figure 4.45 shows the 3D reconstruction of the two targets compared to the simulation.

There is a clear separation of the chromophores in the image with a small amount of crosstalk, especially in the IR806 reconstruction ($\sim 10\%$). Less crosstalk is apparent in the Nigrosin chromophore reconstruction, and this improvement could be due to the strong spectral sensitivity of the Nigrosin across the different wavelengths; by comparison, IR806 has very low contrast at the lower wavelengths. At higher iteration number, the simulations suggest that the two chromophores will eventually be differentiated. Unfortunately, at this time the data reconstruction is noise limited to 80 iterations after which no further improvements or difference in image quality can be found. For Nigrosin, $\Delta\Gamma^{Nigrosin} = 0.90$ which accounts for most of our contrast. The volume contrast for IR806 was also quite good with $\Delta\Gamma^{IR806} = 0.78$. The crosstalk in the scattering images from the absorbing targets were found to be $\sim 10\%$ in this situation. Two reasons might explain the improve contrast: the increased number of sources could improve resolution and the lower perturbation ($2\times$ background instead of $times$) of the absorbers puts the problem more in the perturbative limit. Improving resolution with increased numbers of sources and detectors, improving our SNR which gives greater numbers of off-axis measurements, improving absorption resolution with different regularization, are all obvious issues we hope to explore in the near future with the Gen3 imager as a result of these experiments.

4.10 Clinical Results: Breast Images

The Gen3 breast imager resides the in Perelman Center for Advanced Medicine at the Hospital of the University of Pennsylvania. It is currently being tested on breast cancer patients. These first patient measurements have helped us to develop and improve the clinical hardware and software interfaces. Patient measurements present a unique set of challenges that constrain our data sets.

The primary challenge is measurement time; we want to keep it as short as possible. Other challenges are present too. For example, the optical properties and breast boundary shapes vary quite a lot and are unique to each patient. In addition, unlike the tissue phantom experiments, the location and extent of the lesions in our clinical images are not known apiori; even if an MRI of the breast has been taken, the MRI measurement is usually made at a different time and in a different geometry, and of course, MRI has contrast mechanisms that are different from optics. Thus, with some trepidation, in this section we present first results from the study of two patients with the Gen3 breast imager.

4.10.1 Patient Measurement Protocol

First we describe the patient measurement protocol which was developed in accordance with the policies outlined by the University of Pennsylvania's Institutional Review Board (IRB). We have taken pains here to elucidate the protocol in a step-by-step manner. The future user of the instrument will benefit greatly from this step-by-step description.

1. Instrument setup and preparation.
    (a) The laser system, CCD, frequency generators, and all hardware are turned on and allowed to stabilize for at least 1 hour.
    (b) A large polyethelene bag is placed within and then attached to the breast tank. Care is taken to insure that the bag is set flush against the source plate, window and side ports.
    (c) The galvo switch alignment is adjusted to maximize light throughput and minimize instability before the measurement (note, this alignment can be done the night before).
    (d) An optically matched India Ink and Intralipid solution is made before the patient arrives. A typical solution would have approximate absorption and scattering values of

$\mu_a = 0.06\ \mathrm{cm}^{-1}$ and $\mu_a = 8\mathrm{cm}^{-1}$, respectively, at 785nm.

2. Once the patient has been consented and instrument preparation has been made, the patient is placed on the Gen3 bed.
    (a) The breast is then softly compressed between the source and detector plate until the patient experiences only a slight discomfort. Typical plate separation is 6 cm. When compression is complete, the plates are locked into place.
    (b) The headrest and exam table height are adjusted for the patient. It is worthwhile to take the time needed for this adjustment to be sure the patient is comfortable. Patient comfort is important for reducing movement during the measurement.
3. The first data taken is associated with the profilometry measurements.
    (a) Left side projector/camera measurement is taken.
    (b) Then the right side projector/camera measurement is taken.
    (c) Finally, the front illuminated Gen3 CCD measurement is made.
4. The breast imaging tank is filled with the India Ink and Intralipid solution that was prepared earlier (to match patient breast optical properties).
5. The system light intensity and the detection gain is adjusted to optimize detection dynamic range (Figure 6.5).
    (a) The image intensifier MCP gain (typically 570V) is adjusted at brightest source position; this task enables us to check for signal saturation, etc.
    (b) The attenuator is adjusted for pickoff light level to prevent detector saturation (i.e.,, to at most $\sim$ 50K counts for brightest laser).
6. Start the breast DOT measurement. With the current instrumentation, the duration of this

measurement is $\sim$35 minutes.

7. When the measurement is finished, then the patient will dress, and during this time period the tank is prepared for the reference measurement.
   (a) At the same source plate and window separation (i.e., as used for the patient), fill the tank to top with Intralipid solution.
   (b) Place the solid chest wall phantom on top of tank (Figure 3.5, ensuring contact between phantom and Intralipid solution.
8. Begin reference measurement.
9. Obtain an image of the source positions. This image helps us locate the source positions in for the reconstruction.
   (a) Empty breast imaging tank of Intralipid.
   (b) Move source plate to detection plane.
   (c) Illuminate fiber bundle face via the galvo, and take image of this source plate with the Gen3 CCD.
10. Calibrate Profilometry measurement using calibration target (Figure 4.27)
   (a) Place calibration target in breast imaging tank.
   (b) Left side projector/camera measurement.
   (c) Right side projector/camera measurement.

4.10.2 Cancer Patient 1

Our first patient is a 79-year-old post-menopausal Caucasian female. Ultrasound found hypoechoic nodules which span approximately $18 \times 10\text{mm}$ at the 3:30 region of the breast, 4 cm from the areolar margin. A left breast core biopsy confirmed the presence of infiltrating mammary carcinoma with ductal and lobular features, and with intermediate grade nuclei. The patient consented to participate in our study in accordance with the consent policies outlined by the university's IRB. With the location of the tumor in mind, an effort was made to optimally place the patient's breast into the imaging tank. The plates were then compressed gently to fit the breast and achieve patient comfort. The final plate separation had a fixed distance of 64mm.

The profilometry images were taken before the box was filled with Intralipid solution as described in Section 4.10.1. After optimization of the light level and detection gain for this particular breast, the DOT scan was initiated and run for 34 minutes. Finally, when the patient measurement was complete, a reference DOT scan was made with the box filled completely with Intralipid, and with the chest wall INO phantom (from Section 3.2.4, Chapter 3) placed over the breast tank hole. This block was placed on top of the tank in order to extend the diffuse medium in a manner analogous to the patient's chestwall; this configuration also helped prevent signal saturation caused by air boundaries. After the optical exam, the patient received a bilateral MRI. The MRI of the breasts was performed on a 1.5 Tesla magnet at HUP. In the lower-outer left breast, the MRI detected an area of abnormal enhancement that measured approximately $70 \times 13 \times 33$ mm.

Figure 4.46 shows the DOT reconstruction from the patient. T1 image slices from an MRI are shown, and the multi-spectral frequency-domain images of the hemoglobin concentration

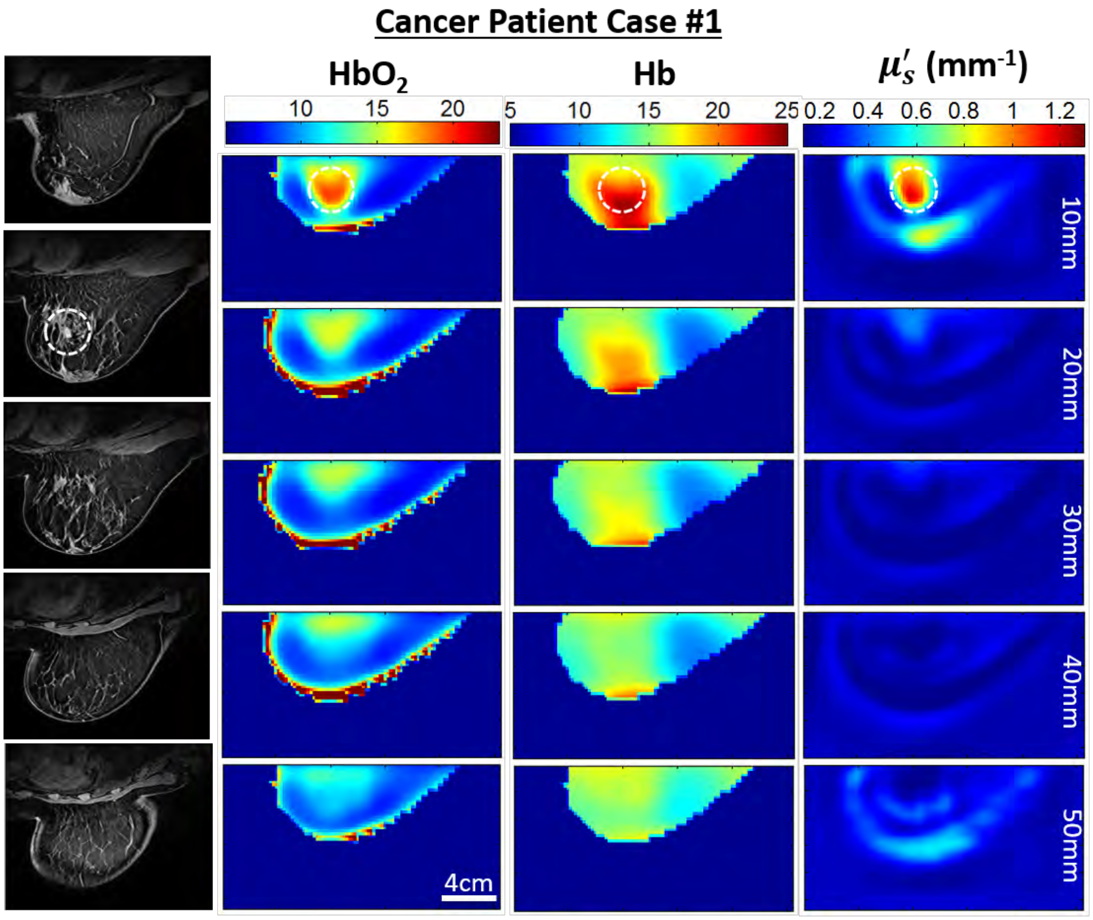

Figure 4.46: MRI and DOT images of a 79-year-old post-menopausal Caucasian female with breast cancer. The first column shows an MRI of the cancer patient. Columns 2-4 show results from the 3D multi-spectral frequency-domain DOT reconstruction of HbO_2, Hb, and μ_s' at 785nm. The tumor location in the MRI and the corresponding area in the DOT images are indicated by white dotted circles. Note, however, the MRI and DOT breast compressions are similar but are not identical. Interesting features are apparent in both images with high HbO_2, Hb and scattering near the tumor region (identified with biopsy clip in the MRI).

(HbO_2), the deoxy-hemoglobin (Hb), and scattering (μ_s') are shown. The MRI slices was chosen to correspond to the slice of the DOT images by choosing equally spaced slices. In Figure 4.47, the derived parameters of total hemoglobin concentration $THC = HbO_2 + Hb$, blood oxygen saturation $StO_2 = HbO_2/THC$, and an optical index $OI = THC \times \mu_s'/StO_2$ (normalized to healthy region) are exhibited. The optical index is a parameter which seeks to maximize optical

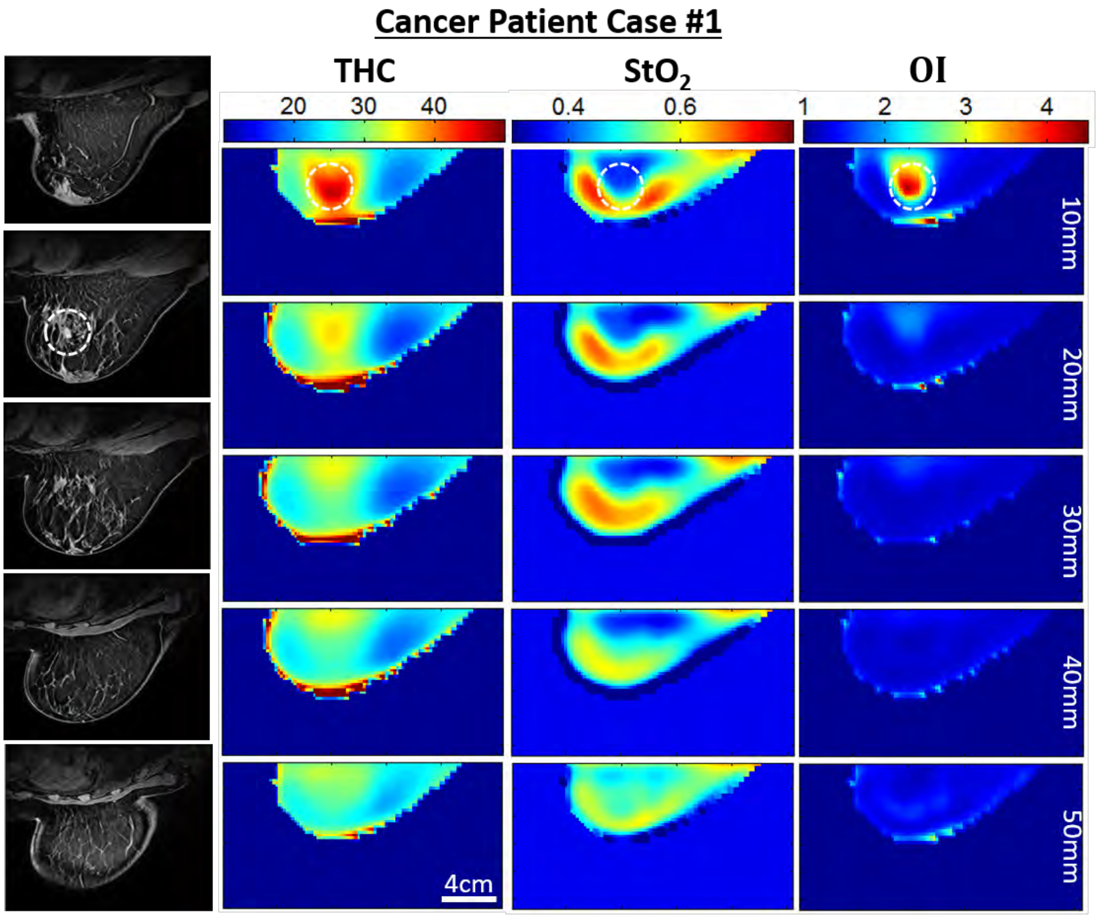

Figure 4.47: MRI and DOT images of a 79-year-old post-menopausal Caucasian female with breast cancer. The first column shows an MRI of the cancer patient. Columns 2-4 show results from the 3D multi-spectral frequency-domain DOT reconstruction of the THC, StO_2, and OI at 785nm. The tumor location in the MRI is indicated by a white dotted circle. White dotted circles also indicate suspected tumor location on the DOT images. StO_2 shows depressed oxygenation region near the tumor location.

contrast with the assumption that in tumors an elevated level of THC and μ_s' and depressed levels of StO_2 might be expected [24,53,93]. The optical/physiological properties all fall within realistic values for the breast. Importantly, in the 10mm slice the DOT images show significant contrast for multiple optical parameters. The dotted circle region where we suspect the tumor is located in Figure 4.46, show a contrast of $HbO_2 \sim$ 2.8, $Hb \sim$ 1.7, $\mu_s' \sim$ 4, $THC \sim$ 1.7,

$StO_2 \sim 0.8$, and $OI \sim 11.6$ when compared to the health region (i.e., as estimated from MRI and from other examinations). From the Hb and Hb images on the same plane the tumor can be estimated to be $25 - 35$ mm in diameter.

Much work remains. As in the simulations and phantom experiments, it appears that the tumor region might be closer to the source plane than expected from the MRI. This first patient result is promising. A tumor was imaged. This tumor was quite large, and it is certainly possible that the surrounding tissues also have optical properties that are different from normal tissues and therefore give rise to a further broadened spatial contrast. Furthermore, the imaging geometries of MRI and DOT are not the same, and thus the lesions could be spatially shifted in corresponding images. Of course, numerous issues remain to be addressed. For example, why does the contrast seem to be stronger near the source plane? We know that artifacts tend to arise near the source and detection planes, but we need to find ways to reduce these effects. In the future (see Chapter 5), many improvements can be made which should lead to improvements in the DOT images.

4.10.3 Cancer Patient 2

The second patient is a 68-year-old post-menopausal Caucasian female. She is positive for invasive mammary carcinoma with ductal and lobular features with associated in-situ carcinoma, and with intermediate nuclear grade. Ultrasound evaluation of this region showed a 15 mm mass with associated calcifications at the 12:00 region of the breast. A right breast core biopsy confirmed the presence of invasive mammary carcinoma with ductal and lobular features associated with the in-situ carcinoma, and intermediate nuclear grade. This patient was consented in accordance with the policies outlined by Penn's IRB. The individual's breast was gently compressed

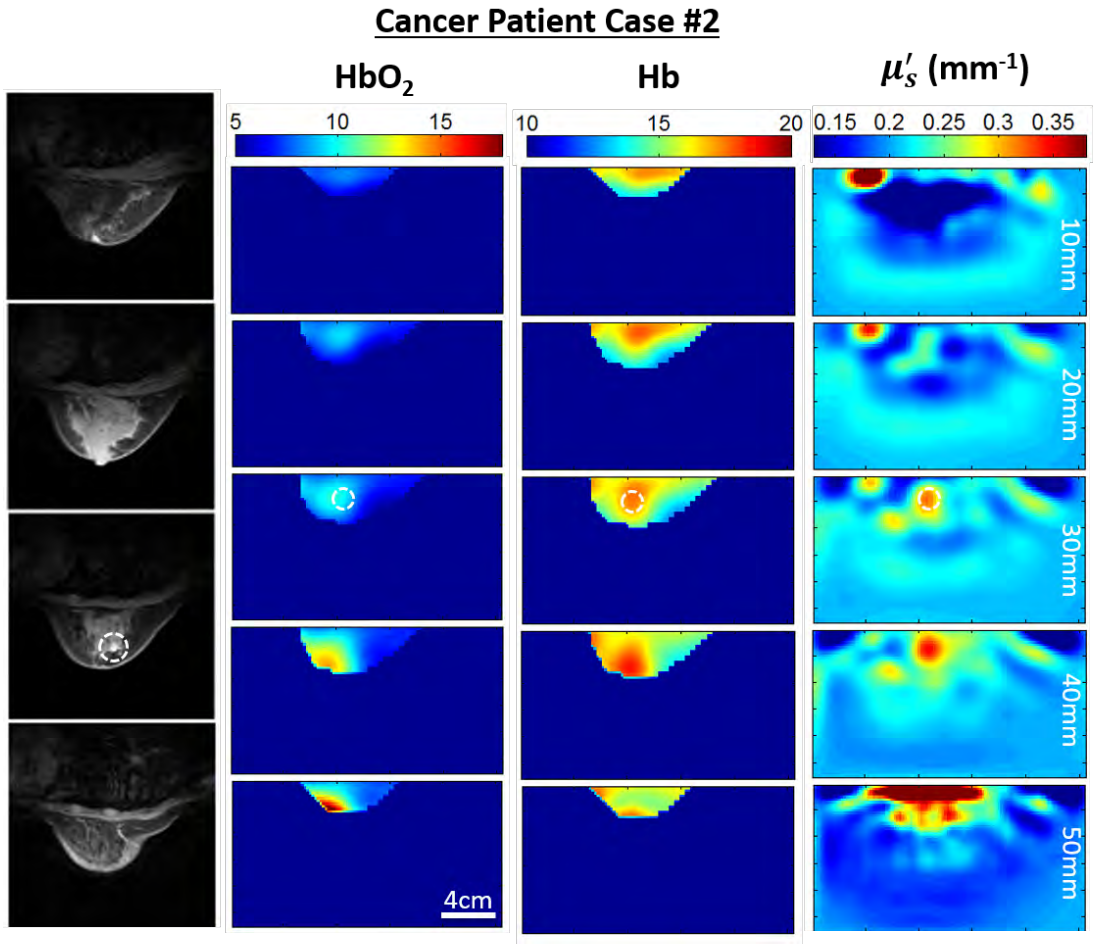

Figure 4.48: MRI and DOT images of a 68-year-old post-menopausal Caucasian female with breast cancer. The first column shows the MRI of the cancer patient. Columns 2-4 show results from the 3D multi-spectral frequency-domain DOT reconstruction of the HbO_2, Hb, and μ_s' at 785nm. The tumor location in the MRI and DOT images are indicated by white dotted circles. The MRI and DOT breast compressions are similar but are not identical. Possible tumor location shown in HbO_2 (identified with biopsy clip in the MRI). The μ_s' image seem to have difficulty with this particular patient where there are large artifacts near the source and detector plane.

to achieve patient comfort; the plate separation was fixed distance at 60 mm. A measurement procedure similar to that of Patient 1 followed. After completion of the research study, the patient received an MRI bilateral image of her breasts in a 1.5 Tesla magnet. The MRI reported a moderate-to-large amount of glandular tissue. Approximately 9 mL of gadolinium contrast

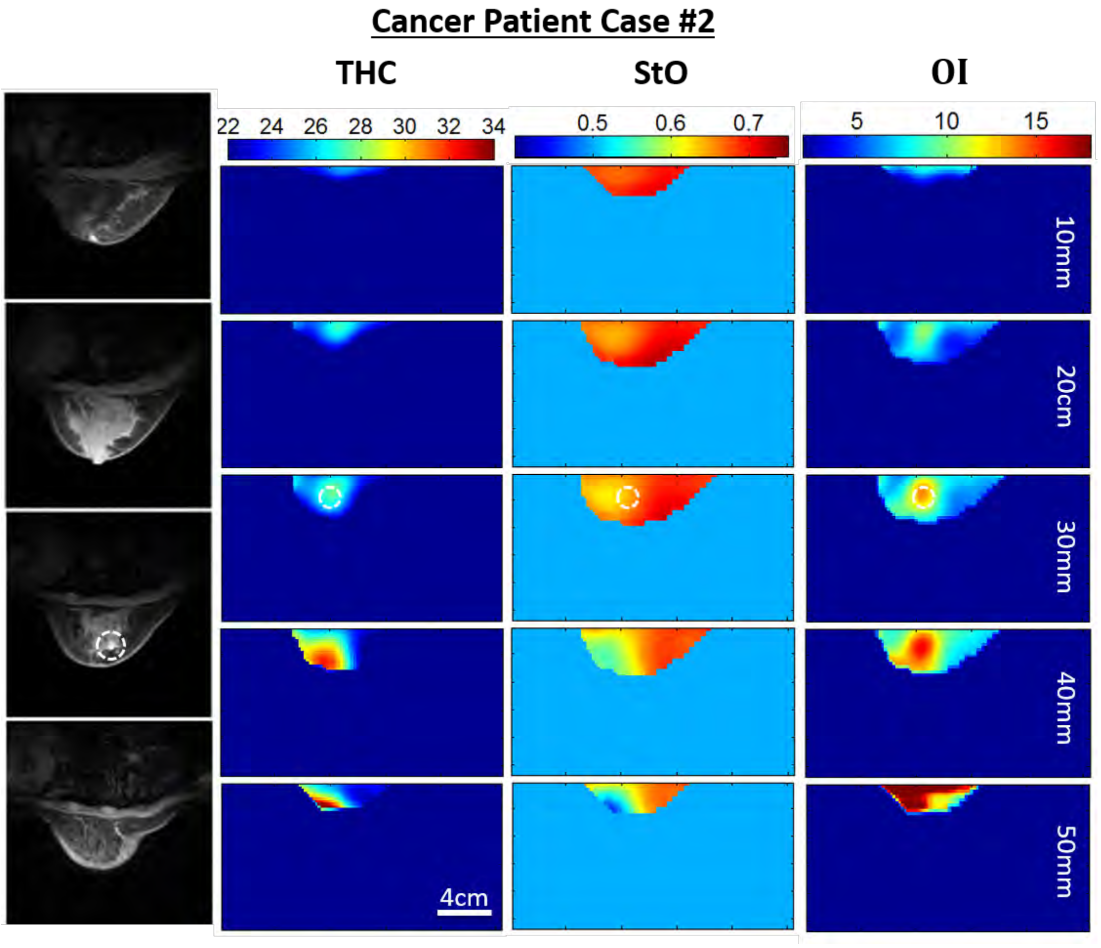

Figure 4.49: MRI and DOT images of a 68-year-old post-menopausal Caucasian female with breast cancer. The first column shows the MRI of the cancer patient. Columns 2-4 show results from the 3D multi-spectral frequency-domain DOT reconstruction of the THC, StO_2, and OI at 785nm. Interesting features are apparent in both images with high THC, StO_2 and scattering near the tumor region.

was administered intravenously for the MRI, and a 2 cm irregular mass was revealed in the upper-inner anterior right breast. There was also a linear enhancement in gadolinium contrast extending from the index mass anteriorly and posteriorly, with the overall extent of enhancement approximately $4\ \mathrm{cm}$. In addition, a cluster of enhancing irregular masses was found in the upper outer breast at middle depth.

This patient presents a difficult case for x-ray, because of its high radiographic density. Figure 4.48 and 4.49 shows the MRI as well as optical images for this patient. In this patient he tumor is difficult to locate but the suspected tumor has been circled in the $30\ \mathrm{mm}$ slice of the DOT image. The dotted white circle region where we suspect the tumor is located show a contrast of $HbO_2 \sim 1.4$, $Hb \sim 1.1$, $THC \sim 1.4$, $StO_2 \sim 0.8$, and $OI \sim 2$ when compared to the health region. The reconstruction algorithm also seemed to have difficulty with the scattering region, and thus it is challenging to ascertain a localized tumor area because of scattering artifacts near the source and detector plane. As was the case with the first patient, the tumor in this case was quite large and somewhat diffuse, and it is certainly possible that the surrounding tissues also have optical properties that are different from normal tissues and therefore give rise to a further broadened spatial contrast; further, since the imaging geometries of MRI and DOT are not the same, the lesions in the corresponding images could be spatially shifted. Again, looking to the future (see Chapter 5), the first results show promise, but many improvements can and should be made which will very likely lead to improvements in the DOT images.

4.11 Summary

In this chapter I have described a DOT breast imager that has been developed for clinical use. The instrument utilizes a spatially dense (10^7) source-detector pair arrangement, as well as multispectral and frequency-domain data types to push standalone DOT imaging capabilities in the clinical environment. These particular data types and source-detector geometry were explored with imaging simulations, and the instrument was characterized and validated with tissue phantoms. In addition, first image reconstructions from cancer patient data has been obtained. These steps represent a beginning and will soon lead to needed further development and optimization of image reconstruction and the hardware. Then the Gen3 imager will be translated to address specific clinical problems.

Chapter 5

Summary

In this thesis, I have presented research that further develops Diffuse Optical Tomography for clinical breast imaging. This research was challenging because of its many facets, which ranged from subtle optoelectronics in the physics instrumentation to complexities of the diffuse optical inverse problem algorithms and computation to our evolving understanding of breast cancer biophysics and biophotonics. Ultimately, the clinical grade instrumentation we have built is nonionizing (safe), low-cost (commercially attractive), high-throughput (accessible), and scalable (flexible). On the clinical side, DOT has many possible niches. The non-invasive optical modality, for example, is attractive for medical niches such as detection and characterization of cancer in the radiographically dense breast (e.g., for fibrotic breasts characteristic of, but not limited to, young women), for repeated imaging in populations with genetic predisposition to develop breast cancer (e.g., populations with BRCA mutations), for detection of some breast cancer phenotypes that are sometimes been difficult to observe with traditional mammography (e.g., some DCIS lesions), for use in combination with other techniques to improve diagnosis (e.g., multi-modal imaging), for tracking functional information about cancer response in neoadjuvant chemotherapy monitoring (e.g., to adjust the drug regimen), and more.

In Chapter 3, I used phantom experiments to systematically investigate the effects of the chest wall on diffuse optical tomography (DOT) in the standard parallel-plate (slab) breast imaging geometry. Resolution and image quality was studied using a spatially-dense (source-detector) data set and linear reconstruction methods. This research lead us to several promising conclusions. First, although the presence of the chest wall phantom in close proximity to the target complicates the inverse problem, we are able to reconstruct images of absorption contrast with CW data. Further, we showed that the most severe effects of the chest wall can be rectified by appropriate data restriction in conjunction with linear image reconstruction. In the work, we carried out both fast reconstructions using an analytical reconstruction method, and we developed and experimentally verified an algebraic image reconstruction which turned out to be well suited for use with these data sets that are compromised (and restricted versions of these data) by the presence of the chest wall.

In the future, we will want to consider the research from Chapter 3 in a clinical context. In practical clinical applications of DOT, the location of the chest wall relative to the sources and detectors should be known, and therefore data restriction can be applied *in vivo*. Further, the fast reconstruction times of the linear methods, and the ever improving computation and memory costs, make real-time DOT imaging an appropriate goal in the clinical setting. If successful (and work remains to achieve this goal), then it should be possible to develop data-driven algorithms for data rejection in the clinical imagers which could utilize real-time adjustment of patient position, etc. Of course, further exploration of these datasets with nonlinear inversion methods should be interesting too. Additionally, my research points to the need to explore applications of optical projection imaging, wherein the 3D tomographic images slices are averaged over the whole depth of the plane-parallel (slab) sample; projection imaging appears to have real potential. Our research found that the projection images are much less sensitive to systematic errors typically encountered in image reconstruction, i.e., compared to the individual reconstructed slices; reconstructed slices often exhibit severe image artifacts, especially near boundaries. The projection images, by contrast, were found to be free of many of these artifacts and to display the targets clearly. (Recall that projection images still require 3D DOT.) This finding may be significant since the optical projection image is rather similar to x-ray radiographic projection, yet it displays optical contrast that is correlated to functional information about tissues (and can possibly be acquired real time). Interestingly, with my clinical instrument, discussed in Chapter 4, it is possible to carry out breast imaging in two different orthogonal geometries (frontal and sagittal); thus, with two orthogonal image projections (used in tandem), more accurate renderings of the tumor size, shape and character will be possible with fewer artifacts. Finally, it could be very interesting to implement this projection image data as a prior (i.e., initial guess) for nonlinear reconstructions.

In Chapter 4, I described the instrumentation that I built for clinical breast DOT in great detail. The instrument provides unique imaging opportunities for the field because it has a spatially dense (10^7) source-detector pair arrangement and multi-spectral/frequency-domain data types. The result of my effort is the most data-intensive stand-alone DOT instrument yet reported. The instrument was characterized and validated with tissue phantoms. Further, first cancer patient data has been obtained. All of this initial data is now being used for reconstruction and hardware optimization.

Specifically, for our particular data type (frequency-domain) and source-detector geometry (slab), we explored a small subset of possible reconstruction algorithms with various regularization techniques (Tikhonov, Perona-Malik, Total Variation) in 2D and 3D. We carried out studies with simulated data to test multi-chromophore and simultaneous absorption/scattering reconstructions. We then tested the whole combination of instrumentation and algorithms (i.e., the best versions of the algorithms that we found in the studies of simulated data) using tissue phantoms. In the process, we learned that with separate (i.e.., independent) regularization (TV regularization) for absorption and scattering, the properties and resolution of the reconstructed absorption targets were improved. We are also learning that tissue phantom and clinical problems are different enough to warrant different reconstruction approaches, because the target objects with sharp versus smooth optical transitions are imaged differently when employing different reconstruction approaches.

This research represents the beginning of the clinical translation process. Thus far only a small number of issues in the vast phase-space of our reconstruction software and in our Gen3 imager hardware has been explored. In the future, we will investigate the effects of combining multiple regularization schemes, e.g., wherein some are spatially variant to reduce artifacts that arise near the source and detector planes, and we will explore other regularization parameter spaces and iterative image reconstruction processes. To try and further reduce these source and detector plane boundary effects, we will try reconstructing source coupling coefficients and/or the boundary conditions as a free parameter. Using the index of refraction as an additional parameter could also yield interesting physiological information and improve reconstructions.

In addition, the use of scattering or absorption only reconstructions as an image prior for a full reconstruction is also an idea that is being explored.

In a different vein, and importantly, we also learned that upgrades in the instrument signal-to-noise ratio (SNR) will translate to improved reconstruction fidelity. To this end, we will explore hardware improvements such as pixel binning to decrease readout noise, increasing the cross-correlation frequency to reduce pink noise near zero frequency (e.g., even an increase from 1 Hz to 2 Hz should substantially reduce noise), increasing the modulation frequency to improve phase contrast (e.g., even an increase from 70 MHz to 85/90 MHz will improve phase-sensitivity and will better separate absorption and scattering contributions to the signal), increasing our data acquisition frame-rate, and increasing laser power (within allowed limits) and stability. The additional use of the measured DC signal from our heterodyne detection is also being explored to improve SNR and our image field-of-view. We will explore usage of calibration sources centered through the breast (to detect potential motional artifacts), and we will explore the usage of DOT measurements of the same breast with our two orthogonal views (frontal and sagittal). Finally, we could reduce the acquisition time significantly by selecting only those sources most needed for the reconstruction (this involves studying the full problem with 209 sources and then deleting sources and comparing the images); for example, if we could save a factor of 4 in time by using 60 well-chosen sources, then the systematics will be reduced, the time between the reference and patient measurements will be reduced, and we could add more wavelengths to detect other chromophores (if desired).

Once these improvements are implemented, and we gain more confidence in our reconstructions, the Gen3 imager will be utilized for focused work on several clinically applications. Examples of the latter that we are eager to address include imaging in the radiographically dense breast populations, imaging in the genetic high-risk populations, neoadjuvant chemotherapy monitoring, exploration of novel optical contrast agents (e.g., exogenous absorption and fluorescence contrast agents), construction of multi-modal malignancy parameters based on optical data and data from other medical imaging modalities, dynamic imaging (e.g., breast compression and decompression), and more.

Appendix A

Gen3 Software

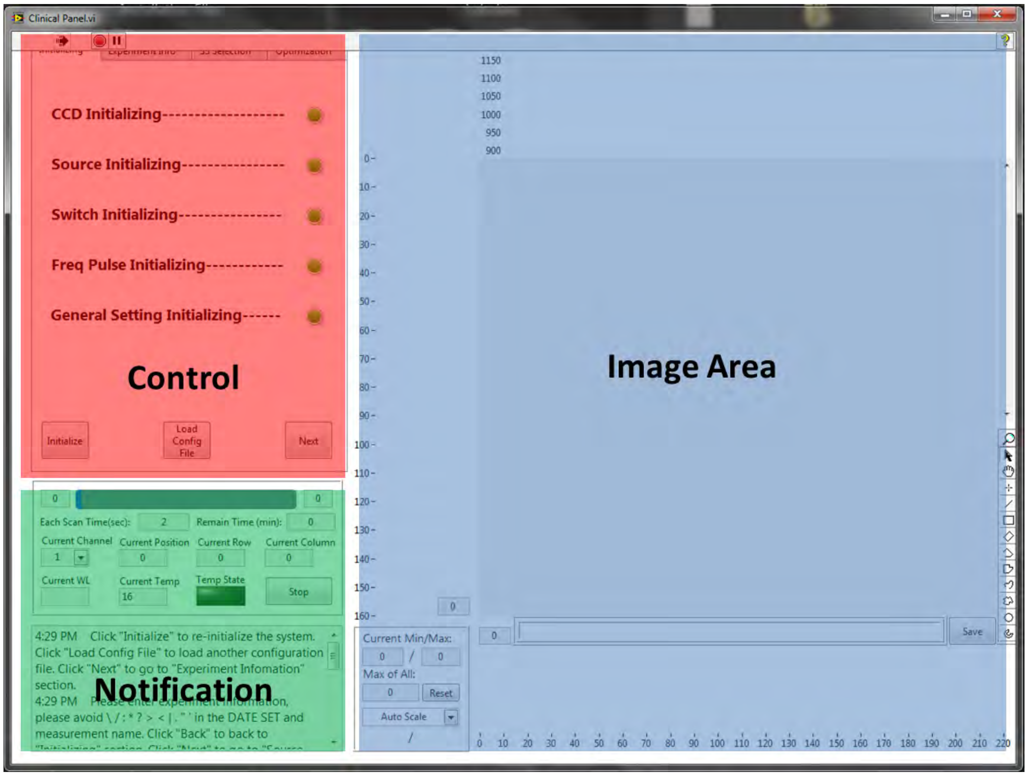

Each Scan Time(sec): 2
Remain Time (min): 0
Current Channel 1
Current Position 0
Current Row 0
Current Column 0
Current WL
Current Temp 16
Current Min/Max: 0 / 0
Max of All: 0

4:29 PM Click "Initialize" to re-initialize the system. Click "Load Config File" to load another configuration file. Click "Next" to go to "Experiment Infomation" section.

4:29 PM Please enter experiment information, please avoid \ / : * ? > < | . " ' in the DATE SET and measurement name. Click "Back" to back to

Figure 6.1: The Gen3 Clinical software written in Labview. The software consist of a control area (red) where the user interacts with the software, the notification area (area) where the instrument status and notifications are displayed, and the imaging area (blue) where the image from the Gen3 CCD is displayed.

The Gen3 Clinical software was written with our clinical collaborators in mind. It minimizes access to the hardware and simplifies the measurement process to reduce user error. Figure 6.1 shows the general layout of the software. The upper left area has the polymorphic interface controls (indicated in red) where the user mainly interacts with the software. Right below is the notification area (indicated in green) which displays the status of the instrument and various errors and notifications. Finally on the right is the image display (indicated in blue) where images from the Gen3 CCD is displayed.

The first panel that displays (Figure 6.2) is the initialization screen. Pressing the initialization button will do a system check of the CCD and the DAQ module. If there are any errors or if these

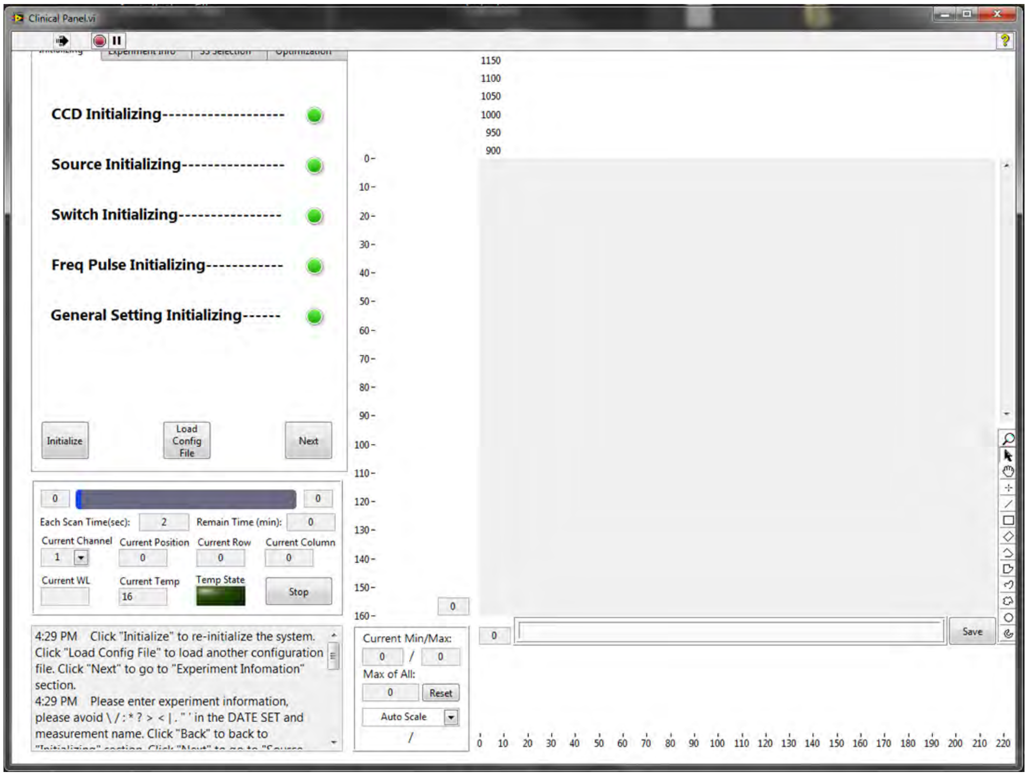

CCD Initializing------------------

Source Initializing---------------

Switch Initializing---------------

Freq Pulse Initializing-----------

General Setting Initializing------

Each Scan Time(sec): 2
Remain Time (min): 0
Current Channel: 1
Current Position: 0
Current Row: 0
Current Column: 0
Current WL:
Current Temp: 16
Current Min/Max: 0 / 0
Max of All: 0

4:29 PM Click "Initialize" to re-initialize the system. Click "Load Config File" to load another configuration file. Click "Next" to go to "Experiment Infomation" section.
4:29 PM Please enter experiment information, please avoid \ / : * ? > < | . " ' in the DATE SET and measurement name. Click "Back" to back to

Figure 6.2: The first screen in the software is the initialization configuration screen. At this step, the hardware connection and statuses are checked before allowing the user to proceed. After the hardware status is checked, the user can load a preconfigured config file or proceed without one. The user can then continue onto the next step.

parts are disconnected, it will be indicated in the notification area. If all checks are successful and all green indicators are lit, the user can then load a configuration file (that has already been created in the Gen3 Experimental Software). Once a configuration file is loaded successfully, the user may proceed by clicking “next”.

The proceeding screen is the Data input screen where the measurement details are recorded. The current date is automatically loaded and the control panel asks the user for the experiment number and the number of measurements. The minimum number of measurements is two: 1) one for the reference, and 2) one for a single breast measurement. The user can set up to 12 independent measurements before clicking “next”.

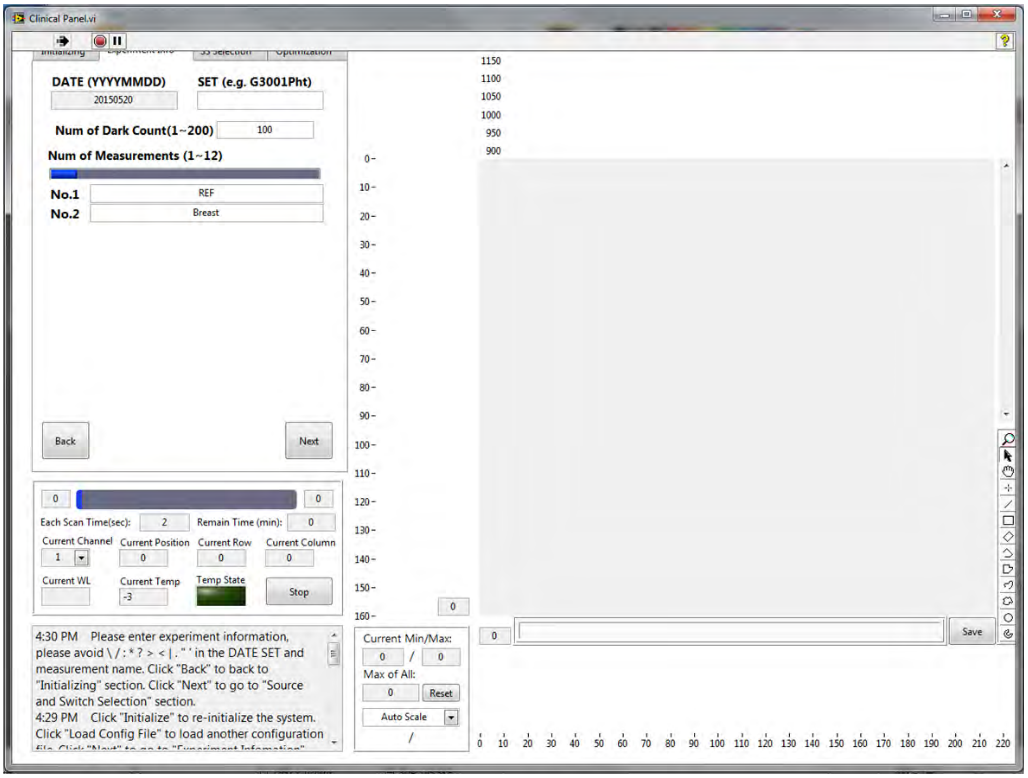

DATE (YYYYMMDD): 20150520

SET (e.g. G3001Pht):

Num of Dark Count(1~200): 100

Num of Measurements (1~12)

No.1: REF

No.2: Breast

Each Scan Time(sec): 2

Remain Time (min): 0

Current Channel: 1

Current Position: 0

Current Row: 0

Current Column: 0

Current WL:

Current Temp: -3

Temp State

Current Min/Max: 0 / 0

Max of All: 0

4:30 PM Please enter experiment information, please avoid \ / : * ? > < | . " ' in the DATE SET and measurement name. Click "Back" to back to "Initializing" section. Click "Next" to go to "Source and Switch Selection" section.

4:29 PM Click "Initialize" to re-initialize the system. Click "Load Config File" to load another configuration

Figure 6.3: The second panel is the Data input screen where the details of the measurement is entered. The patient number and the number of measurements can be indicated. The minimum number of measurements is two (typically for reference and a single breast measurement) but can be increased to 12.

The third panel (Figure 6.4) in the clinical software is the source configuration screen. Here the user can choose the sources and wavelengths that will be used for the measurement. The first 11 × 19 indicators are for the source position. The second 11 × 19 grid is the calibration source grid. The user can indicate after which source the calibration measurement is taken. In Figure 6.4, for example, the calibration source is set to be taken after every 10th source. The sources sequence during the measurement moves from top left to the bottom right (this is hard coded). The last pair of 1 × 5 indicator allow the user to choose the wavelengths for the sources and calibration sources respectively.

The fourth panel of the software shown in Figure 6.5 the optimization panel. This panel is the first panel where the CCD and lasers can be controlled by the user. At this panel, the detection

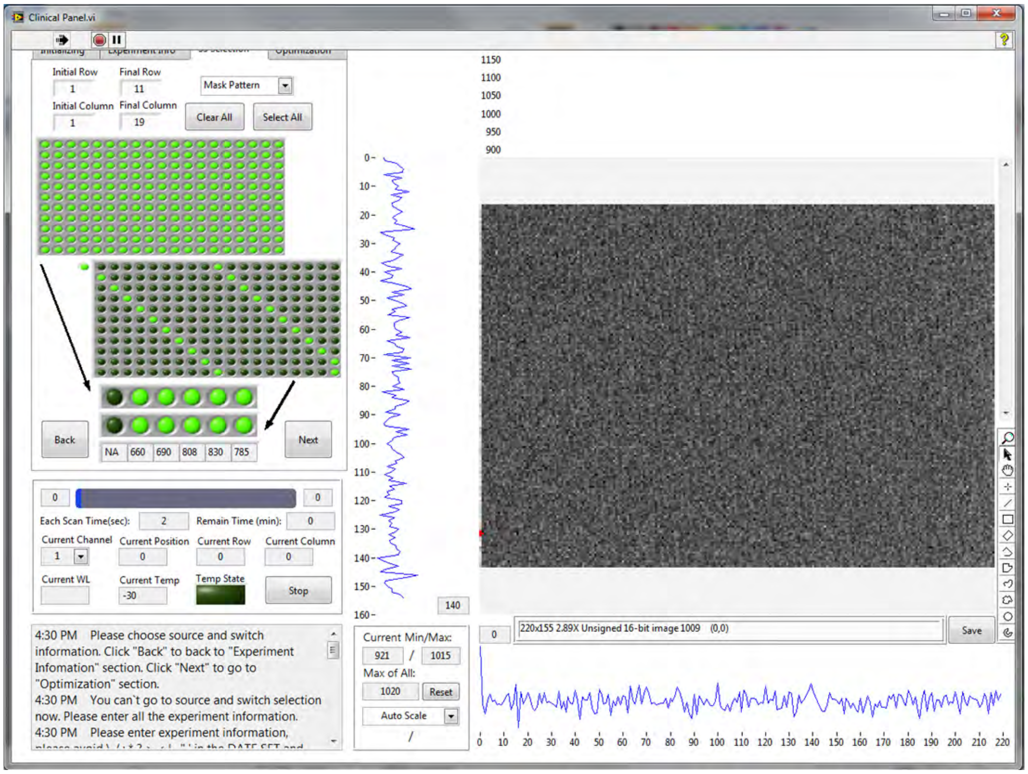

Initial Row: 1
Final Row: 11
Initial Column: 1
Final Column: 19

NA 660 690 808 830 785

Each Scan Time(sec): 2
Remain Time (min): 0
Current Channel: 1
Current Position: 0
Current Row: 0
Current Column: 0
Current WL:
Current Temp: -30
Temp State

4:30 PM Please choose source and switch information. Click "Back" to back to "Experiment Infomation" section. Click "Next" to go to "Optimization" section.
4:30 PM You can`t go to source and switch selection now. Please enter all the experiment information.
4:30 PM Please enter experiment information,

Current Min/Max: 921 / 1015
Max of All: 1020

220x155 2.89X Unsigned 16-bit image 1009 (0,0)

Figure 6.4: The third control panel is the source configuration screen. Here the source positions, the calibration measurements, and wavelengths used in the experiment can be chosen.

gain and the laser intensities are adjusted so that the CCD not saturated for the particular breast or sourceplate detection window separation distance. The pickoff light level is adjusted at this stage. Note that the pickoff does not go through the imaging tank, so it must be adjusted independently of the laser sources.

The last panel in the clinical software is the measurement panel. At this point, the user can begin the measurements. The steps displayed on this screen is dependent on the entries in the previous panels. The user simply takes the measurement from the top to the bottom. The green light after each measurement description lights up indicating that the measurement is completed.

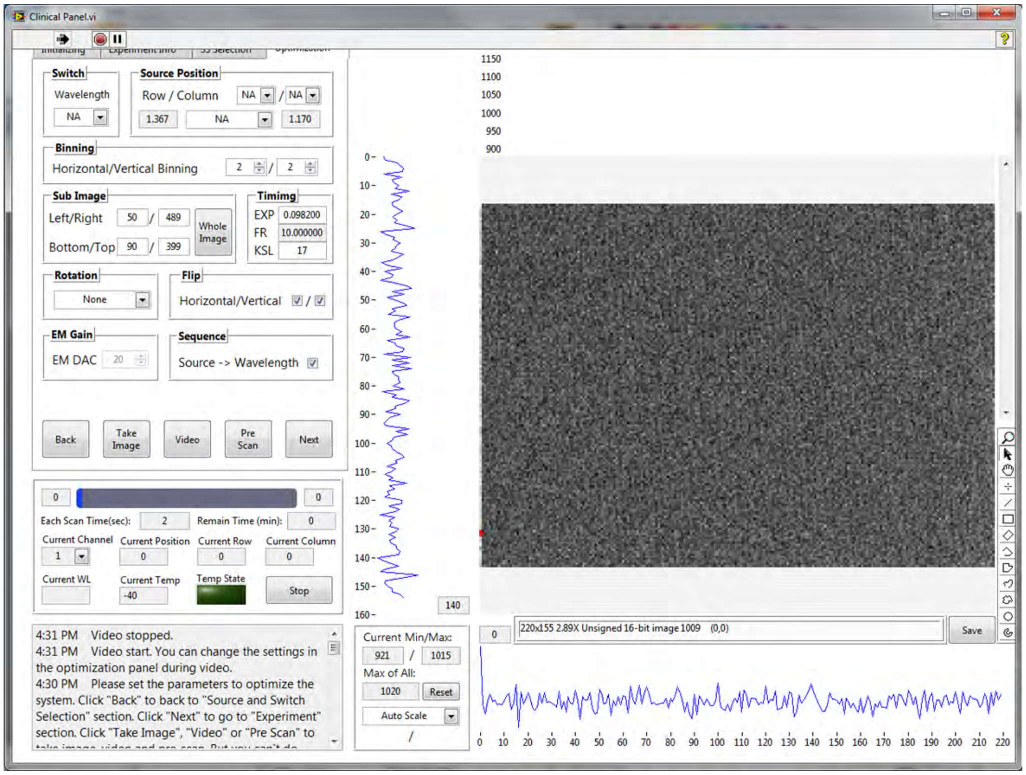

Switch
Wavelength NA

Source Position
Row / Column NA / NA
1.367 NA 1.170

Binning
Horizontal/Vertical Binning 2 / 2

Sub Image
Left/Right 50 / 489
Bottom/Top 90 / 399

Timimg
EXP 0.098200
FR 10.000000
KSL 17

Rotation
None

Flip
Horizontal/Vertical ☑ / ☑

EM Gain
EM DAC 20

Sequence
Source -> Wavelength ☑

Each Scan Time(sec): 2
Remain Time (min): 0
Current Channel 1
Current Position 0
Current Row 0
Current Column 0
Current WL
Current Temp -40
Temp State

4:31 PM Video stopped.
4:31 PM Video start. You can change the settings in the optimization panel during video.
4:30 PM Please set the parameters to optimize the system. Click "Back" to back to "Source and Switch Selection" section. Click "Next" to go to "Experiment" section. Click "Take Image", "Video" or "Pre Scan" to

Current Min/Max: 921 / 1015
Max of All: 1020
Auto Scale

220x155 2.89X Unsigned 16-bit image 1009 (0,0)

Figure 6.5: The measurement optimization screen. At this stage, the CCD can be run in video mode with the same exposure used in the actual measurements. The laser light level and detection gain is adjusted so that the CCD is not saturated or so that the light level is adequate for the current experiment.

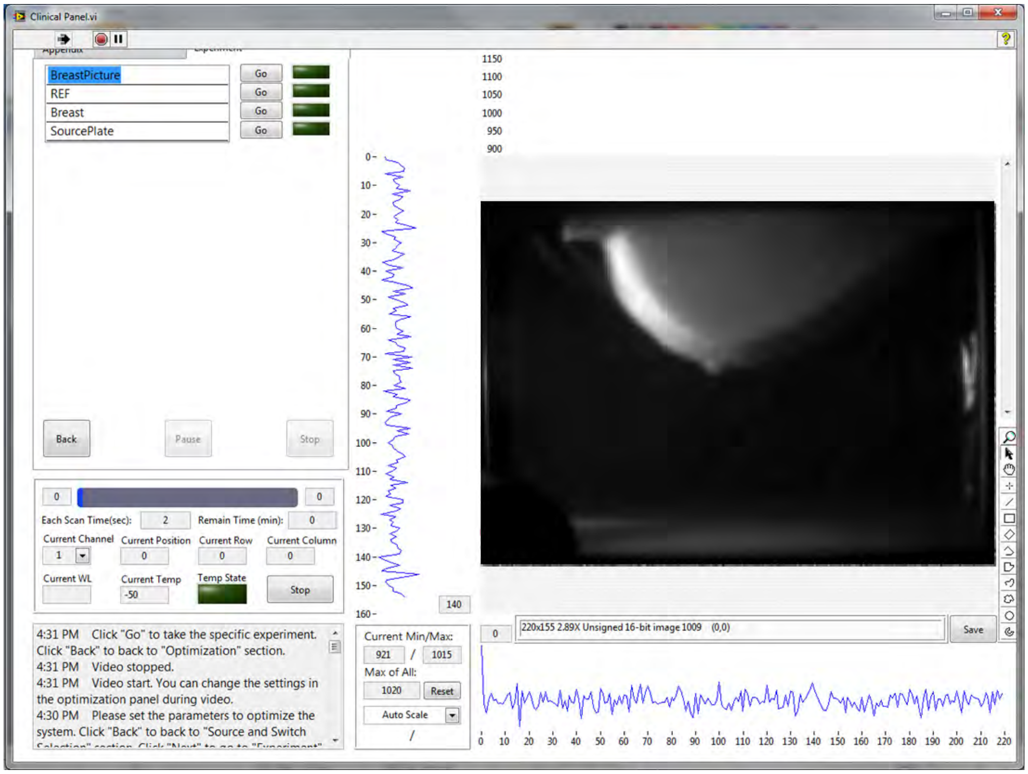

Each Scan Time(sec): 2
Remain Time (min): 0
Current Channel 1
Current Position 0
Current Row 0
Current Column 0
Current WL
Current Temp -50
Temp State
Current Min/Max: 921 / 1015
Max of All: 1020
220x155 2.89X Unsigned 16-bit image 1009 (0,0)

4:31 PM Click "Go" to take the specific experiment. Click "Back" to back to "Optimization" section.
4:31 PM Video stopped.
4:31 PM Video start. You can change the settings in the optimization panel during video.
4:30 PM Please set the parameters to optimize the system. Click "Back" to back to "Source and Switch

Figure 6.6: The measurement screen of the Gen3 clinical software. After setting up the experiment, the user takes the measurements in series on this screen by pressing the measurement buttons in sequence from top to bottom.

Bibliography

[1] Max Cutler. Transillumination of the breast. *Annals of surgery*, 93(1):223, 1931.

[2] Frans F Jobsis. Noninvasive, infrared monitoring of cerebral and myocardial oxygen sufficiency and circulatory parameters. *Science*, 198(4323):1264–1267, 1977.

[3] Frans F. Jobsis, Paul. D. Jobsis, et al. Biochemical and physiological basis of medical near-infrared spectroscopy. *Journal of biomedical optics*, 4(4):397–402, 1999.

[4] Frans F Jobsis et al. Discovery of the near-infrared window into the body and the early development of near-infrared spectroscopy. *Journal of biomedical optics*, 4(4):392–396, 1999.

[5] Akira Ishimaru. *Wave propagation and scattering in random media*, volume 2. Academic press New York, 1978.

[6] MCW van van Rossum and Th M Nieuwenhuizen. Multiple scattering of classical waves: microscopy, mesoscopy, and diffusion. *Reviews of Modern Physics*, 71(1):313, 1999.

[7] KM Case and PF Zweifel. Linear transport theory. 1967.

[8] DA Boas, MA O'leary, B Chance, and AG Yodh. Scattering of diffuse photon density waves by spherical inhomogeneities within turbid media: analytic solution and applications. *Proceedings of the National Academy of Sciences*, 91(11):4887–4891, 1994.

[9] MA OLeary, DA Boas, XD Li, B Chance, and AG Yodh. Fluorescence lifetime imaging in turbid media. *Optics Letters*, 21(2):158–160, 1996.

[10] Troy O McBride, Brian W Pogue, Ellen D Gerety, Steven B Poplack, Ulf L Österberg, and Keith D Paulsen. Spectroscopic diffuse optical tomography for the quantitative assessment of hemoglobin concentration and oxygen saturation in breast tissue. *Applied optics*, 38(25):5480–5490, 1999.

[11] Natasha Shah, Albert Cerussi, Charlotta Eker, Jenny Espinoza, John Butler, Joshua Fishkin, Rene Hornung, and Bruce Tromberg. Noninvasive functional optical spectroscopy of human breast tissue. *Proceedings of the National Academy of Sciences*, 98(8):4420–4425, 2001.

[12] Vasilis Ntziachristos, AG Yodh, Mitchell D Schnall, and Britton Chance. Mri-guided diffuse optical spectroscopy of malignant and benign breast lesions. *Neoplasia*, 4(4):347–354, 2002.

[13] David A Boas, Maria Angela Franceschini, Andy K Dunn, and Gary Strangman. Non-invasive imaging of cerebral activation with diffuse optical tomography. *In vivo optical imaging of brain function*, pages 193–221, 2002.

[14] Yuanqing Lin, Gwen Lech, Shoko Nioka, Xavier Intes, and Britton Chance. Noninvasive, low-noise, fast imaging of blood volume and deoxygenation changes in muscles using light-emitting diode continuous-wave imager. *Review of Scientific Instruments*, 73(8):3065–3074, 2002.

[15] Joseph P Culver, Andrew M Siegel, Jonathan J Stott, and David A Boas. Volumetric diffuse optical tomography of brain activity. *Optics letters*, 28(21):2061–2063, 2003.

[16] David J Cuccia, Frederic Bevilacqua, Anthony J Durkin, Sean Merritt, Bruce J Tromberg, Gultekin Gulsen, Hon Yu, Jun Wang, and Orhan Nalcioglu. In vivo quantification of optical contrast agent dynamics in rat tumors by use of diffuse optical spectroscopy with magnetic resonance imaging coregistration. *Applied optics*, 42(16):2940–2950, 2003.

[17] Guoqiang Yu, Turgut Durduran, Daisuke Furuya, Joel H Greenberg, and Arjun G Yodh. Frequency-domain multiplexing system for in vivo diffuse light measurements of rapid cerebral hemodynamics. *Applied optics*, 42(16):2931–2939, 2003.

[18] Sean Merritt, Frederic Bevilacqua, Anthony J Durkin, David J Cuccia, Ryan Lanning, Bruce J Tromberg, Gultekin Gulsen, Hon Yu, Jun Wang, and Orhan Nalcioglu. Coregistration of diffuse optical spectroscopy and magnetic resonance imaging in a rat tumor model. *Applied optics*, 42(16):2951–2959, 2003.

[19] David A Boas, Anders M Dale, and Maria Angela Franceschini. Diffuse optical imaging of brain activation: approaches to optimizing image sensitivity, resolution, and accuracy. *Neuroimage*, 23:S275–S288, 2004.

[20] Turgut Durduran, Guoqiang Yu, Mark G Burnett, John A Detre, Joel H Greenberg, Jiongjiong Wang, Chao Zhou, and Arjun G Yodh. Diffuse optical measurement of blood flow, blood oxygenation, and metabolism in a human brain during sensorimotor cortex activation. *Optics letters*, 29(15):1766–1768, 2004.

[21] Natasha Shah, Albert E Cerussi, Dorota Jakubowski, David Hsiang, John Butler, and Bruce J Tromberg. The role of diffuse optical spectroscopy in the clinical management of breast cancer. *Disease markers*, 19(2-3):95–105, 2004.

[22] Dorota B Jakubowski, Albert E Cerussi, Natasha Shah, David Hsiang, John Butler,

Bruce J Tromberg, et al. Monitoring neoadjuvant chemotherapy in breast cancer using quantitative diffuse optical spectroscopy: a case study. *Journal of biomedical optics*, 9(1):230–238, 2004.

[23] Natasha Shah, Jessica Gibbs, Dulcy Wolverton, Albert Cerussi, Nola Hylton, and Bruce J Tromberg. Combined diffuse optical spectroscopy and contrast-enhanced magnetic resonance imaging for monitoring breast cancer neoadjuvant chemotherapy: a case study. *Journal of biomedical optics*, 10(5):051503–051503, 2005.

[24] Albert Cerussi, Natasha Shah, David Hsiang, Amanda Durkin, John Butler, and Bruce J Tromberg. In vivo absorption, scattering, and physiologic properties of 58 malignant breast tumors determined by broadband diffuse optical spectroscopy. *Journal of biomedical optics*, 11(4):044005–044005, 2006.

[25] Andrea Bassi, Andrea Farina, Cosimo D'Andrea, Antonio Pifferi, Gianluca Valentini, and Rinaldo Cubeddu. Portable, large-bandwidth time-resolved system for diffuse optical spectroscopy. *Optics express*, 15(22):14482–14487, 2007.

[26] Albert Cerussi, David Hsiang, Natasha Shah, Rita Mehta, Amanda Durkin, John Butler, and Bruce J Tromberg. Predicting response to breast cancer neoadjuvant chemotherapy using diffuse optical spectroscopy. *Proceedings of the National Academy of Sciences*, 104(10):4014–4019, 2007.

[27] Ronald X Xu, Bo Qiang, Jimmy J Mao, and Stephen P Povoski. Development of a handheld near-infrared imager for dynamic characterization of in vivo biological tissue systems. *Applied optics*, 46(30):7442–7451, 2007.

[28] Maria Angela Franceschini, Sonal Thaker, George Themelis, Kalpathy K Krishnamoorthy, Heather Bortfeld, Solomon G Diamond, David A Boas, Kara Arvin, and P Ellen Grant. Assessment of infant brain development with frequency-domain near-infrared spectroscopy. *Pediatric research*, 61:546–551, 2007.

[29] Raiyan T Zaman, Parmeswaran Diagaradjane, James C Wang, Jon Schwartz, Narasimhan Rajaram, Kelly L Gill-Sharp, Sang H Cho, Henry Grady Rylander III, J Donald Payne, Sunil Krishnan, et al. In vivo detection of gold nanoshells in tumors using diffuse optical spectroscopy. *Selected Topics in Quantum Electronics, IEEE Journal of*, 13(6):1715–1720, 2007.

[30] SH Chung, AE Cerussi, C Klifa, HM Baek, O Birgul, G Gulsen, SI Merritt, D Hsiang, and BJ Tromberg. In vivo water state measurements in breast cancer using broadband diffuse optical spectroscopy. *Physics in medicine and biology*, 53(23):6713, 2008.

[31] Sheng-Hao Tseng, Alexander Grant, and Anthony J Durkin. In vivo determination of skin near-infrared optical properties using diffuse optical spectroscopy. *Journal of biomedical optics*, 13(1):014016–014016, 2008.

[32] Shudong Jiang, Brian W Pogue, Colin M Carpenter, Steven P Poplack, Wendy A Wells, Christine A Kogel, Jorge A Forero, Lori S Muffly, Gary N Schwartz, Keith D Paulsen, et al. Evaluation of breast tumor response to neoadjuvant chemotherapy with tomographic diffuse optical spectroscopy: Case studies of tumor region-of-interest changes 1. *Radiology*, 252(2):551–560, 2009.

[33] MA OLeary, DA Boas, B Chance, and AG Yodh. Experimental images of heterogeneous turbid media by frequency-domain diffusing-photon tomography. *Optics letters*,

20(5):426–428, 1995.

[34] Simon R Arridge and William RB Lionheart. Nonuniqueness in diffusion-based optical tomography. *Optics Letters*, 23(11):882–884, 1998.

[35] Simon R Arridge. Optical tomography in medical imaging. *Inverse problems*, 15(2):R41, 1999.

[36] A Siegel, JJ Marota, and David Boas. Design and evaluation of a continuous-wave diffuse optical tomography system. *Optics express*, 4(8):287–298, 1999.

[37] SB Colak, MB Van der Mark, GW'T Hooft, JH Hoogenraad, ES Van der Linden, and FA Kuijpers. Clinical optical tomography and nir spectroscopy for breast cancer detection. *Selected Topics in Quantum Electronics, IEEE Journal of*, 5(4):1143–1158, 1999.

[38] Vasilis Ntziachristos, AG Yodh, Mitchell Schnall, and Britton Chance. Concurrent mri and diffuse optical tomography of breast after indocyanine green enhancement. *Proceedings of the National Academy of Sciences*, 97(6):2767–2772, 2000.

[39] Daniel J Hawrysz and Eva M Sevick-Muraca. Developments toward diagnostic breast cancer imaging using near-infrared optical measurements and fluorescent contrast agents 1. *Neoplasia*, 2(5):388–417, 2000.

[40] Troy O McBride, Brian W Pogue, Shudong Jiang, Ulf L Oesterberg, and Keith D Paulsen. A parallel-detection frequency-domain near-infrared tomography system for hemoglobin imaging of the breast in vivo. *Review of Scientific Instruments*, 72(3):1817–1824, 2001.

[41] Brian W Pogue, Steven P Poplack, Troy O McBride, Wendy A Wells, K Sunshine Osterman, Ulf L Osterberg, and Keith D Paulsen. Quantitative hemoglobin tomography with

diffuse near-infrared spectroscopy: Pilot results in the breast 1. *Radiology*, 218(1):261–266, 2001.

[42] T Durduran, R Choe, JP Culver, L Zubkov, MJ Holboke, J Giammarco, B Chance, and AG Yodh. Bulk optical properties of healthy female breast tissue. *Physics in medicine and biology*, 47(16):2847, 2002.

[43] Xavier Intes, Jorge Ripoll, Yu Chen, Shoko Nioka, AG Yodh, and Britton Chance. In vivo continuous-wave optical breast imaging enhanced with indocyanine green. *Medical physics*, 30(6):1039–1047, 2003.

[44] JP Culver, R Choe, MJ Holboke, L Zubkov, T Durduran, A Slemp, V Ntziachristos, B Chance, and AG Yodh. Three-dimensional diffuse optical tomography in the parallel plane transmission geometry: evaluation of a hybrid frequency domain/continuous wave clinical system for breast imaging. *Medical physics*, 30(2):235–247, 2003.

[45] Alper Corlu, Turgut Durduran, Regine Choe, Martin Schweiger, Elizabeth Hillman, Simon R Arridge, and Arjun G Yodh. Uniqueness and wavelength optimization in continuous-wave multispectral diffuse optical tomography. *Optics letters*, 28(23):2339–2341, 2003.

[46] Turgut Durduran, Regine Choe, Guoqiang Yu, Chao Zhou, Julia C Tchou, Brian J Czerniecki, and Arjun G Yodh. Diffuse optical measurement of blood flow in breast tumors. *Optics letters*, 30(21):2915–2917, 2005.

[47] Regine Choe, Alper Corlu, Kijoon Lee, Turgut Durduran, Soren D Konecky, Monika Grosicka-Koptyra, Simon R Arridge, Brian J Czerniecki, Douglas L Fraker, Angela DeMichele, et al. Diffuse optical tomography of breast cancer during neoadjuvant

chemotherapy: a case study with comparison to mri. *Medical physics*, 32(4):1128–1139, 2005.

[48] Tara D Yates, Jeremy C Hebden, Adam P Gibson, Louise Enfield, Nicholas L Everdell, Simon R Arridge, and David T Delpy. Time-resolved optical mammography using a liquid coupled interface. *Journal of biomedical optics*, 10(5):054011–054011, 2005.

[49] Alper Corlu, Regine Choe, Turgut Durduran, Mark A Rosen, Martin Schweiger, Simon R Arridge, Mitchell D Schnall, and Arjun G Yodh. Three-dimensional in vivo fluorescence diffuse optical tomography of breast cancer in humans. *Optics express*, 15(11):6696–6716, 2007.

[50] Joseph M Lasker, James M Masciotti, Matthew Schoenecker, Christoph H Schmitz, and Andreas H Hielscher. Digital-signal-processor-based dynamic imaging system for optical tomography. *Review of Scientific Instruments*, 78(8):083706, 2007.

[51] Phaneendra K Yalavarthy, Brian W Pogue, Hamid Dehghani, Colin M Carpenter, Shudong Jiang, and Keith D Paulsen. Structural information within regularization matrices improves near infrared diffuse optical tomography. *Optics Express*, 15(13):8043–8058, 2007.

[52] Soren D Konecky, George Y Panasyuk, Kijoon Lee, Vadim Markel, Arjun G Yodh, and John C Schotland. Imaging complex structures with diffuse light. *Optics express*, 16(7):5048–5060, 2008.

[53] Regine Choe, Soren D Konecky, Alper Corlu, Kijoon Lee, Turgut Durduran, David R Busch, Saurav Pathak, Brian J Czerniecki, Julia Tchou, Douglas L Fraker, et al. Differentiation of benign and malignant breast tumors by in-vivo three-dimensional parallel-plate

diffuse optical tomography. *Journal of biomedical optics*, 14(2):024020–024020, 2009.

[54] Turgut Durduran, Regine Choe, WB Baker, and AG Yodh. Diffuse optics for tissue monitoring and tomography. *Reports on Progress in Physics*, 73(7):076701, 2010.

[55] Molly L Flexman, Michael A Khalil, Rabah Al Abdi, Hyun K Kim, Christopher J Fong, Elise Desperito, Dawn L Hershman, Randall L Barbour, and Andreas H Hielscher. Digital optical tomography system for dynamic breast imaging. *Journal of biomedical optics*, 16(7):076014–076014, 2011.

[56] Joseph P Culver, Turgut Durduran, Cecil Cheung, AG Yodh, Daisuke Furuya, and Joel H Greenberg. Diffuse optical measurement of hemoglobin and cerebral blood flow in rat brain during hypercapnia, hypoxia and cardiac arrest. In *Oxygen Transport To Tissue XXIII*, pages 293–297. Springer, 2003.

[57] Turgut Durduran, Mark G Burnett, Guoqiang Yu, Chao Zhou, Daisuke Furuya, Arjun G Yodh, John A Detre, and Joel H Greenberg. Spatiotemporal quantification of cerebral blood flow during functional activation in rat somatosensory cortex using laser-speckle flowmetry. *Journal of Cerebral Blood Flow & Metabolism*, 24(5):518–525, 2004.

[58] Guoqiang Yu, Turgut Durduran, Chao Zhou, Hsing-Wen Wang, Mary E Putt, H Mark Saunders, Chandra M Sehgal, Eli Glatstein, Arjun G Yodh, and Theresa M Busch. Noninvasive monitoring of murine tumor blood flow during and after photodynamic therapy provides early assessment of therapeutic efficacy. *Clinical cancer research*, 11(9):3543–3552, 2005.

[59] Guoqiang Yu, Turgut Durduran, Gwen Lech, Chao Zhou, Britton Chance, Emile R

Mohler, and Arjun G Yodh. Time-dependent blood flow and oxygenation in human skeletal muscles measured with noninvasive near-infrared diffuse optical spectroscopies. *Journal of biomedical optics*, 10(2):024027–02402712, 2005.

[60] Ulas Sunar, Harry Quon, Turgut Durduran, Jun Zhang, Juan Du, Chao Zhou, Guoqiang Yu, Regine Choe, Alex Kilger, Robert Lustig, et al. Noninvasive diffuse optical measurement of blood flow and blood oxygenation for monitoring radiation therapy in patients with head and neck tumors: a pilot study. *Journal of biomedical optics*, 11(6):064021–064021, 2006.

[61] Chao Zhou, Guoqiang Yu, Daisuke Furuya, Joel Greenberg, Arjun Yodh, and Turgut Durduran. Diffuse optical correlation tomography of cerebral blood flow during cortical spreading depression in rat brain. *Optics express*, 14(3):1125–1144, 2006.

[62] Guoqiang Yu, Thomas F Floyd, Turgut Durduran, Chao Zhou, Jiongjiong Wang, John A Detre, and Arjun G Yodh. Validation of diffuse correlation spectroscopy for muscle blood flow with concurrent arterial spin labeled perfusion mri. *Optics express*, 15(3):1064–1075, 2007.

[63] Chao Zhou, Regine Choe, Natasha Shah, Turgut Durduran, Guoqiang Yu, Amanda Durkin, David Hsiang, Rita Mehta, John Butler, Albert Cerussi, et al. Diffuse optical monitoring of blood flow and oxygenation in human breast cancer during early stages of neoadjuvant chemotherapy. *Journal of biomedical optics*, 12(5):051903–051903, 2007.

[64] SA Carp, GP Dai, DA Boas, MA Franceschini, and YR Kim. Validation of diffuse correlation spectroscopy measurements of rodent cerebral blood flow with simultaneous arterial spin labeling mri; towards mri-optical continuous cerebral metabolic monitoring.

Biomedical optics express, 1(2):553–565, 2010.

[65] Meeri N Kim, Turgut Durduran, Suzanne Frangos, Brian L Edlow, Erin M Buckley, Heather E Moss, Chao Zhou, Guoqiang Yu, Regine Choe, Eileen Maloney-Wilensky, et al. Noninvasive measurement of cerebral blood flow and blood oxygenation using near-infrared and diffuse correlation spectroscopies in critically brain-injured adults. *Neurocritical care*, 12(2):173–180, 2010.

[66] Yu Shang, TB Symons, Turgut Durduran, Arjun G Yodh, and Guoqiang Yu. Effects of muscle fiber motion on diffuse correlation spectroscopy blood flow measurements during exercise. *Biomedical optics express*, 1(2):500–511, 2010.

[67] Mamadou Diop, Kyle Verdecchia, Ting-Yim Lee, and Keith St Lawrence. Calibration of diffuse correlation spectroscopy with a time-resolved near-infrared technique to yield absolute cerebral blood flow measurements. *Biomedical optics express*, 2(7):2068–2081, 2011.

[68] Daniel Irwin, Lixin Dong, Yu Shang, Ran Cheng, Mahesh Kudrimoti, Scott D Stevens, and Guoqiang Yu. Influences of tissue absorption and scattering on diffuse correlation spectroscopy blood flow measurements. *Biomedical optics express*, 2(7):1969–1985, 2011.

[69] Ting Li, Yu Lin, Yu Shang, Lian He, Chong Huang, Margaret Szabunio, and Guoqiang Yu. Simultaneous measurement of deep tissue blood flow and oxygenation using noncontact diffuse correlation spectroscopy flow-oximeter. *Scientific reports*, 3, 2013.

[70] Turgut Durduran and Arjun G Yodh. Diffuse correlation spectroscopy for non-invasive, micro-vascular cerebral blood flow measurement. *Neuroimage*, 85:51–63, 2014.

[71] Jiemin Ma and Ahmedin Jemal. Breast cancer statistics. In *Breast Cancer Metastasis and Drug Resistance*, pages 1–18. Springer, 2013.

[72] Ahmedin Jemal, Melissa M Center, Carol DeSantis, and Elizabeth M Ward. Global patterns of cancer incidence and mortality rates and trends. *Cancer Epidemiology Biomarkers & Prevention*, 19(8):1893–1907, 2010.

[73] John J Barron, Ralph Quimbo, Prashant T Nikam, and Mayur M Amonkar. Assessing the economic burden of breast cancer in a us managed care population. *Breast cancer research and treatment*, 109(2):367–377, 2008.

[74] Yan Zhao, Michael A Mastanduno, Shudong Jiang, Fadi El-Ghussein, Junqing Xu, Jiang Gui, Brian W Pogue, and Keith D Paulsen. Systematic optimization of mri guided near infrared diffuse optical spectroscopy in breast. In *SPIE BiOS*, pages 931605–931605. International Society for Optics and Photonics, 2015.

[75] Noel Weidner, Judah Folkman, Franco Pozza, Pierantonio Bevilacqua, Elizabeth N Allred, Dan H Moore, Salvatore Meli, and Giampietro Gasparini. Tumor angiogenesis: a new significant and independent prognostic indicator in early-stage breast carcinoma. *Journal of the National Cancer Institute*, 84(24):1875–1887, 1992.

[76] Sharon Thomsen and Dereck Tatman. Physiological and pathological factors of human breast disease that can influence optical diagnosis. *Annals of the New York Academy of Sciences*, 838(1):171–193, 1998.

[77] Quing Zhu, NanGuang Chen, and Scott H Kurtzman. Imaging tumor angiogenesis by use of combined near-infrared diffusive light and ultrasound. *Optics letters*, 28(5):337–339, 2003.

[78] Stephen T Flock, Brian C Wilson, and Michael S Patterson. Total attenuation coefficients and scattering phase functions of tissues and phantom materials at 633 nm. *Medical Physics*, 14(5):835–841, 1987.

[79] Sharon L Thomsen, Steven L Jacques, and Stephen T Flock. Microscopic correlates of macroscopic optical property changes during thermal coagulation of myocardium. In *OE/LASE'90, 14-19 Jan., Los Angeles, CA*, pages 2–11. International Society for Optics and Photonics, 1990.

[80] Regine Choe. *Diffuse optical tomography and spectroscopy of breast cancer and fetal brain*. PhD thesis, University of Pennsylvania, 2005.

[81] Britton Chance, Shoko Nioka, Jane Kent, Kevin McCully, Michael Fountain, Robert Greenfeld, and Gary Holtom. Time-resolved spectroscopy of hemoglobin and myoglobin in resting and ischemic muscle. *Analytical biochemistry*, 174(2):698–707, 1988.

[82] E Gratton, WW Mantulin, MJ Van De Ven, JB Fishkin, MB Maris, and B Chance. The possibility of a near-infrared optical imaging system using frequency-domain methods. In *Proceedings of III International Conference for Peace through Mind/Brain Science*, pages 183–189, 1990.

[83] DA Benaron, J VANHOUTEN, DC Ho, SD Spilman, and DK Stevenson. Imaging neonatal brain injury using light-based optical tomography. In *Pediatric Research*, volume 35, pages A378–A378. WILLIAMS & WILKINS 351 WEST CAMDEN ST, BALTIMORE, MD 21201-2436, 1994.

[84] John P van Houten, Wai-Fung Cheong, Eben L Kermit, Timothy R Machold, David K

Stevenson, and David A Benaron. Clinical measurement of brain oxygenation and function using light-based optical tomography. *Pediatric Research*, 39:382–382, 1996.

[85] Jeremy C Hebden, Adam Gibson, Rozarina Md Yusof, Nick Everdell, Elizabeth MC Hillman, David T Delpy, Simon R Arridge, Topun Austin, Judith H Meek, and John S Wyatt. Three-dimensional optical tomography of the premature infant brain. *Physics in medicine and biology*, 47(23):4155, 2002.

[86] Jeremy C Hebden. Advances in optical imaging of the newborn infant brain. *Psychophysiology*, 40(4):501–510, 2003.

[87] Andrew M Siegel, Joseph P Culver, Joseph B Mandeville, and David A Boas. Temporal comparison of functional brain imaging with diffuse optical tomography and fmri during rat forepaw stimulation. *Physics in medicine and biology*, 48(10):1391, 2003.

[88] Heng Xu, Hamid Dehghani, Brian W Pogue, Roger Springett, Keith D Paulsen, and Jeff F Dunn. Near-infrared imaging in the small animal brain: optimization of fiber positions. *Journal of Biomedical Optics*, 8(1):102–110, 2003.

[89] Nadège Roche-Labarbe, Stefan A Carp, Andrea Surova, Megha Patel, David A Boas, P Ellen Grant, and Maria Angela Franceschini. Noninvasive optical measures of cbv, sto2, cbf index, and rcmro2 in human premature neonates' brains in the first six weeks of life. *Human brain mapping*, 31(3):341–352, 2010.

[90] Daniel Richard Leff, Oliver J Warren, Louise C Enfield, Adam Gibson, Thanos Athanasiou, Darren K Patten, Jem Hebden, Guang Zhong Yang, and Ara Darzi. Diffuse optical imaging of the healthy and diseased breast: a systematic review. *Breast cancer research and treatment*, 108(1):9–22, 2008.

[91] Bruce J Tromberg, Brian W Pogue, Keith D Paulsen, Arjun G Yodh, David A Boas, and Albert E Cerussi. Assessing the future of diffuse optical imaging technologies for breast cancer management. *Medical physics*, 35(6):2443–2451, 2008.

[92] Jia Wang, Shudong Jiang, Zhongze Li, Richard J Barth, Peter A Kaufman, Brian W Pogue, Keith D Paulsen, et al. In vivo quantitative imaging of normal and cancerous breast tissue using broadband diffuse optical tomography. *Medical physics*, 37(7):3715–3724, 2010.

[93] Bruce J Tromberg, Albert Cerussi, Natasha Shah, Montana Compton, Amanda Durkin, David Hsiang, John Butler, and Rita Mehta. Imaging in breast cancer: diffuse optics in breast cancer: detecting tumors in pre-menopausal women and monitoring neoadjuvant chemotherapy. *Breast Cancer Research*, 7(6):279, 2005.

[94] Quing Zhu, Susan Tannenbaum, Poornima Hegde, Mark Kane, Chen Xu, and Scott H Kurtzman. Noninvasive monitoring of breast cancer during neoadjuvant chemotherapy using optical tomography with ultrasound localization. *Neoplasia*, 10(10):1028–1040, 2008.

[95] Marc Schegerin, Anna NA Tosteson, Peter A Kaufman, Keith D Paulsen, and Brian W Pogue. Prognostic imaging in neoadjuvant chemotherapy of locally-advanced breast cancer should be cost-effective. *Breast cancer research and treatment*, 114(3):537–547, 2009.

[96] Albert E Cerussi, Vaya W Tanamai, David Hsiang, John Butler, Rita S Mehta, and Bruce J Tromberg. Diffuse optical spectroscopic imaging correlates with final pathological response in breast cancer neoadjuvant chemotherapy. *Philosophical Transactions*

of the Royal Society of London A: Mathematical, Physical and Engineering Sciences, 369(1955):4512–4530, 2011.

[97] Regine Choe and Turgut Durduran. Diffuse optical monitoring of the neoadjuvant breast cancer therapy. *Selected Topics in Quantum Electronics, IEEE Journal of*, 18(4):1367–1386, 2012.

[98] David R Busch, Regine Choe, Mark A Rosen, Wensheng Guo, Turgut Durduran, Michael D Feldman, Carolyn Mies, Brian J Czerniecki, Julia Tchou, Angela DeMichele, et al. Optical malignancy parameters for monitoring progression of breast cancer neoadjuvant chemotherapy. *Biomedical optics express*, 4(1):105–121, 2013.

[99] BW Pogue, MS Patterson, H Jiang, and KD Paulsen. Initial assessment of a simple system for frequency domain diffuse optical tomography. *Physics in medicine and biology*, 40(10):1709, 1995.

[100] S Nioka, Y Yung, M Shnall, S Zhao, S Orel, C Xie, B Chance, and L Solin. Optical imaging of breast tumor by means of continuous waves. In *Oxygen Transport to Tissue XVIII*, pages 227–232. Springer, 1997.

[101] Steven P Poplack, Tor D Tosteson, Wendy A Wells, Brian W Pogue, Paul M Meaney, Alexander Hartov, Christine A Kogel, Sandra K Soho, Jennifer J Gibson, and Keith D Paulsen. Electromagnetic breast imaging: Results of a pilot study in women with abnormal mammograms 1. *Radiology*, 243(2):350–359, 2007.

[102] Louise C Enfield, Adam P Gibson, Nicholas L Everdell, David T Delpy, Martin Schweiger, Simon R Arridge, Caroline Richardson, Mohammad Keshtgar, Michael Douek, and Jeremy C Hebden. Three-dimensional time-resolved optical mammography

of the uncompressed breast. *Applied optics*, 46(17):3628–3638, 2007.

[103] Dirk Grosenick, K Thomas Moesta, M Michael, Heidrun Wabnitz, Bernd Gebauer, Christian Stroszczynski, Bernhard Wassermann, Peter M Schlag, Herbert Rinneberg, et al. Time-domain scanning optical mammography: I. recording and assessment of mammograms of 154 patients. *Physics in medicine and biology*, 50(11):2429, 2005.

[104] Antonio Pifferi, Paola Taroni, Alessandro Torricelli, Fabrizio Messina, Rinaldo Cubeddu, and Gianmaria Danesini. Four-wavelength time-resolved optical mammography in the 680 980-nm range. *Optics letters*, 28(13):1138–1140, 2003.

[105] Alper Corlu, Regine Choe, Turgut Durduran, Kijoon Lee, Martin Schweiger, Simon R Arridge, Elizabeth Hillman, and Arjun G Yodh. Diffuse optical tomography with spectral constraints and wavelength optimization. *Applied optics*, 44(11):2082–2093, 2005.

[106] Soren D Konecky, Regine Choe, Alper Corlu, Kijoon Lee, Rony Wiener, Shyam M Srinivas, Janet R Saffer, Richard Freifelder, Joel S Karp, Nassim Hajjioui, et al. Comparison of diffuse optical tomography of human breast with whole-body and breast-only positron emission tomography. *Medical physics*, 35(2):446–455, 2008.

[107] Q Zhu, T Durduran, V Ntziachristos, M Holboke, and AG Yodh. Imager that combines near-infrared diffusive light and ultrasound. *Optics letters*, 24(15):1050–1052, 1999.

[108] Monica J Holboke, Bruce J Tromberg, Xingde Li, Natasha Shah, J Fishkin, D Kidney, J Butler, Britton Chance, and Arjun G Yodh. Three-dimensional diffuse optical mammography with ultrasound localization in a human subject. *Journal of Biomedical Optics*, 5(2):237, 2000.

[109] Vasilis Ntziachristos, Britton Chance, and Arjun Yodh. Differential diffuse optical tomography. *Optics Express*, 5(10):230–242, 1999.

[110] Vasilis Ntziachristos, Andreas H Hielscher, AG Yodh, and Britton Chance. Diffuse optical tomography of highly heterogeneous media. *Medical Imaging, IEEE Transactions on*, 20(6):470–478, 2001.

[111] AP Gibson, JC Hebden, and Simon R Arridge. Recent advances in diffuse optical imaging. *Physics in medicine and biology*, 50(4):R1, 2005.

[112] Vivek Venugopal and Xavier Intes. Recent advances in optical mammography. *Current Medical Imaging Reviews*, 8(3):244–259, 2012.

[113] Richard C Haskell, Lars O Svaasand, Tsong-Tseh Tsay, Ti-Chen Feng, Bruce J Tromberg, and Matthew S McAdams. Boundary conditions for the diffusion equation in radiative transfer. *JOSA A*, 11(10):2727–2741, 1994.

[114] R. Aronson. Extrapolation distance for diffusion of light. *Photon Migration and Imaging in Random Media and Tissues*, 1888:297–305, 1993.

[115] R. Aronson. Boundary conditions for diffusion of light. *J Opt Soc Am A Opt Image Sci Vis*, 12:2532–2539, 1995.

[116] Daniele Contini, Fabrizio Martelli, and Giovanni Zaccanti. Photon migration through a turbid slab described by a model based on diffusion approximation. i. theory. *Applied optics*, 36(19):4587–4599, 1997.

[117] SE Orchard. Reflection and transmission of light by diffusing suspensions. *JOSA*, 59(12):1584–1597, 1969.

[118] Anuradha Godavarty, Daniel Hawrysz, Ranadhir Roy, Eva Sevick-Muraca, and Margaret Eppstein. Influence of the refractive index-mismatch at the boundaries measured in fluorescenceenhanced frequency-domain photon migration imaging. *Optics Express*, 10(15):653–662, 2002.

[119] Judith R Mourant, Tamika Fuselier, James Boyer, Tamara M Johnson, and Irving J Bigio. Predictions and measurements of scattering and absorption over broad wavelength ranges in tissue phantoms. *Applied Optics*, 36(4):949–957, 1997.

[120] RMP Doornbos, Roland Lang, MC Aalders, FW Cross, and HJCM Sterenborg. The determination of in vivo human tissue optical properties and absolute chromophore concentrations using spatially resolved steady-state diffuse reflectance spectroscopy. *Physics in medicine and biology*, 44(4):967, 1999.

[121] Lihong V Wang and Hsin-i Wu. *Biomedical optics: principles and imaging*. John Wiley & Sons, 2012.

[122] Steven L Jacques. Optical properties of biological tissues: a review. *Physics in medicine and biology*, 58(11):R37, 2013.

[123] Nancy A Lee, Henry Rusinek, Jeffrey Weinreb, Ramesh Chandra, Hildegard Toth, Cory Singer, and Gillian Newstead. Fatty and fibroglandular tissue volumes in the breasts of women 20-83 years old: comparison of x-ray mammography and computer-assisted mr imaging. *AJR. American journal of roentgenology*, 168(2):501–506, 1997.

[124] DR White, HQ Woodard, and SM Hammond. Average soft-tissue and bone models for use in radiation dosimetry. *The British journal of radiology*, 60(717):907–913, 1987.

[125] HQ Woodard and DR White. The composition of body tissues. *The British journal of*

radiology, 59(708):1209–1218, 1986.

[126] Subhadra Srinivasan, Brian W Pogue, Shudong Jiang, Hamid Dehghani, and Keith D Paulsen. Spectrally constrained chromophore and scattering near-infrared tomography provides quantitative and robust reconstruction. *Applied optics*, 44(10):1858–1869, 2005.

[127] Changqing Li, Stephen R Grobmyer, Lin Chen, Qizhi Zhang, Laurie L Fajardo, and Huabei Jiang. Multispectral diffuse optical tomography with absorption and scattering spectral constraints. *Applied optics*, 46(34):8229–8236, 2007.

[128] Frederic Bevilacqua, Andrew J Berger, Albert E Cerussi, Dorota Jakubowski, and Bruce J Tromberg. Broadband absorption spectroscopy in turbid media by combined frequency-domain and steady-state methods. *Applied optics*, 39(34):6498–6507, 2000.

[129] John C Schotland. Continuous-wave diffusion imaging. *JOSA A*, 14(1):275–279, 1997.

[130] Vadim A Markel and John C Schotland. Inverse scattering for the diffusion equation with general boundary conditions. *Physical Review E*, 64(3):035601, 2001.

[131] Vadim A Markel and John C Schotland. Effects of sampling and limited data in optical tomography. *Applied physics letters*, 81(7):1180–1182, 2002.

[132] Vadim A Markel and John C Schotland. Inverse problem in optical diffusion tomography. ii. role of boundary conditions. *JOSA A*, 19(3):558–566, 2002.

[133] Vadim A Markel, Vivek Mital, and John C Schotland. Inverse problem in optical diffusion tomography. iii. inversion formulas and singular-value decomposition. *JOSA A*, 20(5):890–902, 2003.

[134] Vadim A Markel, Joseph A OSullivan, and John C Schotland. Inverse problem in optical diffusion tomography. iv. nonlinear inversion formulas. *JOSA A*, 20(5):903–912, 2003.

[135] Vadim A Markel and John C Schotland. Symmetries, inversion formulas, and image reconstruction for optical tomography. *Physical Review E*, 70(5):056616, 2004.

[136] Zheng-Min Wang, George Y Panasyuk, Vadim A Markel, and John C Schotland. Experimental demonstration of an analytic method for image reconstruction in optical diffusion tomography with large data sets. *Optics letters*, 30(24):3338–3340, 2005.

[137] Han Y Ban, David R Busch, Saurav Pathak, Frank A Moscatelli, Manabu Machida, John C Schotland, Vadim A Markel, and Arjun G Yodh. Diffuse optical tomography in the presence of a chest wall. *Journal of biomedical optics*, 18(2):026016–026016, 2013.

[138] Soren D Konecky. *Non-invasive imaging of breast cancer with diffusing near-infrared light*. PhD thesis, University of Pennsylvania, 2008.

[139] AC Kak and M Slaney. Principles of computerized tomography (piscataway, nj: Ieee). 1987.

[140] Xavier Intes, Vasilis Ntziachristos, Joe P Culver, Arjun Yodh, and Britton Chance. Projection access order in algebraic reconstruction technique for diffuse optical tomography. *Physics in medicine and biology*, 47(1):N1, 2002.

[141] CP Gonatas, Masaru Ishii, John S Leigh, and John C Schotland. Optical diffusion imaging using a direct inversion method. *Physical Review E*, 52(4):4361, 1995.

[142] Magnus Rudolph Hestenes and Eduard Stiefel. Methods of conjugate gradients for solving linear systems. 1952.

[143] SR Arridge, M Schweiger, M Hiraoka, and DT Delpy. A finite element approach for modeling photon transport in tissue. *Medical physics*, 20(2):299–309, 1993.

[144] Keith D Paulsen and Huabei Jiang. Spatially varying optical property reconstruction using

a finite element diffusion equation approximation. *Medical Physics*, 22(6):691–701, 1995.

[145] Simon R Arridge, Hamid Dehghani, Martin Schweiger, and Eiji Okada. The finite element model for the propagation of light in scattering media: a direct method for domains with nonscattering regions. *Medical physics*, 27(1):252–264, 2000.

[146] Martin Schweiger and Simon Arridge. The toast++ software suite for forward and inverse modeling in optical tomography. *Journal of biomedical optics*, 19(4):040801–040801, 2014.

[147] Simon Arridge and Martin Schweiger. A gradient-based optimisation scheme foroptical tomography. *Optics Express*, 2(6):213–226, 1998.

[148] Martin Schweiger, Simon R Arridge, and Ilkka Nissilä. Gauss–newton method for image reconstruction in diffuse optical tomography. *Physics in medicine and biology*, 50(10):2365, 2005.

[149] Jonathan Richard Shewchuk. An introduction to the conjugate gradient method without the agonizing pain, 1994.

[150] Michael S Patterson, Britton Chance, and Brian C Wilson. Time resolved reflectance and transmittance for the noninvasive measurement of tissue optical properties. *Applied optics*, 28(12):2331–2336, 1989.

[151] David A Benaron and David K Stevenson. Optical time-of-flight and absorbance imaging of biologic media. *Science*, 259(5100):1463–1466, 1993.

[152] Stefan Andersson-Engels, O Jarlman, R Berg, and S Svanberg. Time-resolved transillumination for medical diagnostics. *Optics letters*, 15(21):1179–1181, 1990.

[153] Steven L Jacques. Time-resolved reflectance spectroscopy in turbid tissues. *Biomedical*

Engineering, IEEE Transactions on, 36(12):1155–1161, 1989.

[154] Florian EW Schmidt, Jeremy C Hebden, Elizabeth Hillman, Martin E Fry, Martin Schweiger, Hamid Dehghani, David T Delpy, and Simon R Arridge. Multiple-slice imaging of a tissue-equivalent phantom by use of time-resolved optical tomography. *Applied optics*, 39(19):3380–3387, 2000.

[155] Vasilis Ntziachristos, XuHui Ma, and Britton Chance. Time-correlated single photon counting imager for simultaneous magnetic resonance and near-infrared mammography. *Review of Scientific Instruments*, 69(12):4221–4233, 1998.

[156] Joshua B Fishkin and Enrico Gratton. Propagation of photon-density waves in strongly scattering media containing an absorbing semi-infinite plane bounded by a straight edge. *JOSA A*, 10(1):127–140, 1993.

[157] Britton Chance, M Cope, E Gratton, N Ramanujam, and B Tromberg. Phase measurement of light absorption and scatter in human tissue. *Review of scientific instruments*, 69(10):3457–3481, 1998.

[158] Brian W Pogue and Michael S Patterson. Frequency-domain optical absorption spectroscopy of finite tissue volumes using diffusion theory. *Physics in medicine and biology*, 39(7):1157, 1994.

[159] Petra Bonfert-Taylor, Frederic Leblond, Robert W Holt, Kenneth Tichauer, Brian W Pogue, and Edward C Taylor. Information loss and reconstruction in diffuse fluorescence tomography. *JOSA A*, 29(3):321–330, 2012.

[160] Stéphanie Chaillat and George Biros. Faims: A fast algorithm for the inverse medium problem with multiple frequencies and multiple sources for the scalar helmholtz equation.

Journal of Computational Physics, 231(12):4403–4421, 2012.

[161] Ralf B Schulz, Jorge Ripoll, and Vasilis Ntziachristos. Noncontact optical tomography of turbid media. *Optics letters*, 28(18):1701–1703, 2003.

[162] Jorge Ripoll, Ralf B Schulz, and Vasilis Ntziachristos. Free-space propagation of diffuse light: theory and experiments. *Physical review letters*, 91(10):103901, 2003.

[163] Jorge Ripoll and Vasilis Ntziachristos. Imaging scattering media from a distance: theory and applications of noncontact optical tomography. *Modern Physics Letters B*, 18(28n29):1403–1431, 2004.

[164] Gordon M Turner, Giannis Zacharakis, Antoine Soubret, Jorge Ripoll, and Vasilis Ntziachristos. Complete-angle projection diffuse optical tomography by use of early photons. *Optics letters*, 30(4):409–411, 2005.

[165] Brian W Pogue and Michael S Patterson. Review of tissue simulating phantoms for optical spectroscopy, imaging and dosimetry. *Journal of biomedical optics*, 11(4):041102–041102, 2006.

[166] Albert E Cerussi, Robert Warren, Brian Hill, Darren Roblyer, Anaïs Leproux, Amanda F Durkin, Thomas D OSullivan, Sam Keene, Hosain Haghany, Timothy Quang, et al. Tissue phantoms in multicenter clinical trials for diffuse optical technologies. *Biomedical optics express*, 3(5):966–971, 2012.

[167] Yasaman Ardeshirpour and Quing Zhu. Optical tomography method that accounts for tilted chest wall in breast imaging. *Journal of biomedical optics*, 15(4):041515–041515, 2010.

[168] Alwin Kienle and Thomas Glanzmann. In vivo determination of the optical properties of

muscle with time-resolved reflectance using a layered model. *Physics in medicine and biology*, 44(11):2689, 1999.

[169] Paola Taroni, Antonio Pifferi, Alessandro Torricelli, Daniela Comelli, and Rinaldo Cubeddu. In vivo absorption and scattering spectroscopy of biological tissues. *Photochemical & Photobiological Sciences*, 2(2):124–129, 2003.

[170] A Blasi, S Fox, N Everdell, A Volein, L Tucker, G Csibra, AP Gibson, JC Hebden, MH Johnson, and CE Elwell. Investigation of depth dependent changes in cerebral haemodynamics during face perception in infants. *Physics in medicine and biology*, 52(23):6849, 2007.

[171] F Orihuela-Espina, DR Leff, DRC James, AW Darzi, and GZ Yang. Quality control and assurance in functional near infrared spectroscopy (fnirs) experimentation. *Physics in medicine and biology*, 55(13):3701, 2010.

[172] Vadim A Markel, Zheng-Min Wang, and John C Schotland. Optical diffusion tomography with large data sets. In *Photonics North 2005*, pages 59691B–59691B. International Society for Optics and Photonics, 2005.

[173] Tamara L Troy, David L Page, and Eva M Sevick-Muraca. Optical properties of normal and diseased breast tissues: prognosis for optical mammography. *Journal of biomedical optics*, 1(3):342–355, 1996.

[174] EM Sevick-Muraca, G Lopez, JS Reynolds, TL Troy, and CL Hutchinson. Fluorescence and absorption contrast mechanisms for biomedical optical imaging using frequency-domain techniques. *Photochemistry and photobiology*, 66(1):55–64, 1997.

[175] Anuradha Godavarty, Margaret J Eppstein, Chaoyang Zhang, Sangeeta Theru, Alan B

Thompson, Michael Gurfinkel, and Eva M Sevick-Muraca. Fluorescence-enhanced optical imaging in large tissue volumes using a gain-modulated iccd camera. *Physics in Medicine and Biology*, 48(12):1701, 2003.

[176] Tao Peng. Algorithms and models for 3-d shape measurement using digital fringe projections. 2007.

[177] Song Zhang and Peisen S Huang. Novel method for structured light system calibration. *Optical Engineering*, 45(8):083601–083601, 2006.

[178] Song Zhang. Flexible 3d shape measurement using projector defocusing: extended measurement range. *Optics letters*, 35(7):934–936, 2010.

[179] Sai Siva Gorthi and Pramod Rastogi. Fringe projection techniques: whither we are? *Optics and lasers in engineering*, 48(IMAC-REVIEW-2009-001):133–140, 2010.

[180] Jason Geng. Structured-light 3d surface imaging: a tutorial. *Advances in Optics and Photonics*, 3(2):128–160, 2011.

[181] Brian Pogue, Markus Testorf, Troy McBride, Ulf Osterberg, and Keith Paulsen. Instrumentation and design of a frequency-domain diffuse optical tomography imager for breast cancer detection. *Optics express*, 1(13):391–403, 1997.

[182] Shudong Jiang, Brian W Pogue, Troy O McBride, Marvin M Doyley, Steven P Poplack, and Keith D Paulsen. Near-infrared breast tomography calibration with optoelastic tissue simulating phantoms. *Journal of electronic imaging*, 12(4):613–620, 2003.